Distant Hemodynamic Impact of Local Geometric Alterations in the Arterial Tree

by

Yoram Richter

B.S. Physics and Computer Science
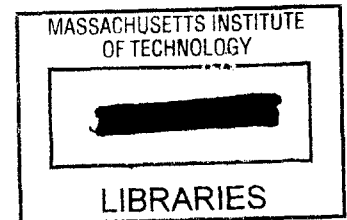Tel Aviv University, 1997

Submitted to the Department of Electrical Engineering and Computer Science in partial fulfillment of the requirements for the degree of

MASTER OF SCIENCE IN ELECTRICAL ENGINEERING AND
COMPUTER SCIENCE
AT THE
MASSACHUSETTS INSTITUTE OF TECHNOLOGY

JUNE 2000

© 2000 Massachusetts Institute of Technology
All rights reserved

Signature of Author _

Department of Electrical Engineering and Computer Science
May 19, 2000

Certified by _____

Elazer R. Edelman
Thomas D. and Virginia W. Cabot Associate Professor
Division of Health Sciences and Technology
Thesis Supervisor

Accepted by _

Arthur C. Smith
Professor of Electrical Engineering and Computer Science
Chairman, Committee on Graduate Students
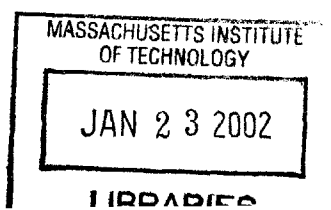
Distant Hemodynamic Impact of Local Geometric Alterations in the Arterial Tree

by

Yoram Richter

Submitted to the Department of Electrical Engineering and Computer Science
on May 19, 2000 in Partial Fulfillment of the Requirements for the Degree of
Master of Science in Electrical Engineering and Computer Science

ABSTRACT

Hemodynamics has long been identified as a major factor in the determination and localization of atherosclerotic lesions. Atherosclerosis is focal and often forms in specific locations in the arterial tree such as bifurcations. Many different aspects of fluid mechanics have been suggested as the trigger for atherogenesis - non-laminar and/or unstable flow, flow separation, regions of higher/lower and/or oscillatory shear stress etc. While the precise mechanism by which these hemodynamic factors act is not yet clear, the fact that they correlate highly with atherogenesis suggests that local disturbances in flow through blood vessels can promote arterial disease. These issues have become increasingly acute as physicians seek to alter the pathological arterial anatomy with bypass grafting or endovascular manipulations such as angioplasty or stenting.

We proposed that vascular interventions might cause previously unforeseen effects in the arterial tree especially at branch points. Manipulation of one branch of a bifurcation might adversely affect the contralateral branch of the bifurcation. The goal of this work was to study the distant impact of local flow alterations, as well as to classify and evaluate the different parameters that determine their severity.

Dynamic flow models of the arterial system were developed that allowed for the continuous alteration of model geometry in a controlled fashion. This property allows for the simulation not only of the healthy or diseased states, but also of the entire range in between. Moreover, these models permit simulation of different strategies of clinical intervention. Flow through the models was investigated using both qualitative (flow visualization) and quantitative (flow and pressure readings) tools. Flow separation and vascular resistance in one location of the arterial tree varied with geometrical alterations in another.

The results of this study could have important implications for the diagnosis, treatment and long-term follow-up of the large number of patients who suffer from these diseases and undergo vascular interventions. Clinical arterial manipulation of one arterial site may well need to consider the hemodynamic impact on vascular segments at a distance.

Thesis Supervisor: Elazer R. Edelman
Title: Thomas D. and Virginia W. Cabot Associate Professor, Division of Health Sciences and Technology

Acknowledgements

Elazer Edelman. For proving everyday that you can mix clinical practice and quality research, family and career, religion and science, personal academic achievements and true mentoring, oil and water, teacher and friend.

Tom McMahon. If it wasn't for his generosity, experience and technical creativity this project might well have remained no more than wishful thinking. He will sorely be missed.

My mother. God only knows how she put up with me for so long, but everything I am today, for better or worse, is the direct result. My father. For never telling me what he thought I should do and yet providing the guidance to make the choices so easy, obvious and clear. By their profound achievements – family, academic, business and humanitarian – they define the word synergism.

My wife. Without whom nothing is possible.

Table of contents

List of figures

List of tables

Chapter 1: Introduction

I. General:

The examination of the potential impact of hemodynamics and atherosclerosis has been coupled for some time. The hallmark of atherosclerotic vascular disease, the gradual occlusion of a blood vessel's cross section, is altered flow. As atherosclerotic vascular disease is the leading cause of mortality and morbidity around the world, many have sought to understand how atherosclerotic lesions, form, grow and destabilize based on fundamental fluid dynamics. This work proposes an alternative means of analyzing the types of fluid dynamic interactions that could contribute to atherosclerotic disease.

II. Relationship of atherosclerosis to fluid mechanics:

Early workers in the field of atherosclerosis research noticed a unique phenomenon: Despite the systemic factors such as tobacco abuse, hypertension, and diabetes that place patients at risk of developing atherosclerosis, the distribution of atherosclerotic lesions is far from uniform and often predictably localized to specific regions of the arterial tree[1]. Regions in and around bifurcations[2] and bends in the arterial tree have a considerably higher atherosclerotic plaque burden than other locations even those only one or two diameters away. These observations, have led to the school of thought that attributes at least part of the disease to fluid mechanic stimuli[3]. Since the properties of flow patterns change quite considerably over the relevant length scales, it seems appropriate to attribute the progression of disease and especially the early part which would determine it's localization to the interplay of forces and flows between the blood flowing in the arteries and the arterial wall.

Whatever the flow pattern in the vessel is, the actual transduction of force to the vessel wall is through the shear stress, which is by definition the force per unit area exerted by the fluid on the vessel wall. It is thus reasonable to begin to look for potentially deleterious flow patterns in those that produce abnormalities in shear stress[4]. The importance of shear is further reinforced by the concentration of atherosclerotic plaque in regions of the vascular bed that have abnormally high and low shear stress, bifurcations.

Several characteristics of flow have been proposed over the years as a stimulus for the development of atherosclerotic disease. It was initially proposed that abnormally high shear stress cause disruption damage and denudation of the endothelial cell layer[1,5]. Endothelial dysfunction is a primary factor in the initiation and propagation of atherosclerotic lesions. Yet, examination of the bifurcations themselves shed light on this theory. Bifurcations possess regions of abnormally low and high shear stress, the highest values being found around the flow divider region. However, it is the high shear regions of bifurcations that are typically spared of the common elements of atherosclerosis including lipid deposits, inflammatory cells, fibrosis, etc.

Thus, rather than a specific shear event, turbulent flow patterns[6,7] were thought to explain the observed localization of lesions, through damage to the endothelium as well, and deposition of different blood-borne products onto the vessel wall. The difficulty is that it is rare to encounter conditions under which laminar flow becomes turbulent within the arterial bed. Arterial flow rates do vary but in general the Reynolds numbers[i], are well below the upper critical value at which laminar flow can be expected to turn turbulent, and are typically less than the lower critical Reynolds number at which turbulence is expected to die out and revert to laminar flow. Thus, while turbulence might exist at very specialized locations, for example immediately downstream from heart valves and in some locations in the ventricles, as a general rule turbulence would not be expected to prevail in the arterial bed, and certainly not to the extent that would explain the wide distribution of atherosclerotic disease[8].

Given these facts, the focus has shifted from high shear regions to low shear regions[9-11]. Low shear can abrade the endothelium and directly affects gene expression patterns and the function of endothelial cells[12,13]. A bifurcation can exhibit several regions of lower shear stress. Most prominent of these are the two regions of boundary layer separation that exist in the lateral angles of the bifurcation[14]. Stretching from stagnation point to point of reattachment, these two areas are ones in which the shear stress is abnormally low throughout. This has led several workers to suggest a direct link between localization of atherosclerosis and regions of boundary layer separation[15]. Other

---

[i] See subsequent discussion of dimensionless parameters.

features of the flow in separated regions have also been proposed as possible promoters for atherogenesis, these include both reverse and pulsatile (non-uniform) shear stress and have been shown to correlate with the localization of atherosclerotic plaques in vivo[16].

The importance of low shear stress is consistent with the evolving view of atherosclerosis as an inflammatory process[17], wherein the progression of atherosclerosis is governed by a series of reactions between the vessel wall and a multitude of blood-borne inflammatory cells, particles and proteins. The characterization of these reactions and the factors that determine their progression is a complex science. However, one must keep in mind that the interaction of the inflammatory cells with the vessel wall does not happen in a vacuum. Rather, throughout these events the inflammatory cells and the vessel wall itself are subjected to varying forces exerted on them by the arterial architecture and flowing blood. These forces will determine to a large extent the properties of the endothelial lining through which the inflammatory cells must traverse, the forces acting on them as they attempt to breach the vessel wall and indeed which and how many cells arrive at any given location to begin with.

This view of atherosclerosis lends itself especially well to the relation of fluid mechanic phenomena, particularly low shear stress and boundary layer separation, to atherogenesis and the progression of atherosclerotic disease. The process of inflammatory cell penetration of the endothelial cell layer is not an instantaneous one by any means. Rather, it is a gradual, multi-stage process that takes place over numerous cycles of flow. Throughout this process, the cells are subjected to forces exerted on them by the vessel wall, by adjacent cells and also by the flowing blood. At least in the initial stages, the adherence of these cells is passive and thus whether or not the cells eventually bind and penetrate the vessel wall, or on a global scale, the probability and hence the number of cells which ultimately breach the vessel wall, is determined by the balance of forces that bind cells, and those forces which would tear them away. These latter forces, which retard penetration of the vessel wall, are no more than an expression of the shear stress, would be reduced in regions where for whatever reason the shear stress is abnormally low. Furthermore, regions of boundary layer separation, which include re-circulating and sluggish flows, would increase residence times for the inflammatory agents near the vessel wall. This would allow more time for the reactions to occur and reach the point

10

where the cells take on a more active migratory nature and contribute further to the progression of atherosclerotic disease.

Other more detailed models of the interactions of flow with the arterial wall have focused on oscillatory, bi-directional and spatially and temporally alternating flow patterns[16]. One could easily make a link between atherogenesis and any altered flow pattern. Endothelial cells have been shown to be adapted to the local flow conditions that they encounter. One example of this type of adaptation is the morphologic appearance of these cells[18]. Cells that are subjected to high, yet physiologic, flows tend to have an elongated appearance when viewed en-face, with the long axis oriented along the direction of flow. Conversely, cells that are subjected to more static conditions tend to be more rounded[18]. In a system as intricately evolved as this, it seems reasonable to assume that endothelial cells are specifically suited to whatever the flow conditions at their location happen to be. Assuming this to be the case, one would expect that any alteration in the flow pattern, be it direction, velocity, a higher or a lower shear stress or any other change from what the cells in that particular location have been conditioned for, would have a negative effect on endothelial cell function.

Whatever the mechanism of action, one cannot ignore the simple phenomenological correlation between regions of boundary layer separation and development of atherosclerotic disease. Some studies[19] have gone as far as showing not only a one-to-one correlation in the localization of these two factors, but actually a striking resemblance in the physical shape of the region of separation and the subsequent atherosclerotic lesion that develops. This resemblance is so extensive, especially around bends and bifurcations, that one is led to think of mechanisms whereby the separated flow triggers atherogenesis, and the lesion develops until it fills the entire original space taken up by the separated flow. It is these observations that prompted the present work to focus on boundary layer separation. An implicit assumption is made, that any process that tends to reduce the extent of flow separation is beneficial, whereas any process that tends to enlarge it is deleterious in its effects.

III. Modalities of treatment:

The end result of the long course of vascular disease will in most cases be luminal occlusions that jeopardize organ perfusion to such an extent as to necessitate corrective or bypass procedures. It is worthwhile noting that these luminal occlusions need not be complete, or nearly complete to exert a significant effect on the organ. One explanation for this fact lies in an appreciation of the fluid mechanic principles involved. As will be discussed later, the resistance to flow of an arterial segment[i] is under ideal situations inversely related to the fourth power of the diameter of the segment. Thus, even a modest decrease in diameter can have a drastic effect on the resistance to flow of the artery, and hence the amount of blood which it delivers. A second explanation has to do with the morphology and natural history of atherosclerotic lesions. Some lesions may, at certain points become unstable and rupture, exposing cells and tissues and releasing agents to the circulation with dramatic effects. There is evidence that the unstable lesions that rupture are less likely to be the ones that present a substantial luminal occlusion or reduction in cross-sectional area.

Corrective procedures might take the form of bypass grafting or angioplasty e.g. from percutaneous procedures known as Percutaneous Transluminal Angioplasty (PTA). During bypass grafting, an alternative flow channel[ii] is used to divert flow from a point upstream or proximal to the lesion to a point on the vessel that is downstream or distal to the lesion. During angioplasty, the artery is dilated to approximate its original dimensions and flow is restored downstream in the vessel.

The long term efficacy and benefit of these procedures is a topic of intense investigation and debate. The relative advantages and disadvantages of one procedure over the other are of tremendous clinical importance but also in many cases unclear. Regardless, the most common mode of failure of these two treatment modalities is similar – accelerated occlusion of the new flow channel. In the case of bypass grafting this is

---

[i] The resistance to flow is inversely related to the amount of flow going through the segment in a parallel circuit such as the arterial tree.

[ii] The sources for this channel are numerous and include the saphenous vein from the leg, the radial artery from the arm and the internal mammary artery from the chest, as well as research efforts into artificial sources.

commonly referred to as graft occlusion, whereas in the case of angioplasty this is known as restenosis.

IV. Prior Work:

A large body of experimental evidence has been assembled regarding the flow in different parts of the arterial tree and especially that which exists in and around arterial bifurcations. This work includes analytical analysis, modeling by use of mock circulation systems as well as numerical analysis. Each one of these approaches has its advantages and its limitations:

Analytical work is the most precise and can give perhaps the most insight and intuition into the problem. Unfortunately, the full Navier-Stokes equation that governs flow in the relevant regime of intermediate Reynolds numbers is complex and can only be solved analytically for a handful of highly simplified geometries. This leaves the latter two methods – numerical analysis and physical modeling. Of these two, numerical analysis is clearly the more flexible as it allows for changing of the parameters that characterize the problem virtually instantly. However, numerical analysis is of lesser accuracy at the singular points of flow unsteadiness and separation[20]. Since these are the points at which the phenomena of interest here occur, this presents a severe limitation to the applicability of the results. The second limitation of numerical analysis is that while it is for the most part well suited for the solution of partial differential equations which govern the flow, it runs into great difficulties in predicting things such as the particle sedimentation patterns in these flows, as these problems include an inherent stochastic element. Physical modeling is a highly refined method dating back at least 1872 when William Froude built the first towing tank to test the resistance of ocean vessels. It is however not without its own limitations, the major ones being the fact that it is time consuming, the relative difficulty associated with altering the parameters modeled and the inherent inaccuracies stemming from physical limitations of the modeling apparatus.

Since the central role of bifurcations was identified early on, analytical[21], numerical[20,22-24] and physical modeling[19,25-27] methods have all been employed to the analysis of bifurcations. Typical sites examined have been the left main coronary bifurcation[22], the carotid bifurcation[27], the pulmonary artery bifurcation[28] and the main

13

aortic bifurcation. Experiments typically map different flow parameters in the region such as flow vectors, pressure gradients, shear rates and shear stresses along the artery wall as well as others. While extensive, these models all share several common characteristics. This set of common characteristics coincides with a resultant shared set of limitations, which shall be discussed hence.

Past models have all been similar in that they:

a) usually simulate conditions in healthy arteries, that is, before lesions have actually formed[22].

b) are often highly specialized to specific situations such as a T-bifurcation, a symmetric bifurcation etc. To mimic the specific case in question input flow parameters, such as flow rate and pressure profile, and the physical properties of the model, e.g. relative diameters, bifurcation angles etc. are determined as precisely as possible[19,20,26].

c) concentrate on what has been perceived as the "causal" effects, i.e. the effects distal to the bifurcation in one specific independent branch.

d) are "static", modeling the system at one point in time, and do not allow for the long term remodeling of the system that occurs in the natural case[25].

These common features also provide a set of respective limitations to their applicability:

a) While providing valuable insight into the process of atherogenesis, and helping to explain areas of high risk, this type of work is of limited clinical application. High-risk areas may be identified but clinical intervention before significant lesions have occurred is unlikely.

b) Since each actual clinical case is unique, the value and applicability of a highly specialized model is severely limited. That is to say that the chances in any one clinical setting that the geometrical attributes of a patient's disease will coincide with a case which has been modeled are extremely remote. For this reason, the knowledge gained has had a limited effect on the practices of clinicians presented with a wide range of specialized cases but no concise set of general guidelines.

c) Models that examine only down-stream vessels ignore the potential impact on the larger and possibly more clinically important proximal vessels.

d) Static systems ignore the long-term dynamic nature of the arterial system, which enables it to respond to ever changing conditions by continuously re-modeling itself.

14

V. Time course of disease and response to intervention:

An important issue to appreciate is the time course of the different processes involved in atherosclerotic disease. The progression of the disease itself is quite slow. Precursors of atherosclerotic lesions can readily be identified in healthy individuals in their early twenties. Observations have been made of fatty streaks, the very earliest form of atherosclerotic lesions, in children as young as two to four years of age. However, normal adults[i] do not typically become symptomatic until their mid to late fifties. The natural progression of atherosclerotic lesions is a slow and gradual one, taking anywhere from thirty to fifty years and perhaps even longer to develop.

The changes in the arterial wall imposed by bypass or angioplasty are entirely different however. These changes take place over the course of what amounts to minutes to hours. The response of the tissue to these rapid changes can be expected to vary greatly from that to the disease itself. A system that has been designed to deal optimally with events that occur over the course of many years in an optimal manner can be expected to react in a sub-optimal and perhaps even deleterious manner to changes on this vastly shorter time scale. One possible manifestation of this effect might be restenosis, which runs on a much shorter time scale of months to years as opposed to the decades over which the original disease developed. When considering the effects of interventions it is thus helpful to view the arterial system as one that is normally in a quasi-steady state very close to equilibrium, and has suddenly been thrust much further away from the equilibrium point than it would normally be.

VI. Interactions between different sites in the arterial tree:

In the clinical setting, lesions in individual arteries have typically been treated as separate and independent events. While the presence of lesions in multiple sites is certainly an indication for choosing one type of treatment modality over another, the continued progression of lesions in segments that were not manipulated has not been attributed to interactions between these sites, but rather to the underlying systemic disease manifesting itself in several locations. Similarly, the occurrence of lesions, either

---

[i] By normal here we mean ones that do not suffer from diabetes mellitus or any other form of genetic or environmentally caused disease that predisposes them to accelerated atherosclerosis at a young age.

de-novo or as a progression of prior ones, over time has typically not been attributed to a causal relationship between them or to a result of an intervention but rather further symptoms of an already established disease.

Consequently, the treatment of lesions has been on an individual basis with little regard to the effects that treatment of one site might have on another. Furthermore, the long-term follow-up of patients who were treated with one form of intervention or another has focused on the site at which the intervention was performed. A demonstration of this point is the fact that one of the most common criteria for the evaluation of efficacy of a treatment modality over time is the rate of "target lesion revascularization".

The basis of this thesis is the assertion that this view is an oversimplification of the problem. The reasons for this assertion can be broken down into three main factors:

1. We first examine a vastly oversimplified analogy for a fluid flow circuit – that of a completely passive electrical circuit:
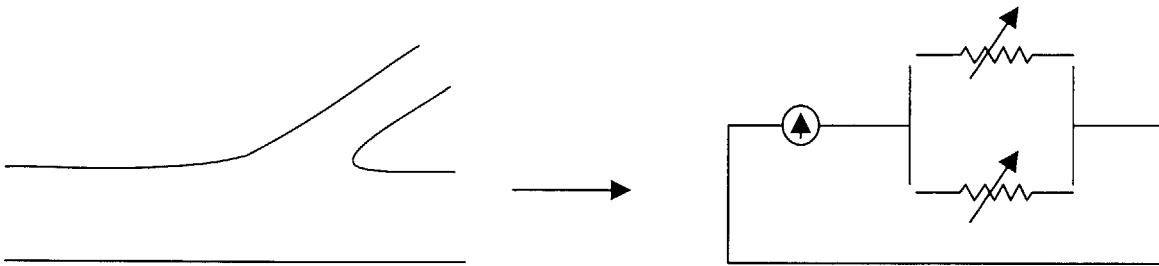
Figure 1-1: Simple electric analogy for flow

In this analogy, a lesion in a branch is simulated by raising the resistance of the appropriate resistor. Re-adjusting the value of the resistance down towards its original value simulates dilation of this lesion. Clearly, any change in the resistance on one branch will have an effect on not only the flow in that branch but also on the flow through the contralateral one.

2. In the case given above, each flow branch is modeled by an entirely passive circuit element. In reality, the case is much more complex: Each vessel segment posses a fluid dynamic impedance, which is a generalized dynamic resistance taking into account the compliance of the vessel, the inertia of the fluid and the frequency of oscillations. This impedance is different from the circuit above in that while electrical resistors have set impedance regardless of the circuit they are placed in, the impedance of a vessel is

dependant on the flow patterns it is subjected to. Any change in one part of such a circuit will necessarily effect a change in the flow patterns through other parts of the circuit and hence change the impedance of these other channels thus altering the flow patterns further. In this manner, a complex interaction is set up between any part of the flow circuit and all other parts.

3. Real arteries are composed of living tissue and are not simply solid tubes. They have the capacity to adapt and react to changing flow conditions. It is the assumption of this work that under normal conditions, these adaptations optimize the entire flow system from the perspective of some crucial parameter such as energy consumption or tissue perfusion. Under abnormal conditions there could be a derailment of these adaptive mechanisms and adverse results.

Regardless of what guides these adaptations, the end result is that intervention on one site might under certain conditions set off a host of adaptive responses in other sites. As the effects are fluid dynamic, the impact may be observed downstream from the site of intervention, upstream from it, or in a parallel flow channel. Some of these interventions might trigger a problem of considerably larger implications than that which they attempted to solve, for example if an intervention in one site has an adverse effect on a more proximal vessel. In other, less extreme cases, the type of intervention and the manner in which it is performed would surely benefit from a more complete understanding of the interactive processes involved so as to produce a more favorable long term result.

VII. Experimental scenario:

To demonstrate this approach, a specific clinical scenario was outlined to simulate the progression of disease, the clinical intervention performed and the possible long-term outcomes. It is crucial to note that this scenario in no way attempts to model the most prevalent clinical situation. Nor does it attempt to model precisely any specific type of intervention. In fact, no attempt has been made to accurately model any real-world situation at all. The sole purpose of the scenario is to provide a framework through which the types of interactions discussed can be examined individually and their impact

precisely analyzed and rigorously demonstrated. This scenario is the backbone of the set of experiments performed:

1. Basic bifurcation geometry:

    The basic geometry of a bifurcation includes an inherent fluid mechanics problem. On a theoretical basis alone one would expect two regions of flow separation to form (see fig. 1-2). The first region forms in the ostium of the side branch. This separation can be understood in several ways but perhaps the most intuitive is the point of view of inertia. That is to say that the blood flowing down the main branch simply has too much inertia to negotiate the sharp bend on the lateral wall of the bifurcation. The second region of separation forms in the main branch[i] facing the ostium of the side branch. This can be understood in several ways: One is to think of it as a result of the take-off of blood into the side branch that diverts all streamlines away from the wall. This is however somewhat misleading as it predicts that at a zero degree angle of bifurcation – the case in which one channel simply divides into two parallel channels – one would not see this region of separated flow – a result that is false[21]. Perhaps the more correct way of thinking of this region of separation is to consider the flow in the main branch against an adverse pressure gradient created by the imposition of a new boundary layer – that which forms along the flow divider.
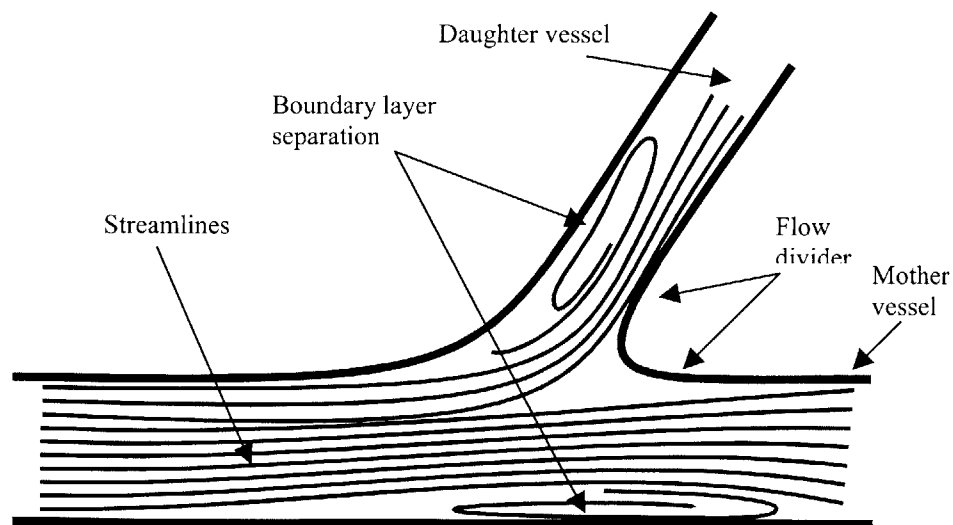
Figure 1-2: Flow through a simple bifurcation – regions of boundary layer separation.

---

[i] During the course of this thesis we will be using the terms "main branch" and "mother branch" and the terms "side branch" and "daughter branch" interchangeably.

2. Tapered bifurcation:

In reality, major bifurcations[i] do not normally appear as in fig. 1-2. Rather, most bifurcations include a tapering of the lateral wall of the mother branch from approximately the point that faces the ostium of the daughter branch. This is demonstrated in fig. 1-3.
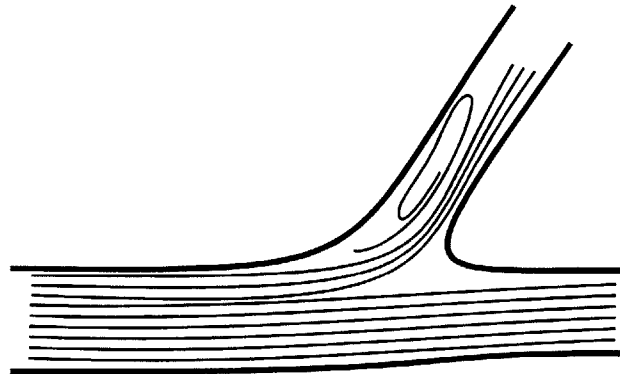
Figure 1-3: Flow through a tapering bifurcation

One possible explanation for the benefit of this geometry is that by approximating the curvature of the streamlines with the vessel wall itself, the artery reduces or perhaps eliminates the region of flow separation in the main branch. Note however that the region of separation in the side branch still exists, as approximating the streamlines with the vessel wall at this point would severely reduce the diameter of the daughter branch. This is indeed where most of the lesions in bifurcations actually occur.

3. Lesion in daughter vessel:

Flow separation in the ostium of the daughter vessel produces, a lesion. Because the progression of disease is very gradual, the system has time to react adaptively to the slow occlusion of the side branch. This can be done in a number of ways including alterations in the downstream resistance i.e. the vascular bed, development of collateral circulation (see fig. 1-4) as well as shifting of the input flow patterns to the system itself (by shunting flow away from other sites for example). Whatever these adaptations turn out to be, the original cause of boundary layer separation in the

---

[i] The term "major" refers to those bifurcations where the diameter of the daughter branch is not insignificant with respect to the diameter of the mother branch.

19

mother vessel, take-off of flow at the bifurcation, no longer exists. The tapering of the mother vessel now serves no advantageous role and is actually detrimental as it needlessly increases the resistance to flow of the mother branch. It is reasonable to assume then that the system will adapt in such a way as to eliminate this tapering. It is even conceivable that due to the increased pressure in the region of the bifurcation the artery might actually bulge out at this point (see fig. 1-4).
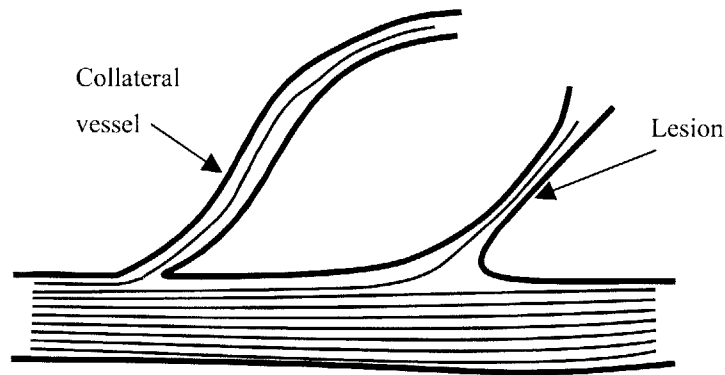
Figure 1-4: Flow through bifurcation with lesion in daughter branch. Note development of collateral circulation as well as the elimination of taper in the mother branch facing the ostium.

Note that in this new configuration boundary layer separation has been minimized, perhaps eliminated. There is of course still a perfusion problem to the region that was served by the daughter vessel.

4. Dilation of daughter branch:

   The assumption made when dilating a lesion is that one is returning the system to its original configuration. If however we take into account the fact that the system has adapted to the changing conditions over the course of the disease as it has here, it becomes clear that by dilating the lesion one actually creates a completely new configuration. In this new configuration, the other parts of the system are no longer optimized for the conditions with which they are presented and one possible manifestation of this could be the re-establishment of a region of separation in the main branch as depicted in figure 1-5. In other words, restoration of the original anatomy or vascular architecture may not restore the initial or optimal flow conditions.
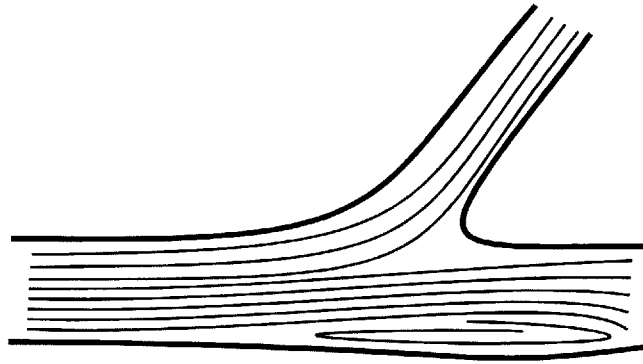
Figure 1-5: Dilation of daughter branch. Note formation of new area of
boundary layer separation in mother branch due to non-optimized flow.

At this point, one must consider the previous discussion of time scales. A system which normally reacts to changes in the flow regime that take place over the course of years to decades, is now presented with a vast alteration in flow over the course of minutes to hours. The biological reaction to such a change can be expected to be different from the controlled normal reaction. Rather, the system might react in an uncontrolled manner to produce a lesion in the main branch rather than stopping at a mild taper.

The experiments outlined in this thesis track this general scenario and demonstrate the properties of flow at each stage. Flow is analyzed using several different tools to both verify the theoretical predictions made above, and to attempt to predict what their implications might be. This is done in a manner that does not attempt to be true to any specific set of parameters measured in a real case, or even those indicated by taking an average of all cases. Rather, it is performed in a generalized manner so as to attempt to tease out the underlying qualitative rules that govern these processes regardless of the data pertaining to the individual case.

Chapter 2 outlines the methods by which the flow model was built and analyzed. Chapter 3 presents the experiments performed and analyzes the results obtained. Chapter 4 contains conclusions and suggestions for future work.

VIII. References:

1. Texon M. A Hemodynamic Concept of Atherosclerosis, with Particular Reference to Coronary Occlusion. *A.M.A. Archives of Internal Medicine.* 1957;99:418-427.
2. Roach MR. The effects of bifurcations and stenoses on arterial disease. In: *Cardiovascular flow dynamics & measurements.* Baltimore: Park Press; 1977.
3. Giddens DP, Zarins CK, Glagov S. The role of fluid mechanics in the localization and detection of atherosclerosis. *Journal of Biomechanical Engineering.* 1993;115:588-594.
4. Krams R, Wentzel JJ, Oomen JAF, Vinke R, Schuurbiers JCH, De Feyter PJ, Serruys PW, Slager CJ. Evaluation of Endothelial Shear Stress and 3D Geometry as Factors Determining the Development of Atherosclerosis and Remodeling in Human Coronary Arteries in Vivo. *Arteriosclerosis Thrombosis and Vascular Biology.* 1997;17:2061-2065.
5. Fry DL. Acute Vascular Endothelial Changes Associated with Increased Blood Velocity Gradients. *Ciculation Research.* 1968;22:165-197.
6. Fergusson GG, Roach MR. Flow Conditions at Bifurcations as Determined in Glass Models with Reference to the Focal Distribution of Vascular Lesions. In: Bergel DH, ed. *Carsiovascular Fluid Dynamics.* Orlando.: Academic Press Inc.; 1976:141-157.
7. Gutstein WH, Farrell GA, Armellini C. Blood flow Disturbance and Endothelial Cell Injury in Pre-Atherosclerotic Swine. *Laboratory Investigation.* 1973;29:134-149.
8. Glagov S, Zarins C, Giddens DP, Ku DN. Hemodynamics and Atherosclerosis. Insights and Perspectives Gained From Studies of Human Arteries. *Archives of Pathology and Laboratory Medicine.* 1988;112:1018-1031.
9. Friedman MH, Deters OJ, Bargeron CB, Hutchins GM, Mark FF. Shear-Dependent Thickening of the Human Arterial Intima. *Atherosclerosis.* 1986;60:161-171.
10. Sabbah HN, Khaja F, Brymer JF, Hawkins ET, Stein PD. Blood Velocity in the Right Coronary Artery: Relation to the Distribution of Atherosclerotic Lesions. *American Journal of Cardiology.* 1984;53:1008-1012.
11. Gibson MC, Diaz L, Kandarpa K, Sacks FM, Pasternak RC, Sandor TS, Feldman C, Stone PH. Relation of Vessel Wall Shear Stress to Atherosclerosis Progression in Human Coronary Arteries. *Arteriosclerosis and Thrombosis.* 1993;13:310-315.
12. Davies PF. Mechanisms involved in endothelial responses to hemodynamic forces. *Atherosclerosis.* 1997;131 Suppl:S15-7.
13. DePaola N, Gimbrone MAJ, Davies PF, Dewey CF. Vascular endothelium responds to fluid shear stress gradients. *Arteriosclerosis & Thrombosis.* 1992;12:1254-1257.
14. Fernandez RC, De Witt KJ, Botwin MR. Pulsatile Flow Through a Bifurcation with Applications to Arterial Disease. *Journal of Biomechanics.* 1976;9:575-580.
15. Fox JA, Hugh AE. Localization of Atheroma: A Theory Based on Boundary Layer Separation. *British Heart Journal.* 1966;28:388-399.
16. Moore JE, Xu C, Glagov S, Zarins CK, Ku DN. Fluid wall shear stress measurements in a model of the human abdominal aorta: oscillatory behavior and relationship to atherosclerosis. *Atherosclerosis.* 1994;110:225-240.
17. Ross R. Atherosclerosis - An Inflammatory Disease. *New England Journal of Medicine.* 1999;340:115-126.
18. Fry DL. Responses of the Arterial Wall to Certain Physical Factors. In: *Atherogenesis: Initiating Factors:* Assosciated Science Publishers; 1973:93-121.
19. Asakura T, Karino T. Flow Patterns and Spatial Distribution of Atherosclerotic Lesions in Human Coronary Arteries. *Circulation Research.* 1990;66:1045-1066.
20. Perktold K, Hofer M, Rappitsch G, Loew M, Kuban BD, Friedman MH. Validated Computation of Physiologic Flow in a Realistic Coronary Artery Branch. *Journal of Biomechanics.* 1998;31:217-228.
21. Zamir M, M.R. R. Blood Flow Downstream of a Two-dimensional Bifurcation. *Journal of Theoretical Biology.* 1973;42:33-48.
22. He X, Ku DN. Pulsatile Flow in the Human Left Coronary Artery Bifurcation: Average Conditions. *Journal of Biomechanical Engineering.* 1996;118:74-82.

23. Rindt CCM, Steenhoven AA. Unsteady Flow in a Rigid 3-D Model of the Carotid Artery Bifurcation. *Journal of Biomechanical Engineering*. 1996;118:90-96.

24. He X, Ku DN, Moore JE, Jr. Simple calculation of the velocity profiles for pulsatile flow in a blood vessel using Mathematica. *Annals of Biomedical Engineering*. 1993;21:45-9.

25. Malcolm AD. Flow Phenomena at Bifurcations and Branches in Relation to Human Atherogenesis: A Study in a Family of Glass Models. In:: University of Western Ontario; 1975.

26. Friedman MH, Kuban BD, Schmalbrock P, Smith K, Altan T. Fabrication of Vascular Replicas From Magnetic Resonance Images. *Journal of Biomechanical Engineering*. 1995;117:364-366.

27. Bharadvaj BK, Mabon RF, Giddens DP. Steady Flow in a Model of the Human Carotid Bifurcation. Part I - Flow Visualization. *Journal of Biomechanics*. 1982;15:349-362.

28. Yoganathan AP, Ball J, Woo YR, Philpot EF, Sung HW. Steady Flow Velocity Measurements In a Pulmonary Artery Model with Varying Degrees of Pulmonic Stenosis. *Journal of Biomechanics*. 1986;19:129-146.

Chapter 2: Materials and methods

This chapter will discuss the common methods used for all the experiments described in this thesis. The next chapter, which deals with specific experiments, will discuss the methods unique to each experiment and its result. Part one of this chapter will describe the fabrication of the physical flow model and it's operation. Part two will discuss the instrumentation used to perfuse, record and analyze flow through this model. Part three will deal with the general method for visualization of flow. Part four deals with dimensionless analysis and how it relates to the experiments performed here.

I. Fabrication and operation of mock circulation

The flow model is formed in a Plexiglas container filled with a clear silicone compound, into which cavities in the shape of different geometries in the arterial tree have been formed. Fluid is perfused through these cavities to simulate blood flow. Adjacent to these cavities are pneumatic spaces that can be inflated and deflated to compress adjacent flow channels. Silicon plungers function as pneumatic "pusher-pullers", so as to enable a dynamic alteration in flow channel geometry to simulate different disease states and/or clinical intervention schemes.
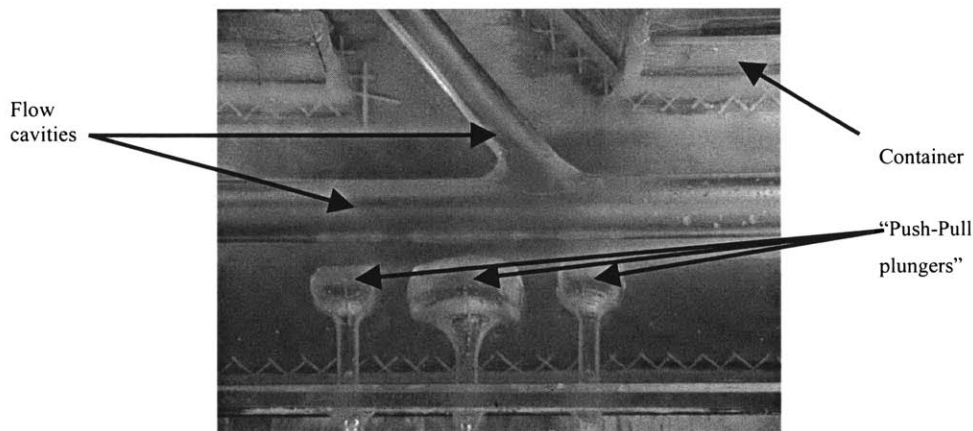
Figure 2-1: Flow model. Chamber, flow cavity and pneumatic "pusher-pullers" are indicated
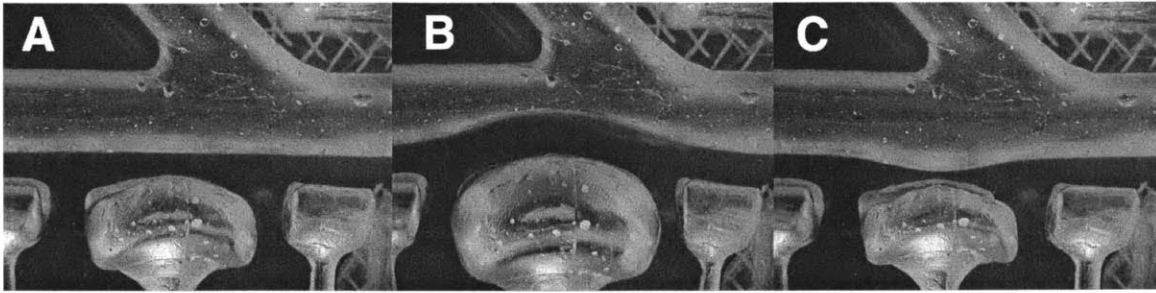
Figure 2-2: Operation of "push-pull plungers". (A) Device is deflated for normal geometry. (B) Device is pressurized to create lesion. (C) Vacuum is applied to create aneurysm.

The flow model is created in three main steps:

1. Creation of a solid cast of the flow channels and pneumatic spaces.

2. Fixation of solid cast in container and embedding in silicone.

3. Melting of the cast out of container to create flow channels/pneumatic spaces, and connection to external flow/pressure channels.

I.1 Creation of solid cast:

The material for the solid cast must be pliable enough to be shaped into smooth, non-obstructive flow models that are similar to arteries in their geometry and internal properties, and able to be melted out of the silicone without affecting its essential properties, such as optical clarity for flow imaging. Unfortunately, these properties are difficult to reconcile in one material. Initially wax was embedded directly into the silicone and melted out. Unfortunately, the petroleum present in wax softens the wax and reacts with the silicone when heated causing it to become opaque. Thus, a staged process was used that included first formation of the initial cast from wax, then formation of a polyurethane mold and finally cast pouring.

I.1.a. Formation of initial cast from wax: Sculptor's microcrystalline wax was used to create the cast as it is soft and pliable when heated, allowing molding into virtually any shape. When cooled, it becomes hard and smooth and the shape can be retained. Small pieces of the wax were heated to 75°C for approx. 4 minutes, and after slight cooling could then be rolled and kneaded into the required shapes. Bifurcations were formed by

25

joining two cylinders of wax and filling in the creases, and push-pull plungers were formed by connecting a small cylinder or hemi-cylinder to a long stem. Final shaping was performed when the wax had cooled completely to achieve as smooth a finish as possible.
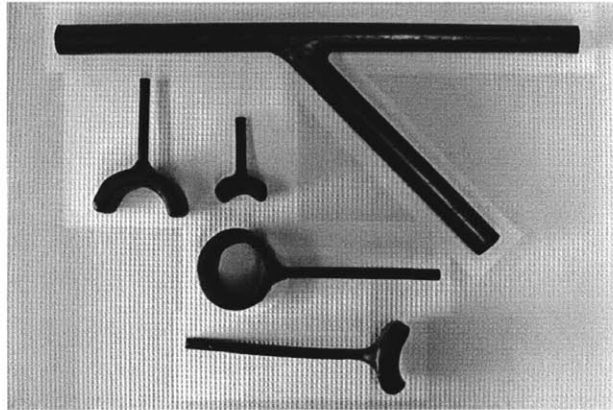
Figure 2-3: Wax casts. Bifurcation model seen at top. Several push-pull plungers including concentric, one-sided and semi-circular are shown.

I.1.b. Formation of polyurethane mold: Since wax cannot be melted out of the silicone without altering its optical properties, and the PEG that is ultimately placed in the silicone can be poured but not shaped, a mold is required to transfer the cast from one material to the other. The material for formation of this mold was a two part polyurethane compound, Smooth-On PMC-121/30 Dry. The normal PMC-121/30 compound exudes a mold release material that dissolves the wax. A container for holding the wax and polyurethane was assembled and sealed. The wax piece was suspended inside the container and aligned along a horizontal plane that passes through the entire wax piece. Long pieces were supported from below to prevent sagging.
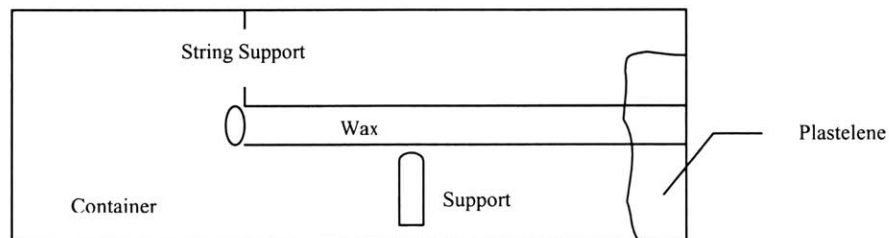
Figure 2-4: Suspension of wax cast prior to polyurethane pouring

Polyurethane was mixed and poured into the container up to halfway up on the wax piece and then allowed to set partially. Plastic cylinders of approx. ½cm diameter and 6cm length were halfway submerged in the partially cured polyurethane. These cylinders

would ultimately be used in aligning the two halves of the polyurethane mold. Once the bottom half of the mold was fully cured, a layer of Teflon spray, Smooth-On Mold Release, was sprayed on and allowed to dry. The second half of the polyurethane mold was poured into the container and allowed to cure. The mold was removed from the container, opened and the wax piece removed. The two halves were re-assembled using the plastic cylinders as guides for alignment.

I.1.c. <u>Pouring final cast</u>: The final cast was made of Poly(Ethylene Glycol) (PEG). The molecular weight of the PEG must be between 1000-1500 for the cast to be solid and smooth, but not brittle. The PEG was melted and poured into the polyurethane mold that had been placed vertically. Once the PEG cooled, the mold was opened and the PEG carefully removed.

The end properties of the PEG piece are highly sensitive to the temperature at which the melting was done. To produce a smooth non-brittle piece, the temperature cannot greatly exceed the melting temperature of the PEG. For the 1500 molecular weight PEG this should be no higher than 60°C.

I.2 <u>Fixation of cast and embedding in silicone</u>:

A clear Plexiglas container for the model was built and sealed using silicone sealant. The bifurcation cast as well as all of the push-pull plungers were fixed in the container prior to embedding in the silicone of the final model. A gap of at least 3 cm between the container and outer most PEG piece prevented bursting of the model from imposed pressure. The PEG pieces were interfaced to the outside tubing through the container walls using specially built glass tubes. The details of the design (see fig. 2-5) of these tubes are crucial to their function.

27
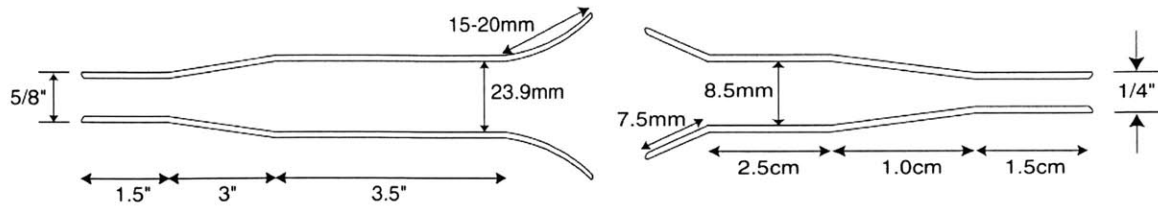
Figure 2-5: Glass interface pieces. Left – example of interface piece for bifurcation arm with internal end (the end that stays inside container) facing right. Right – example of interface piece for pusher-puller with internal end facing left.

The inner diameter of the internal end was slightly oversized relative to the external diameter of the PEG piece. The flaring out of the internal end of both pieces creates an O-ring effect that seals off the interface between the silicone cavity and the glass when the model is pressurized.
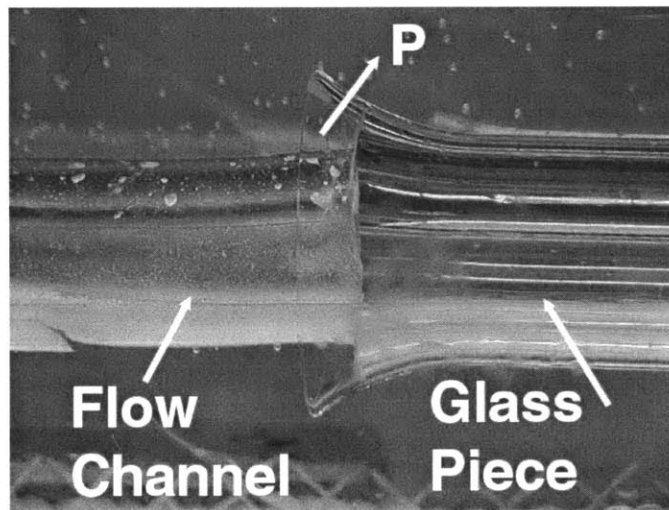
Figure 2-6: O-ring effect. In an image of the finished model, the top arrow indicates direction in which the pressure pushes the silicone on the inside of the glass interface to seal it against the flaring surface.

The mid portion of each glass tube was plugged by pouring molten PEG into it. The glass tube was then held vertically with the inner part facing up and the end of the PEG cast that was to interface with this piece inserted down to the plug. The narrow space between the PEG piece and the glass was sealed with molten PEG.
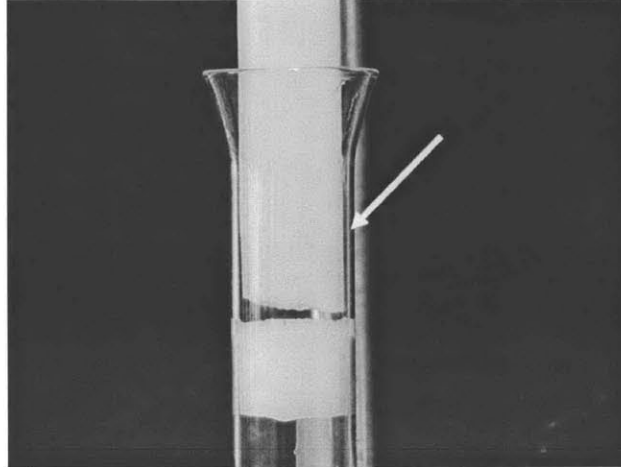
Figure 2-7: Interface sealing. One arm of PEG cast in glass tubing prior to sealing with molten PEG. PEG was poured into space indicated by arrow.

Holes were drilled in the walls of the Plexiglas container for the glass interface pieces. The interface pieces were threaded through the holes, sealed using silicone sealant and fixed in place with a ring of epoxy cement that surrounded the glass and bound it to the Plexiglas.
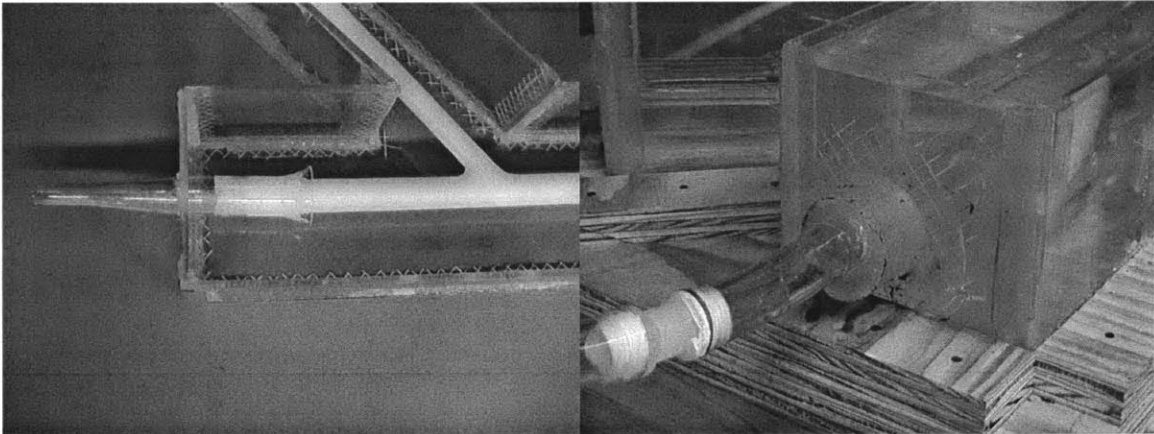
Figure 2-8: Fixation of PEG cast. Interface piece before (left) and after (right) fixation using epoxy ring.

If needed, push-pull plungers can be stabilized from above prior to pouring of bottom half of silicone. After the bottom half has hardened and prior to pouring of top half, these supports can be removed as the pusher-pullers are now stabilized by the silicone. GE Silicones RTV 6166 was mixed at a ratio of 1:2 part A to part B respectively rather than the classic 1:1 ratio so as to increase the stiffness of the model. For models of depth greater than approx. 8cm it is preferable to pour the silicone in two halves; allowing the

bottom half to cure before pouring the top half. This two part process allows air bubbles to escape to the surface before the material is fully cured.
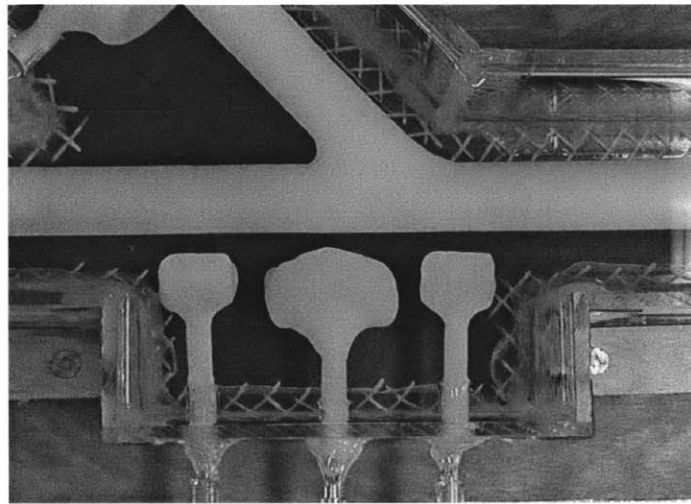
Figure 2-9: Model after curing of silicone. Bifurcation seen at top and three push-pull plungers for the main branch at the bottom.

I.3 Melting and connections:

The final step in fabrication of the flow model was melting the cast out of the silicone. The container with the silicone was mounted onto a wood backing and placed vertically in an oven heated to 70°C. This temperature is sufficient to melt the PEG but not high enough to warp the Plexiglas. Complete melting of the PEG takes overnight, and any residual PEG in the flow channels can be cleared by running hot water inside the model. Tubing from the pump was slid onto the external part of the glass interfaces. Smaller diameter tubing was slid onto the external part of the interfaces for the push-pull plungers and then connected to syringes to impose the pressure differences that inflate/deflate the plungers. The entire container was mounted to slope upwards from proximal to distal to ensure that no air bubbles would be trapped within the model segment during an experiment.

II. Instrumentation and analysis

II.1 <u>Flow circuit:</u>

The flow circuit is comprised of all parts of the experimental flow apparatus other than the silicone model itself. This includes:

1. Lower reservoir and tubing – a container with a spout at the bottom. Filled with the perfusing fluid prior to running the model.

2. Pump – Harvard Apparatus Pulsatile Blood Pump model 1423. Provides independent control over stroke volume, frequency and systole/diastole ratio.

3. Proximal tubing and ports – 5/8" PVC tubing. Ports are glass connectors that allow access to the flow. These include: collateral take-off port, pressure-wire insertion port, proximal differential pressure sensor tubing port and particle injection port.

    3.1. Collateral tube – 3/8" PVC tubing. The middle segment was made of silicone tubing to allow flow constriction and modulation. This tube runs directly from the pump to the upper reservoir.
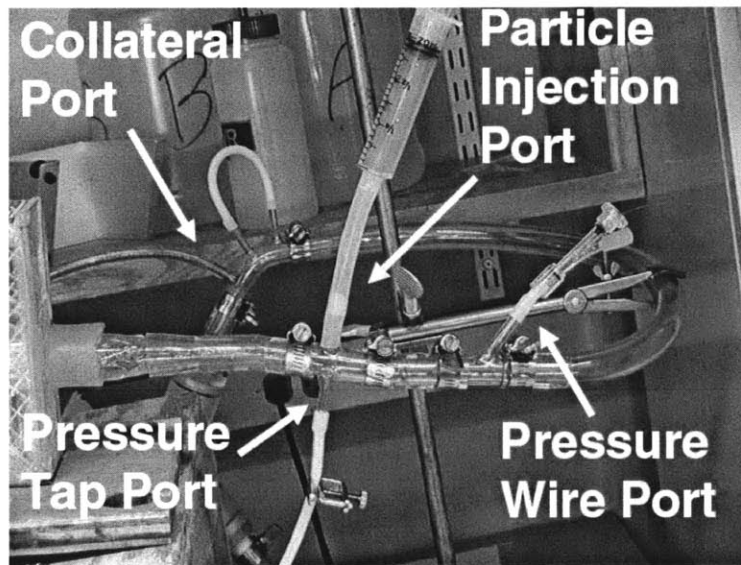
Figure 2-10: Proximal ports.

4. Flow model – described previously.

5. Distal tubing, ports and resistors – 5/8" PVC tubing leaves both branches of the model and was used to mount flow sensors. Distal to flow sensors, ½" silicone tubing on which resistors were mounted runs up to upper reservoir. Mother branch tubing can be fitted with pressure port for distal differential pressure sensor tubing in the same way as proximal port is done.

6. Upper reservoir and tubing – second container with spout at bottom and holes for insertion of distal tubing coming from model and collateral at top. The bottom spout was connected via tubing to top of lower reservoir.
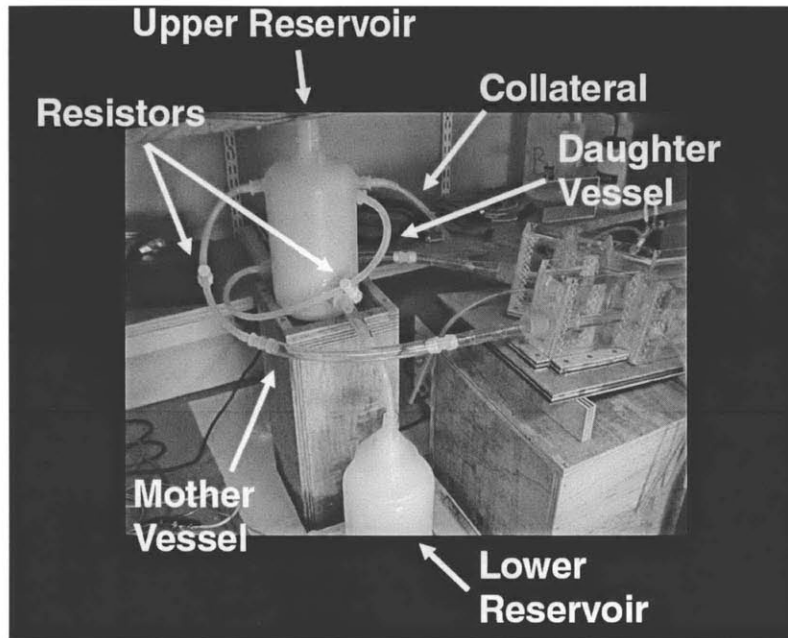
Figure 2-11: Distal tubing and reservoirs.

Perfusing fluid: 40% aqueous glycerol solution with a measured kinematic viscosity of $\nu = 0.027$ Stokes and a specific gravity of 1.1.

II.2 Flow waveform acquisition:

Transonic C-series clamp-on ultrasonic sensors interfaced into a Transonic T-206 dual sensor controller unit were mounted on both the mother and daughter vessels and flow-rate waveforms generated. The sensors were located distal to the model on the tubing connected to each one of the two glass interface pieces.

These sensors provide two advantages: first, as they were not placed within the tubing they did not affect flow. Second, they measure the flow across the entire cross-section of the tube and hence are not affected by the shape of the flow profile. The output signal from the Transonic systems controller was fed into an A/D board, National Instruments DAQ-Pad 1200, working at bipolar ($\pm 5V$) reference single ended mode. Data was displayed and recorded using National Instruments LABView software at a sampling rate of 100Hz. The total flow in the collateral, where relevant, was determined from the

difference between the sum of the integrated flows in the two branches with the collateral open and when occluded. Since the pump characteristics remain the same, the difference was assumed to be the flow in the collateral.
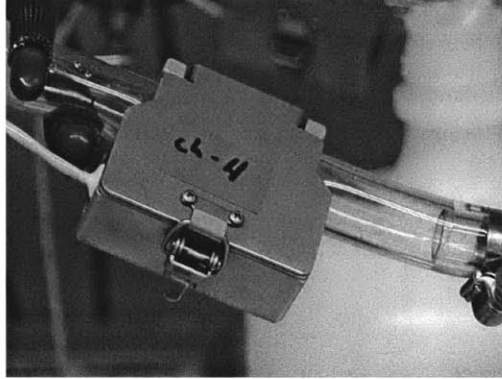
Figure 2-12: Flow sensor. Image shows Transonic ultrasonic flow sensor mounted on tubing exiting model.

II.3 Pressure waveform acquisition:

Two options were available for generation of pressure waveforms: differential pressure between two locations and referenced pressure at a point.

II.3.A. Option A – Differential pressure:

A differential pressure sensor was fabricated using a Motorola MPX10DP differential pressure sensor (pressure range = 1-1.5 psi). For a description of the amplification circuits and operation see appendix A. Pressure input to this sensor is connected via two silicone tubes leading from the pressure tap in the flow tubing on one end, to the port on the differential pressure sensor on the other. The positive terminal on the sensor was connected to the proximal pressure tap and the negative terminal was connected to the distal pressure tap. The tubes themselves were air filled and thus avoided contact of fluid with sensor interior.
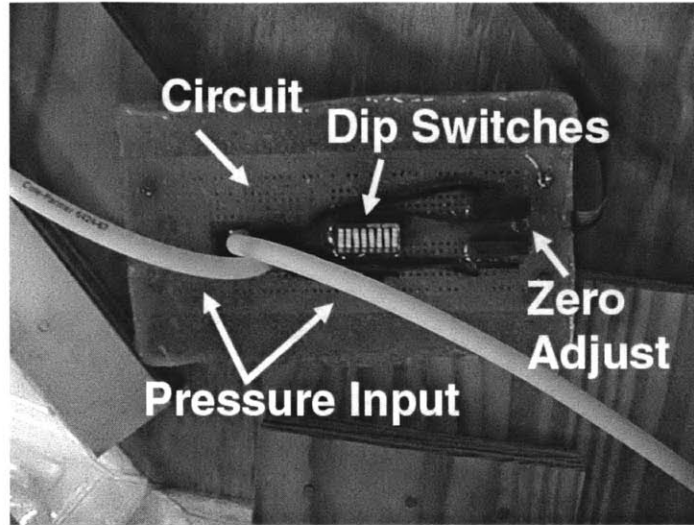
Figure 2-13: Differential pressure sensor.

II.3.B. Option B – Pressure at a point:

Another possibility for pressure measurement is to connect the proximal pressure tap to the positive terminal of the differential pressure sensor described above and leave the negative terminal open to air, or a hydrostatic column of fluid.
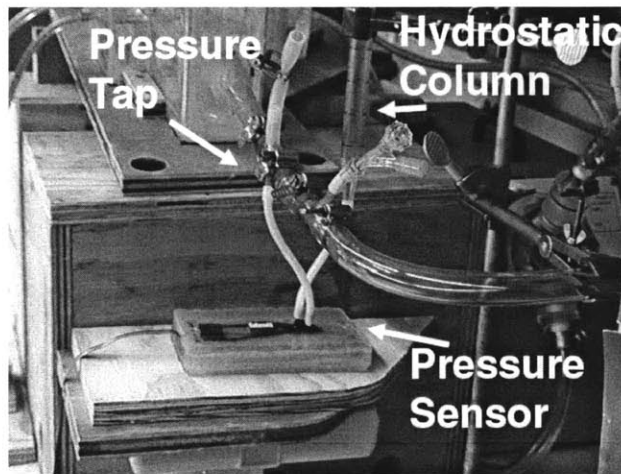
Figure 2-14: Proximal pressure measurement using differential pressure sensor.

When pressure at an internal location was needed a pressure wire, RADI Medical PressureWire (RADI, Stockholm Sweden), was inserted via the pressure wire port and advanced to the point at which pressure was to be measured. The port opening was then sealed off.
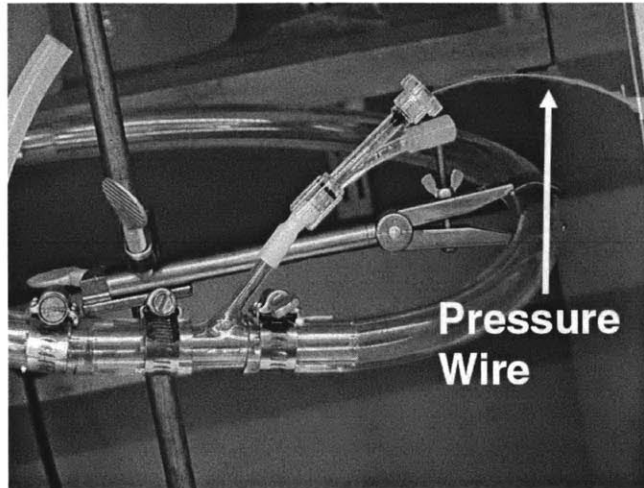
Figure 2-15: Pressure wire insertion.

The RADI controller was fed into an amplification circuit (see appendix A) and the amplified signal was fed into the A/D board.

II.4 Waveform conditioning and synchronization

Once waveforms, pressure or flow, have been recorded they are loaded into MATLAB for analysis. Most of these waveforms are noisy and are digitally filtered (see appendix B) using a low-pass filter with a cutoff frequency of 1Hz. to preserve at least the first 10 harmonics of the fundamental frequency. For experiments that include both waveform and visualization (discussed in part III of this chapter), the waveform and video timeline must be synchronized. The method for synchronization is as follows:

1. At the end of the experiment the pump is turned off suddenly during mid systole.
2. Flow is allowed to subside for approx. 30 seconds and the pump is turned back on.
3. Steps 1&2 are repeated 3 or 4 times.
4. The instant at which the pump was turned off can be identified on the pressure waveform as a discontinuous fall in pressure. Similarly, the instant at which the pump was turned back on can be identified on the pressure waveform.
5. The same events as in step 4 can be identified on the video timeline by using Adobe Premiere to search for the loud clicking sound of the pump switch.
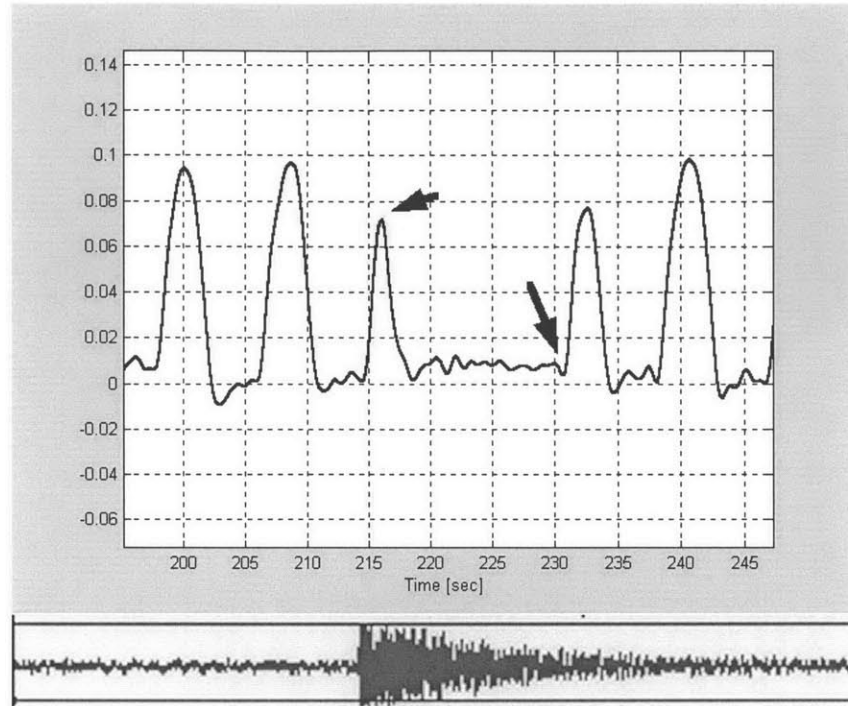
Figure 2-16: Waveform synchronization. Arrows indicate points on pressure waveform at which pump was turned off and then back on. Bottom panel shows audio file with sharp click sound caused by switch in middle.

6. The difference between these two timelines was averaged for several on/off cycles and the waveform timeline was shifted accordingly so that both timelines coincide in time.

III. General flow visualization

Generation of flow visualization was performed in two parts. Enhanced still frames of the flow were produced and then reduced to quantifiable images. This section will describe the common process of generation of the still frames. Conversion of these frames to images of flow visualization will be described in the next chapter. Generation of still frames is comprised of three aspects:

1. Formation of tracer particles
2. Filming/image acquisition
3. Image enhancement.

III.1 Formation of Tracer particles:

Polymeric microspheres were custom-made to serve as tracer particles for the flow model. The technique employed allowed for control of particle size, buoyancy and color. The fabrication procedure is described below. Each batch of spheres produced approx. 800 microspheres of median size approx. 1.3mm, adequate for performing one stage of visualization.

1. Polymer solution: 4gr. Polymer mixture of poly(styrene) and poly(methyl methacrylate) at a mixture ratio of 7:3 respectively in 15cc Methylene Chloride. The ratio can be varied slightly in either direction to produce slightly heavier (less styrene) or lighter (more styrene) particles. The polymer was allowed to dissolve while stirring overnight.
2. Surfactant solution: 1% w/v poly(vinyl alcohol) in water. 300cc of this mixture is needed for one batch.
3. The surfactant solution was spun in a 500cc beaker using an overhead stirrer at a rate of approx. 300 rpm.
4. The polymer solution was loaded into a 1cc syringe and dropped at a rate that maintained individual drops into the spinning surfactant solution through a 26G needle. This was performed a total of 4 times.
5. The particles spun for 30 minutes and were then emptied into a second beaker spun with a stirrer bar overnight. Steps 4&5 were repeated until the entire 20cc of polymer mixture was consumed.

6. The particles are washed of the surfactant and placed in the perfusing mixture of water and glycerin. Over the first 24 hours the particles gradually become lighter, after this period they achieve steady state.

III.2 Filming/image acquisition:

1. Lighting: Optimal lighting was achieved using daylight while surrounding the model itself with a cotton cloak to create an indirect diffuse lighting effect.

2. Contrast: Maximal contrast between particles and background was achieved by placing dark colored cardboard beneath the bottom of the Plexiglas box.

3. Filming: Filming was performed using an off the shelf digital video camera, Sony TRV-9000, mounted above the flow model perpendicular to the plane of the bifurcation. The camera has an inherent rate of 30fps and resolution of 720X480. Shutter and exposure were set to automatic and the focus was allowed to set automatically and then frozen on manual to prevent fluctuations in focus.

4. Acquisition: Movie files were digitally acquired using a Sony PCG-XG9 Laptop with an i-link interface. The movies were then imported into Adobe Premiere and still frames exported for the relevant flow phases.

III.3 Image enhancement:

The goal of image enhancement was to produce maximal contrast between particles and background with minimal noise. This greatly improved the quality of the ultimate flow visualization both by streamline visualization and particle image velocimetry. Enhancement was performed using Adobe Photoshop as follows:

1. A mask image was prepared containing an outline of the channels of flow shaded in with one color and everything else shaded in with a different color (see fig. 2-17).

38
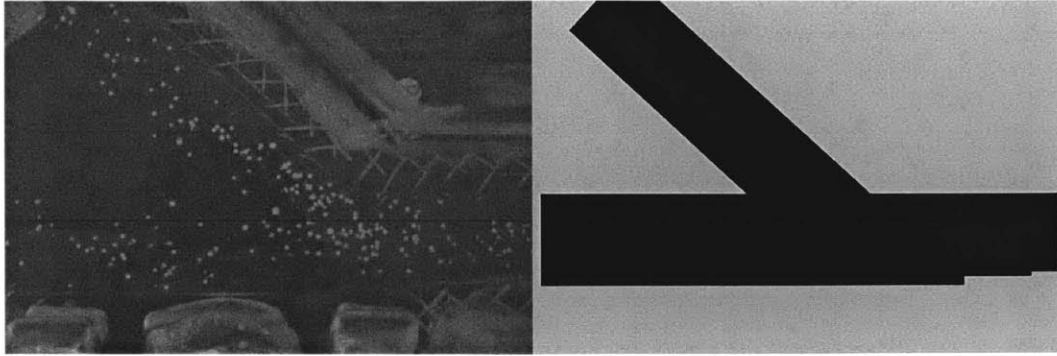
Figure 2-17: Mask image. Left panel – original image of model with tracer particles. Right Panel – Mask image.

2. The mask image was pasted onto the original image as a second layer.

3. The background shade (light part of top image on right) was selected using the magic wand tool.

4. The mask image layer was cleared.

5. The selected area (gray in top image) was filled using the bucket tool with black.

6. The image levels were adjusted using the autolevels command.

7. The Magic wand tool with a tolerance of 2 was used to select one of the particles in the image. The select similar command was used repeatedly to expand this selection to all of the particles. The command was repeated as many times as possible without including the background in the selection.

8. The selection was inverted and the background was filled with black using the bucket tool.

9. The image mode was converted to grayscale. Image levels were adjusted using the autolevels command.

10. The noise was reduced using the despeckle filter.
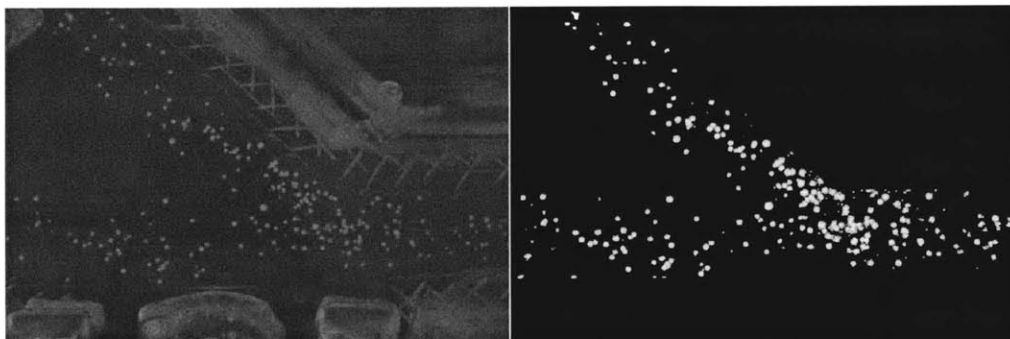
Figure 2-18: Image enhancement. Left panel – original image. Right panel – after image enhancement.

39

IV. Dimensionless analysis

Many engineering problems exist for which a rigorous analytical solution to the governing equations simply cannot be achieved. These problems are often examined with physical modeling; so it is with the scenarios investigated in this work. The building of physical models is complicated by many factors, several of which are discussed in this thesis, of which the issue of length scales is perhaps the most obvious. Models that test large structures like aircraft or ships are typically reduced in scale. On the other hand, models that test small prototypes, such as flow in the arterial tree, are typically enlarged in scale to make the measurements and observations easier to perform. Dimensionless analysis provides a mathematical framework that allows one to correctly interpret the results obtained in testing of a scaled model to the expected data in the prototype.

The basis for dimensional analysis is the concept of *dynamic similarity* and can in a simplified form be understood as a scaling factor for differences between the prototype and model systems. For any system, in our case a flow field, a set of dimensionless parameters can be defined, which describe the interaction and relative weight of forces acting on the flow. Each parameter is a function of the dimensions of the model (e.g. length, diameter, etc.), the properties of the fluid (e.g. viscosity, density, etc.), the properties of the flow field (e.g. velocity, frequency of pulsatility), the properties of the environment (e.g. temperature) and others. Maintaining dynamic similarity between a model and a prototype implies that all of these dimensionless parameters are kept at exactly the same values. For example, in order to maintain the well known Reynolds number constant, if the length of the model is scaled up by a factor ten but the viscosity remains the same, the velocity must be scaled down by a factor ten in order to maintain dynamic similarity. Under these conditions, the flow field can be expected to be geometrically similar i.e. have the same shape as the one in the prototype.

Theoretically, to achieve dynamic similarity *all* dimensionless parameters of fluid flow must be kept constant. These include the: Reynolds number, Strouhal number, Weber number, Womerseley number, Froude number, Cavitation number, Mach number, Prandtl number, Nusselt number, the steady and unsteady pressure coefficients as well as many others. In practice, as many of these parameters can be expressed as combinations of the others, maintaining some parameters constant ensures that others will remain

constant as well. Practical considerations and limitations however, typically limit the number of coefficients that can be kept constant in an experimental model. Since the number of properties that make up the dimensionless parameters is finite, often times in a scaled model maintaining one dimensionless parameter constant will actually directly contradict maintaining some other dimensionless number constant. This problem necessitates defining of the most relevant dimensionless parameters that affect the given problem of interest, rating these in order of importance and then maintaining as many of the important parameters as possible. As will be demonstrated in the course of this thesis, sometimes it is possible to use the form of the dimensionless parameter itself to deduce data for the prototype even if the parameter itself is not kept constant.

We proceed then to analyze the dimensionless parameters that are most relevant to the problem of the shape of the flow field within arteries:

The Reynolds number:

Definition: $\mathrm{Re} = \dfrac{\rho V L}{\mu}$

Where ρ is the density of the fluid, V is the characteristic velocity[i], L is the characteristic length of the system[ii], and μ is the dynamic viscosity of the fluid. This is often replaced by:

$$\mathrm{Re} = \frac{VL}{\upsilon}$$

Where υ is the kinematic viscosity of the fluid.

Significance: The Reynolds number gives the ratio of inertial forces to viscous forces acting on the flow. As such it is extremely important in determining the flow regime one is working in. At low Reynolds numbers, flow can be expected to be very sluggish, with little to no separation and take a long time/space to develop. Such is the case with honey where the viscosity of the solution is significantly higher than the product of the characteristic velocities and lengths. Swirling wind provides the opposite end of the spectrum, where with minimal viscosity high Reynolds numbers are achieved and flow can be expected to be inherently unstable, large areas of separation and eddies are evident

---

[i] In the case of flow through a closed channel such as the case of arteries this is typically taken as the mean velocity of flow in the channel.
[ii] In flow through a closed channel this is typically the diameter of the tube.

and develop relatively quickly. The Reynolds number also has an intimate link to the phenomenon of turbulent as opposed to laminar flow. Laminar flow is one in which individual fluid particles move in a smooth and predictable manner. Adjacent particles move in continuous sheets or *lamina* that are at every point parallel to each other. Turbulent flow on the other hand is one in which the motion of particles is no longer predictable except in a statistical sense. There is considerable mixing between adjacent layers of the flow to the point where layers cannot be defined. The transition from a laminar flow regime to a turbulent one was the topic of Lord Osborne Reynolds' original research. His data showed that at low Reynolds numbers, flow in a pipe remained laminar throughout. At a Reynolds number of approx. 2300 (known today as the "upper critical Reynolds number"), laminar flow would spontaneously undergo a transition into turbulence. On the other hand, below a Reynolds number of approx. 1800 (known today as the "lower critical Reynolds number"), turbulent flow would revert back to laminar.

This leads us to the critical question: what is the Reynolds number for flow within typical arteries? The answer to this question is unfortunately not a simple one. The reason for this stems from the fact that while the dimensions of arteries are easily obtained, as are the properties of blood (density and viscosity) – there is quite a large variation in the estimates for the velocity of blood flow. To understand why this uncertainty comes about, one must consider the way in which in-vivo flow velocities are obtained.

There are several ways in which to measure the flow. These include a number of extra-corporeal sensors and devices, as well as devices placed within the flow itself. The problem with all of these types of devices is that they either require the vessels to be isolated from their surrounding tissue (as is the case in extra-corporeal EM sensors for example) or that devices be placed in the flow which alter the flow itself. Thus, results obtained by these methods vary greatly depending on the effect they have on the flow itself.

Perhaps the only way to measure flow without disturbing it is by using what is known as a "flow wire", which is a thin (0.014") guidewire of the type used to direct the placement of endovascular devices such as balloon catheters mounted with a piezoelectric crystal. This device makes use of the Doppler effect to obtain the flow velocity in the vicinity of the crystal. The problem with this method stems from the fact

that the cross-sectional location of the wire in the artery is practically impossible to control and hence some velocity profile must be assumed to relate the velocity measured by the crystal to the mean velocity of the tube. Most of these devices assume a fully developed laminar profile in a tube, i.e. the Haggen-Poiseuille parabolic flow. In practice however, issues such as entrance length, bifurcations and a non-negligible Womerseley number (discussed hence) all work to make the flow non-parabolic hence invalidating this assumption.

These issues not withstanding, one must ultimately attempt to estimate the Reynolds number in arteries. Common ranges cited in the literature are:

Artery	Reynolds number range
Coronaries	$90^{1i} - 300^2$
Ascending Aorta	1100^3
Common Carotid	180^4
Renal	$300-500^5$

Table 2-1: Reynolds numbers. Common values cited in the literature.

Note that while there is a wide variation in these values, all the cited values are well below the lower critical Reynolds number, making the existence of turbulence improbable. Moreover, all the values belong to the same flow regime – one in which inertial forces are clearly dominant over viscous ones and yet are not high enough to provide for turbulence. In this sense it is really not the precise Reynolds number that must be kept constant but rather the order of magnitude of the Reynolds number as long as we are primarily concerned with the qualitative aspects of the flow field. This statement holds true for any one of the dimensionless parameters considered.

The Womerseley number:

Definition: $\alpha = \dfrac{L}{2}\sqrt{\dfrac{2\pi \rho f}{\mu}}$

---

[i] This is the only measurement made with flow wires.

Where L is a characteristic length of the system (most commonly diameter), ρ is the density of the fluid, μ is the viscosity of the fluid and f is the frequency of oscillations (heart rate).

Note: A common practice is to present α^2 often referred to as the "unsteadiness coefficient".

Significance: The Womerseley number gives the ratio of *transient* inertial forces to viscous forces and is thus sometimes referred to as a "Reynolds number based on frequency". It provides an estimate of the extent to which the flow profile is affected by the frequency in a pulsatile system. At low Womerseley numbers (usually corresponding to low frequencies), the flow is usually "quasi-steady" i.e. at every instant in time the properties of flow (for example the profile) are determined by the boundary conditions (e.g. pressure) as if the flow was steady with these boundary conditions held constant. At high Womerseley numbers on the other hand, the profile does not have time to develop and the instantaneous flow profile is typically blunted with respect to the parabolic one (see fig. 2-19). The entire core of fluid moves almost as a whole and the conditions known as "slug-flow" develop.
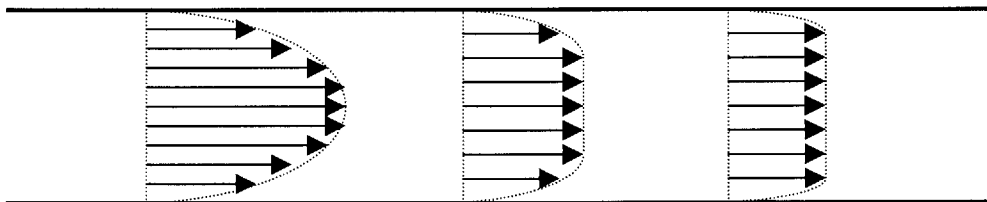
Figure 2-19: Instantaneous flow profiles for different Womerseley numbers. On the left is the case of low Womerseley number – profile is parabolic. Middle and right panels show intermediate and high Womerseley numbers respectively.

Once more we are left with the question: what are the relevant values in real arteries? The answer is once more non-conclusive reflecting the difficulty in obtaining in-vivo measurements. However, common estimates range between 5 and 15 depending on the artery in question. This places the in-vivo Womerseley number in the gray range of not really quasi-steady and not really slug-flow. Numerical and experimental measurements however have simulated this flow and the results in practice turn out to resemble the slug-flow situation much more closely than the instantaneously parabolic case[4,6].

Since this work is primarily focused on flow separation and hence the velocity profile of flow within arteries, these two dimensionless parameters were regarded as the most critical in importance. Thus an effort was made to keep these two parameters constant (or more precisely within the same regime) between prototype and experiment. Nonetheless, consideration must also be given to several other dimensionless parameters including:

The Strouhal number:

Definition: $S_t = \dfrac{fL}{U_m}$

Where f is the frequency of oscillations (heart rate), L is a characteristic length (diameter) and U_m is the maximal flow rate.

Significance: The Strouhal number governs such things as the rate of break away of unstable vortices. A common everyday example of this is the wind whistling as it passes over wire. In the case of the analysis here, it is of lesser importance.

Note also that:

$$\frac{\alpha^2}{Re} = S_t$$

So that keeping the Reynolds number and the Womerseley number the same will by definition also maintain the Strouhal number constant.

Mach number:

Definition: $Mach = \dfrac{U}{C}$

Where U is the velocity of flow and C is the speed of sound in the fluid of interest.

Significance: The Mach number is extremely important in regimes where it becomes close to 1 or where the fluid is highly compressible. In those cases, it governs the formation of shock waves through the flow. In our case however, the Mach number is extremely small and both blood and the simulating fluid are highly non-compressible so that the Mach number can be disregarded.

Steady and Unsteady pressure coefficients:

Definition: $C_{steady} = \dfrac{P_0}{\rho U_0^{\,2}}$ $C_{unsteady} = \dfrac{P_{unsteady}}{\rho U C}$

Where P_0 is the characteristic steady pressure (mean pressure), ρ is the density of the fluid, U is the flow velocity, $P_{unsteady}$ is the pulse pressure and C is the speed of sound in the fluid.

Significance: both these parameters can be neglected provided two conditions are met: First, as long as the pressure pulse wavelength is much longer than the characteristic length of the model, the velocity gradients induced by the pressure pulses are too small to cause observable effects. Second, care needs to be taken to make sure that the model length is not a multiple of ¼ of the wavelength thereby introducing resonance effects. As long as the wavelength is at least 4 times the characteristic length of the model, this is satisfied.

The speed of sound in the perfusing fluid is on the order of 1500m/sec. The fundamental frequency for the pump used in our model is approx. 0.1Hz. Hence the wavelength for this flow is approx. 20Km. thus for all significant harmonics of this pressure waveform the above two conditions are easily met.

V. Derivation of parameters for model circulation:

We begin by citing the relevant parameters for the prototype. Once more we note that there is considerable variation in the literature as to these values. We maintain however that since all these values are really within the same flow regime, and since the present work strives to present qualitative results and not precise numerical predictions, the use of one set of data is as good as another. In practice the data here is based on measurements obtained using flow wires in coronary arteries such as[7]:

Cross-sectional area:	$A = 7.64\text{mm}^2$
Diameter[i]:	$D = 3.12\text{mm}$
Mean velocity:	$U_{ave} = 15\text{cm/sec}$
Frequency (heart rate):	$f = 60/\text{min}$

---

[i] Derived from cross-sectional area assuming circular cross-section.

Viscosity of blood: $v = 0.05$ stokes

These values allow us to calculate the following values for the dimensionless parameters:

Reynolds number: $Re \approx 100$

Womerseley number: $\alpha \approx 1.5\text{-}2.0$

Were it not for practical physical constraints, we would like to create a model that would reproduce these precise parameters. However, one is rarely placed in such a scenario, and in the physical model, the following constraints exist:

To perform flow visualization effectively and to dynamically change the geometry of the model, as discussed in the materials and methods section, the diameter of the main branch of the model is constrained to be no smaller than approx. 2.5cm.

The stroke volume of the pump used to simulate the pulsatile waveform is limited to 100cc. In practice, as the frequency of the pump must be reduced greatly to match the Womerseley number, the stroke volume is limited to an even smaller value of approx. 60-70cc.

The frequency of the pump cannot be reduced below approx. 0.1Hz.

The viscosity of the fluid that can be pumped cannot greatly exceed that of the viscosity of blood.

Given these constraints, these are the values ultimately used in the modeling:

Diameter: $D` = 2.5$ cm

Stroke volume: $SV` = 65$ cc

Frequency: $f` = 1/9$ Hz.

Mean velocity[i] $U`_{ave} = 1.4$ cm/sec

Viscosity of fluid: $v` = 0.05$ stokes

These values give the following for the dimensionless parameters:

$Re` \approx 70 \approx 0.7 \cdot Re$

$\alpha` \approx 4.7 \approx 2.7 \cdot \alpha$

---

[i] Derived from $SV`$, $D`$ and $f`$.

47

As can be seen, the values for both the Reynolds and the Womerseley numbers are not identical to the prototype, and yet are sufficiently close to produce reliable qualitative results.

VI. References:

1. Di Mario C, Meneveau N, Gil R, de Jaegere P, de Feyter PJ, Slager CJ, Roelandt JR, Serruys PW. Maximal blood flow velocity in severe coronary stenoses measured with a Doppler guidewire. Limitations for the application of the continuity equation in the assessment of stenosis severity. *American Journal of Cardiology*. 1993;71:54D-61D.
2. He X, Ku DN. Pulsatile Flow in the Human Left Coronary Artery Bifurcation: Average Conditions. *Journal of Biomechanical Engineering*. 1996;118:74-82.
3. Rieu R, Friggi A, Pelissier R. Velocity Distribution Along an Elastic Model of Human Arterial Tree. *Journal of Biomechanics*. 1985;18:703-715.
4. Rindt CCM, Steenhoven AA. Unsteady Flow in a Rigid 3-D Model of the Carotid Artery Bifurcation. *Journal of Biomechanical Engineering*. 1996;118:90-96.
5. Sabbah HN, Hawkins ET, Stein PD. Flow Separation in the Renal Arteries. *Arteriosclerosis*. 1984;4:28-33.
6. Fung YC. The Frequency Parameter of Pulsatile Flow. In: *Biodynamics. Circulation*. New York: Springer-Verlang; 1984:100-104.
7. Di Mario C, Kern MJ, Serruys PW. Intracoronary Doppler: Instrumentation and Principles of Analysis and Interpretation. In: Topol EJ, ed. *Textbook of Interventional Cardiology*. 2 ed. Philadelphia: W.B. Saunders; 1994.

Chapter 3: Experiment

This chapter describes the 4 main experiments performed in this work:

I.   Establishment of flow regime.

II.   Mathematical modeling.

III.   Flow visualization.

IV.   Sedimentation analysis.

Each segment dealing with an experiment is subdivided into three parts:

1. Theory. This part describes the main theoretical concepts behind the method of the experiment and the hypothesized results.

2. Experiment. A description of the methods used in the experiment and the measurements performed.

3. Results and Discussion. The raw data obtained from the measurements performed in part 2 and a discussion of its possible meaning.

<u>Flow circuit data:</u>

Experiments I, II: Stroke volume   = 80mL

                      Pump frequency   = 0.10Hz.

                      Bifurcation model:

                            Angle of bifurcation   = 45°

                            Mother/Daughter diameter ratio = 4:3

Experiments III, IV: Stroke volume   = 65mL

                      Pump frequency   = 0.11Hz.

                      Bifurcation model:

                            Angle of bifurcation   = 45°

                            Mother/Daughter diameter ratio = 1:1

I. Experiment 1 - Establishment of flow regime

I.1 Theory:

The measurable physical parameters in the flow, pressure and flow rate, are related to each other by the fluid dynamic impedance of the vessel segment. The generalized Ohm's law describes this relation:

$$\Delta P(t) = Z(\omega) \cdot Q(t)$$

Where $\Delta P(t)$ is the instantaneous pressure drop in the vessel, Z is the frequency-dependent fluid dynamic impedance of the vessel and $Q(t)$ is the instantaneous rate of flow in the vessel.

The impedance of the vessel segment is comprised of three independent components: resistance, compliance and inertance. The geometry as well as the conditions of flow determines the relative importance of these three factors.

Resistance: The simplest flow scenario is that of steady flow in a straight long tube of constant cross section with rigid walls. For this flow, the resistance is given by the Haggen-Poiseuille equation:

$$\nabla P = \frac{128\mu}{\pi D^4} \cdot Q$$

Where ∇P is the pressure gradient, μ is the fluid viscosity, Q is the flow rate and D is the tube diameter.

The fluid dynamic resistance is defined in analogy with electrical resistance:

$$R \equiv \frac{\nabla P}{Q}$$

and hence is given by:

$$R = \frac{128\mu}{\pi D^4}$$

Since R is not frequency dependent, it's contribution to the total impedance is simply:

$$Z_R = R$$

Compliance: The elasticity of the blood vessel wall imposes a compliance component of the fluid dynamic impedance. In the same way that the fluid dynamic resistance is analogous to electrical resistance, the compliance is analogous to electrical capacitance. It is defined by:

$$-Q = C \frac{\partial(\nabla P)}{\partial t}$$

Its contribution to the total impedance is given by:

$$Z_C(\omega) = \frac{C}{\omega}$$

Where C is the compliance, which is a constant determined by the geometry and the material properties of the vessel, and ω is the frequency of oscillations of flow.

As is reflected in the equation above, the contribution of compliance to the total impedance is inversely related to the frequency. At high frequencies, the vessel wall does not have sufficient time to expand and contract and hence the effect of compliance is negligible. At low frequencies on the other hand, the vessel expands considerably during each cycle and the compliance has a major effect on the flow.

Inertance: A third contribution to overall impedance is imposed by the inertia of the fluid. The electrical analogy here is with inductance. The inertance is defined by:

$$-\nabla P = I \frac{\partial Q}{\partial t}$$

such that its contribution to the total impedance is given by:

$$Z_I(\omega) = \omega I$$

Where I is the inertance, which is a constant determined by the geometry and the material properties of the fluid, and ω is the frequency of oscillations of flow.

In contrast to compliance the inertance contribution to the total impedance is proportional to the frequency. At very low frequencies, flow is for the most part unidirectional and so inertia plays very little role. At high frequencies, fluid is constantly being accelerated and decelerated and thus inertia plays a major role in determining the pressure required to move fluid.

In the most general case, the impedance and hence the relation between the pressure drop in the vessel and the flow rate is determined by a combination of all three components. However, under certain conditions the fundamental frequency of the oscillations dictates that either the compliance or the inertance is negligible, greatly simplifying analysis of the model. In the case of blood flow in the arterial bed, the compliance is very small and can be neglected leaving just the inertance and resistance as the major components of impedance.

I.2 Experiment:

The assertion that this is an inertia-dominated system was validated by the following method: The pressure drop waveform in the main vessel was recorded using pressure taps feeding into a differential pressure sensor. The proximal tap was located immediately upstream from the model (see fig. 3-1), and the distal tap was located immediately downstream from the model on the mother vessel. Flow rate in the mother vessel was recorded using the flow sensor mounted on the tubing carrying the mother vessel flow.
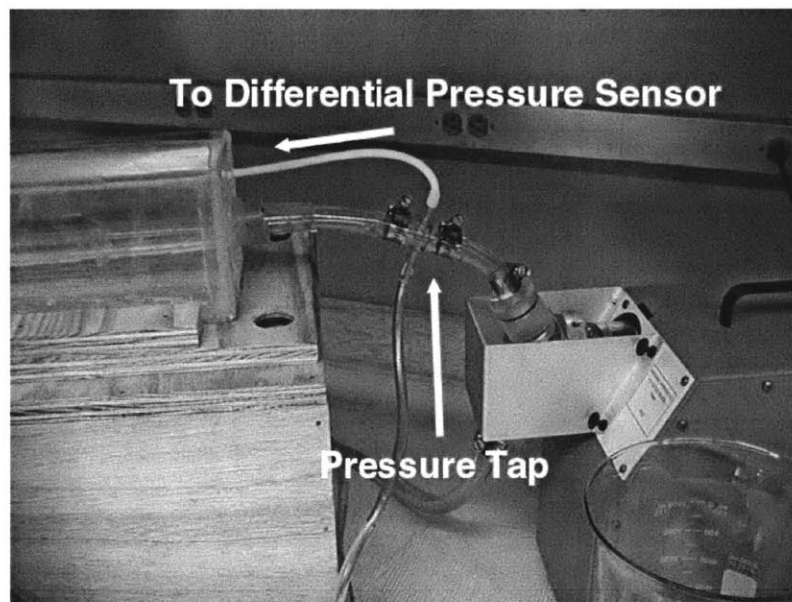
Figure 3-1: Proximal pressure tap for differential pressure measurement. A similar tap is located downstream from the model on the mother vessel.

Both the differential pressure and the flow-rate waveforms were decomposed into their Fourier spectrum. For each integer multiple of the fundamental frequency the Fourier coefficient for the differential pressure drop was divided by the Fourier coefficient for the flow rate. This produces a plot of the impedance as a function of frequency. In the compliance-dominated regime, the magnitude of the impedance should drop with increasing frequency. In the inertance-dominated regime, the magnitude of the impedance should be expected to increase with frequency.

I.3 Results and Discussion:

The plot for the magnitude of the Fourier transform of the differential pressure waveform and the flow waveform is given below (fig. 3.2), as well as the magnitude of the impedance as a function of frequency.
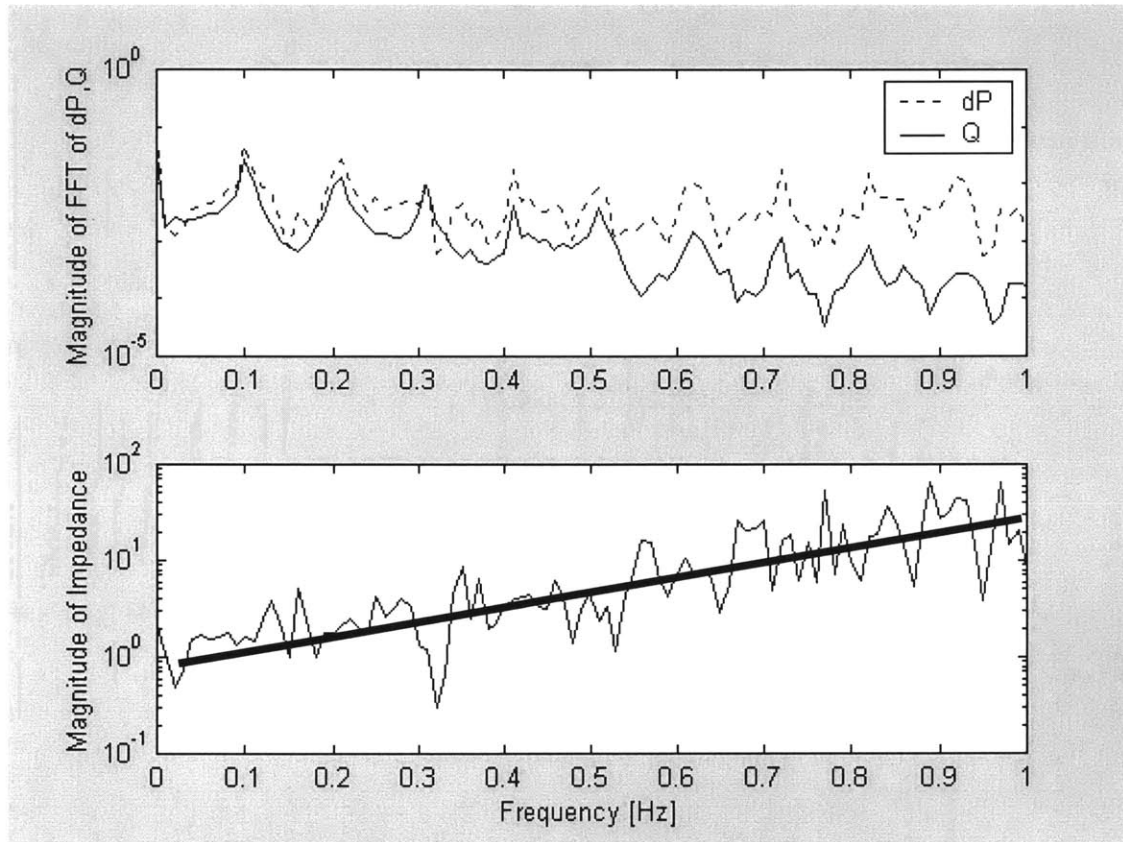
Figure 3-2: Fourier transform of waveforms and impedance. Top panel – magnitude of FFT of differential pressure and flow waveforms. Note the harmonics at integer multiples of fundamental frequency of 0.1 Hz. Bottom panel – magnitude of the fluid dynamic impedance, in arbitrary units, as a function of frequency. Note the clear increase in values with increasing frequency.

The top panel of figure 3-2 clearly shows the expected form of the Fourier transform of both the flow rate and the differential pressure waveform. Harmonics can be seen at integer multiples of the fundamental frequency of the pump which is approx. 0.1Hz.

In the bottom panel, when one transform was divided by the other, these harmonics can no longer be distinguished. Inspection of the bottom panel (note the logarithmic scale) shows that the impedance clearly increases with frequency. As discussed in the theory section (I.1), this increase indicates that the system is inertial as

55

opposed to capacitance-dominated. In some respects, the frequency dependence observed here contradicts the traditional first order model of the vascular system, the Windkessel model, which only includes resistance and capacitance elements. The apparent disparity between the two models is most plausibly explained by the inclusion of the entire vasculature from the aorta onwards in the Windkessel model. The aorta is the primary site of vascular compliance, and would naturally require a capacitor rather than an inductor. The present model on the other hand deals with a more isolated portion of the circulation, namely that of a group of distributing arteries such as the coronary arteries. These arteries are less compliant than the aorta, and as the volume they contain is much smaller their potential capacitance should be much less significant than that predicted by the Windkessel model. This result is consistent with the observation[1] that a non-compliant model was no worse at correlating between intimal thickness and measured wall shear than a compliant model.

Finally, the observed frequency dependence justifies the use in the next experiment of a mathematical model that includes resistance and inertance, but not compliance. A system function H(S) for such an inertial-resistive model can then be written with two terms:

$$H(S) \equiv \frac{Q(S)}{\Delta P(S)} = \frac{1}{R + I \cdot S} \quad \text{or:}$$

$$\Delta P = (R + I \cdot S) \cdot Q$$

The first term is a resistance and is independent of S, frequency, reflecting the proportional relationship between pressure drop and flow rate. The second term includes a frequency component and reflects the fact that in a purely inertial system, the pressure drop is proportional to the time derivative of the flow rate as indicated by:

$$-\nabla P = I \frac{\partial Q}{\partial t}$$

Had the system had a significant compliance-related impedance, there would have been a need to incorporate one more term into the system function, inversely related to frequency (1/S).

II. Experiment 2 – Mathematical modeling

II.1 Theory:

Mathematical models can aid in the qualitative understanding and help construct quantitative descriptions of the physiological flow system. This requires proper validation, precise quantification and repeatable measurements. In the most basic mathematical model of a linear physical system the system is defined by its response to a controlled stimulus. The output is measured and the form and nature of the transformation of the input that creates the output is defined as the *system transfer function*. Once the system transfer function is identified, the output waveform for an arbitrary input can be deduced. We can view the flow system as an input-output system if we define the differential pressure across the vessel segment as the input and the flow through the segment as the output or vice-versa. The system transfer function is then simply the LaPlace transform of the differential equation that governs the flow circuit. In the general case this circuit can be quite complex, however since we have shown in the previous section that this is an inertia-dominated system, we can neglect the compliance and model it at the lowest order as simply a resistance with an inertance in series, much like an electrical circuit of a resistor with an inductor in series. The differential equation governing this circuit is then:

$$\Delta P(t) = R \cdot Q(t) - I \cdot \frac{dQ(t)}{dt}$$

Taking the LaPlace transform of this equation we obtain:

$$\Delta P(S) = R \cdot Q(S) + I \cdot S \cdot Q(S)$$

And thus the system function is given by:

$$H(S) \equiv \frac{Q(S)}{\Delta P(S)} = \frac{1}{R + I \cdot S}$$

This function allows us, given a flow waveform to compute the predicted pressure waveform that would be produced. Alternatively, since the properties of the system - resistance and inertance - appear in the system function as free parameters, given a known flow and pressure waveform we can use the system function to find a fit for the resistance and inertance values.

Despite the obvious analogy between an electrical and a fluid dynamic resistance, there is an important difference: An electrical resistor has a set value, independent of the circuit it is placed in or the current flowing through it. In contrast, the fluid dynamic resistance through a *fixed* geometry is dependent on the flow through it. For example, flow separation can raise the resistance in a segment by altering the effective diameter for flow (see fig. 3-3).

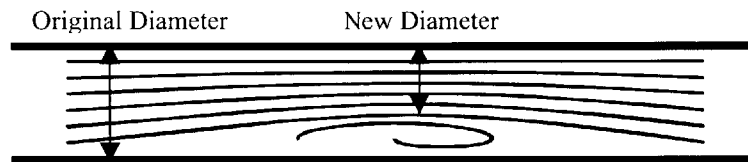Original Diameter   New Diameter

Figure 3-3: Effective diameter in a tube with separated flow.

The boundary conditions imposed by the flow act in exactly the same way as a physical wall with the effect of reducing the diameter and thus raising the resistance.

The value for the inertance is determined primarily by the physical properties of the fluid, and the setting of a pump that propels fluid through the system, both of which remain constant despite changes in the flow field. Very large changes in the flow field, such as might occur if the flow were diverting in a completely different direction, would be expected to change the inertance. However, the macroscopic direction of flow is assumed constant throughout these experiments. Hence we can assume that the inertance remains constant despite changes in regions of flow separation in the branches of the bifurcation.

II.2 Experiment:

II.2.a. Part a - Validation

To validate the mathematical model, the physical flow model was perfused and the differential pressure and flow rate were measured and subsequently low-pass filtered to reduce noise with a cutoff frequency of 2Hz to include the first 20 harmonics. The waveforms were then used in conjunction with the difference equation that represents the system function in discrete domain to obtain a fit for the two free parameters R and I. This was accomplished by simulating the differential pressure waveform based on the flow waveform, and minimizing the total difference between the simulated and measured waveforms by varying the free parameters in a stepwise fashion using the Matlab

command `fmins` which employs the Nelder-Mead simplex method. Once the best fit for R and I were obtained, these values were used to predict the differential pressure waveform from the flow waveform (see appendix B). The predicted waveform was visually compared to the measured waveform. A good agreement between the two was taken as a validation of the mathematical model.

II.2.b. Part b - Quantification of flow separation

Once the mathematical model was validated it could then be used to provide a quantitative measure of the region of flow separation in the mother branch. Flow and differential pressure waveforms were acquired for different conditions simulating scenarios of progression of disease, adaptive optimization of the flow system (e.g. collateral flow), and/or mechanical intervention on the lesion. The different cases are described in the following table:

Case	Daughter Vessel Constriction	Mother Vessel Geometry	Collateral Flow
1	None	Straight	None
2	None	Taper	None
3	Partial	Taper	None
4	Full	Taper	None
5	Full	Straight	None
6	Full	Straight	Full
7	Full	Bow out	Full
8	None	Bow out	Full
9	None	Straight	Full

Table 3-1: Experimental cases for quantification of flow separation. Cases 1-9 represent disease and intervention scenario.

For each flow condition, Fourier decomposition was performed for both the differential-pressure and flow-rate waveforms. The Fourier coefficients for the former were divided by the coefficients for the latter to provide impedance as a function of frequency. Based on the assumption that the contributions to this impedance come from resistance, which is invariant with frequency, and inertance, the resistance was taken as the impedance at zero frequency. As outlined in the theory section above, changes in the resistance are taken to be a reflection of changes in the extent of flow separation.

59

II.3 Results and Discussion:

II.3.a. Part a - Validation
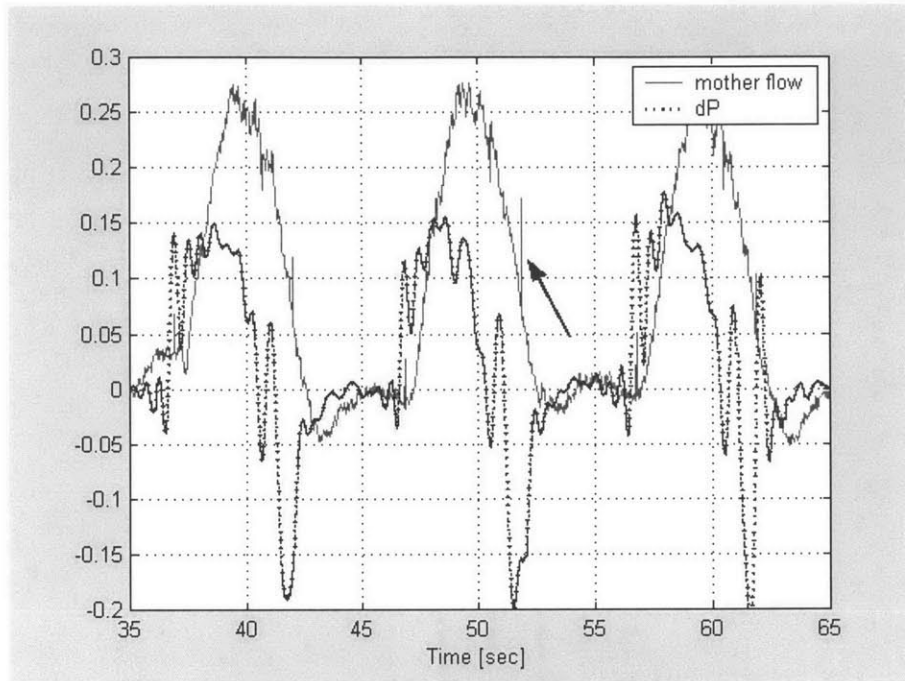

Figure 3-4: Waveform acquisition. Unfiltered mother flow waveform and filtered differential pressure waveform. Note appearance of dicrotic notch indicated by arrow and corresponding up-down-up deflection in dP waveform.
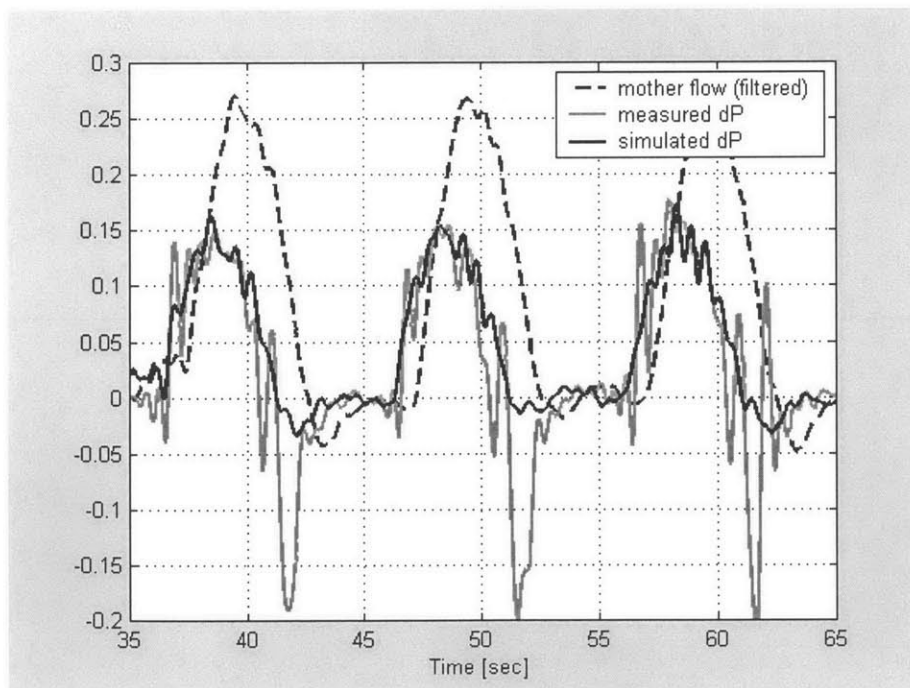

Figure 3-5: Waveform simulation. Note disappearance of dicrotic notch after filtering, and the correlation of the simulated and measured waveform elsewhere.

As can be seen in figure 3-5, there is excellent agreement between the measured differential pressure drop and that predicted by the mathematical model based on the flow-rate waveform. This includes correlation, in phase and in magnitude, of local minima and maxima in both waveforms. The one place where this fit is inadequate is in mid-deceleration where the measured waveform has a characteristic up-down-up deflection that the predicted waveform does not follow. This error likely arises from the origin of the deflection. As can be seen in figure 3-4, the deflection in the pressure waveform corresponds in phase to the location of the dicrotic notch in the flow-rate waveform. Furthermore, the shape of the deflection in the pressure waveform is the theoretical response one would expect to the dicrotic notch. The response to any waveform is determined by the system function, which in this case is comprised of a linear combination of a multiplication by constant and a derivative with respect to time. The dicrotic notch is essentially an impulse function. The derivative of an impulse function consists of a sharp positive deflection, followed by a sharp negative deflection and a return to zero. The presence of just such a function in the differential pressure waveform (figure 3-4), further reinforces the assertion that the deflection in the differential pressure waveform is a result of the presence of the dicrotic notch. However, prior to performing the mathematical simulation that generated the predicted differential-pressure waveform, the flow-rate waveform was low-pass filtered to produce better behavior of the numerical filtering algorithm that is the system function. This low-pass filter removed all high-frequency components from the measured flow waveform signal, including the dicrotic notch itself that is naturally comprised entirely of high frequency components. Thus, when the system function is imposed on the flow waveform to produce the predicted differential-pressure waveform, this flow waveform no longer includes a dicrotic notch. Accordingly, the predicted differential pressure waveform is missing the response to the dicrotic notch, which accounts for the discrepancy seen in figure 3-5.

II.3.b. <u>Part b - Quantification of separation</u>

Disease and intervention scenario: The resistance values for the mother vessel in each one of the cases described in table 3-1 are given below:

Case	1	2	3	4	5	6	7	8	9
Mother	Straight	Taper	Taper	Taper	Straight	Straight	Bow	Bow	Straight
Daughter	-	-	±	+	+	+	+	-	-
Collateral	0	0	0	0	0	+	+	+	+
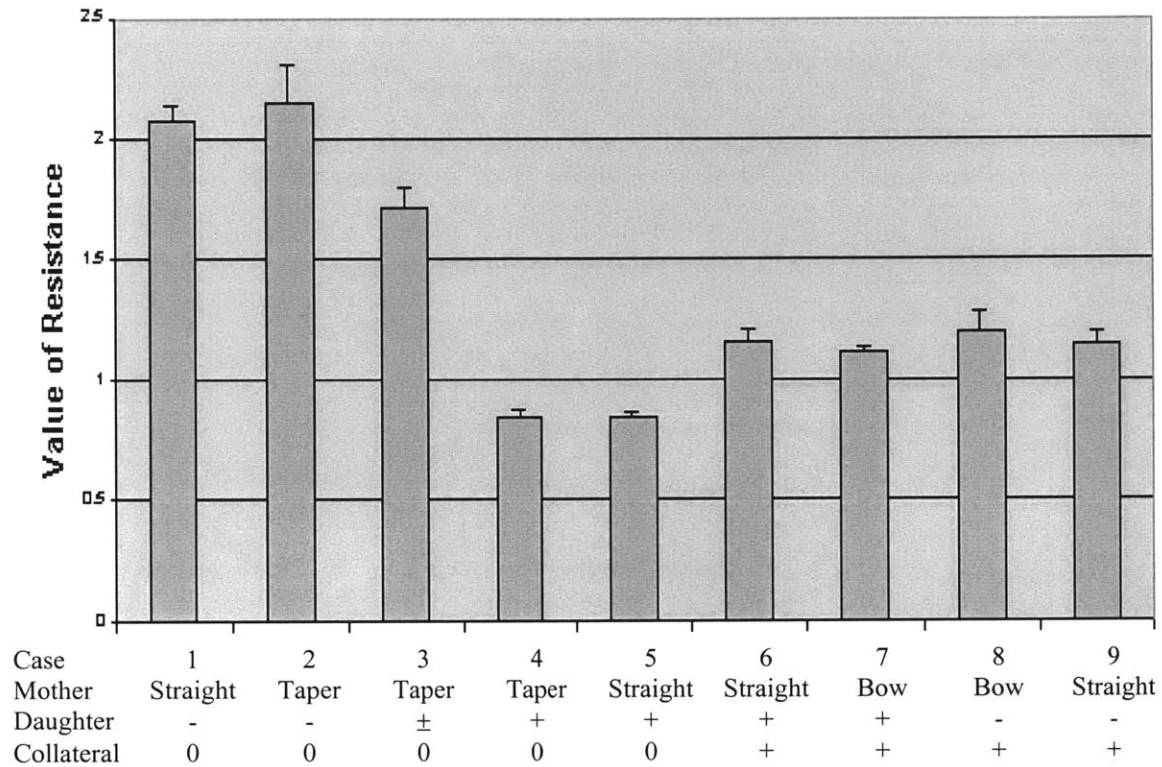
Figure 3-6: Quantification of resistance. Value of resistance in mother vessel, in arbitrary units, for cases 1-9 as calculated by best fit.

Figure 3-6 shows the resistances computed for the 9 flow model configurations described in table 3-1. Since these values are given in arbitrary units, only the relative change between the cases carries physical significance.

As expected, there is virtually no change in the resistance from case 1 to case 2, despite the reduction in the diameter of the mother vessel between these two cases. The lack of effect on resistance is consistent with the theoretical prediction that a part of the cross-section of the main vessel in case 1 was taken up by a region of flow separation. Thus, while the physical diameter of the vessel was reduced in case 2 when a taper was induced on the mother vessel, the effective diameter for flow did not change, keeping the resistance nearly constant.

As progressive constriction was imposed on the daughter vessel in cases 3 and 4, a marked reduction in the resistance of the main branch was observed, despite no change in the geometry of the main branch. Once more, this is consistent with the theoretical model that attributes a part of the resistance in the main branch to flow separation induced by the presence of the side branch. As flow into the side branch was reduced, the region of flow separation in the main branch decreased and the resistance dropped.

Case 5 differed from case 4 in that the gradual taper in the main branch opposite the ostium of the side branch was now removed. At this point, flow was essentially through one straight channel. On theoretical grounds, the resistance would be expected to decrease further, and yet this was not the case. The resistance in case 5 was almost identical to case 4 (fig. 3-6). A possible explanation for the lack of resistance alteration lies in the method in which the differential pressure measurement was performed. A rough estimate of the expected effect of removing the taper can be achieved using the Haggen-Poiseuille equation. When the flow rate in this equation was set to the mean flow rate of the pump, the calculated pressure drop over 4 diameter lengths for a straight segment would only be 0.01 mmHg lower than that of a vessel with a 10% taper. In contrast, the differential pressure sensor measured a total pressure drop across the entire model on the order of 1 mmHg. Hence, the pressure drop from the taper was only a small component of the total pressure drop measured. The small pressure drop creates two problems: a low signal to noise ratio, and more importantly, the presence of the major part of the pressure drop elsewhere in the model. A likely site for this pressure drop is in the connectors that interface the pressure tap into the flow circuit, as well as the interface of the glass pieces that connect the external tubing to the silicone channels. The pressure drop at these sites is most likely affected by any change in the flow patterns thus masking the effect in the region of interest.

Case 6 introduced collateral flow for the first time. Despite the fact that the geometry in the main branch in case 6 matched that of case 5, there was a clear increase in the resistance. A possible explanation for this observation is the reduced flow in the main branch that leads to reduced inertia, and thus a greater diversion of the streamlines in the main branch and a larger region of flow separation. However, the most likely

explanation still lies in the pressure drops outside of the region of interest, which cannot be separated from those that occur inside the flow channel.

When the mother vessel was bowed outward resistance should drop slightly from the increase in vessel diameter (case 7). Resistance increased with the elimination of the daughter vessel constriction (case 8) from the in re-introduction of flow separation in the mother branch established with the increase in daughter vessel flow. This relationship between mother vessel resistance and daughter vessel constriction was seen for all geometries in this work. Mother vessel resistance decreased with the introduction of a daughter vessel constriction whether the mother vessel was straight, bowed or tapered and in the presence or absence of collateral flow.

Case 9 demonstrates the fascinating observation that mother vessel resistance is determined not by absolute diameter, but rather by what is apparently the effective diameter mediated by the region of flow separation opposite the ostium of the side branch. It is important to note that the reduction of the diameter of the main branch under certain conditions can lower the resistance as opposed to raising it as would be expected in a simple one-vessel model.

III. Experiment 3 – Flow visualization

III.1 <u>Theory:</u>

Visualization of flow involves description of the shape and attributes of the flow velocity field. Many methods exist for this purpose including the simple injection of dye into the flow stream, creation of small hydrogen bubbles, introduction of smoke, tracer particles or other types of streamers etc. Other more elaborate methods include laser Doppler anemometry (LDA), which utilizes coherence of laser beams to measure precise instantaneous velocities at a point, as well as particle image velocimetry (PIV), which automatically tracks the flow to produce a vector field.

The specific properties of the models used in this experiment which determine the type of flow visualization were:

a) Pulsatile flow. Hence dyes and other types of streamers are ineffective as these fill up the entire cross-section when the flow is at its stationary point in the cycle.

b) Material properties. The materials and methods by which the flow model was built are not well suited for analysis using laser beams that require optical purity.

c) Scale. The scale of the model was such that small tracer particles could not be used without zooming in to a level that did not allow viewing of the entire region of interest in one frame.

d) The scale and material required precise diffuse lighting and so methods that rely on high definition optics (most PIV) were not well suited for this model.

Given these considerations, two methods for flow visualization of the models were adapted specifically for use here. These two methods give complementary views of the flow field that can be used simultaneously to get an overall qualitative description of the properties of flow:

III.1.A. <u>Method A: Visualization of streamlines</u>

Visualization of streamlines involves using the tracer particles described previously to obtain a semi-instantaneous image of the streamlines of flow. This was done in the following way:

The model was perfused and filmed using the digital video camera at 30 frames per second. Neutrally buoyant tracer particles were injected into the flow via the proximal injection port. The particles were not suspended in the perfusing fluid itself so as to maintain a high particle concentration inside the model itself. A digital video image was acquired, stored on the computer and synchronized to the waveform analysis. A 64-frame, approx. 2 seconds or ¼ of a cycle, segment of the video for which visualization was to be performed was identified using the waveform analysis. The segment was split into 64 still-frame images. The images were enhanced to produce maximal contrast between particles and background, and each of 32 pairs of successive images used to produce a difference image using the image→calculations→difference command in Adobe Photoshop. This was repeated for these 32 difference images in a binary tree fashion. The outline of the bifurcation was drawn onto the image using one of the original 64 images to detect the edges.

This method produces an image that is composed of each one of the original particles at 64 successive positions and thus represents the paths these particles take. If the particle density is high enough, and the image is limited to a short period in time compared with the length of an entire cycle[i], then these lines represent the instantaneous streamlines at the point in the cycle that they were taken. Furthermore, since the length of each line represents the velocity of the particle that produced it, this method actually provides a hybrid representation comprised of not only information about the direction but also the magnitude of the velocity vector field.

III.1.B. <u>Method B: Particle image velocimetry</u>

Our particle image velocimetry was adapted from an algorithm developed by Douglas P. Hart at the department of mechanical engineering at MIT. This program is described in a paper by D.P. Hart[2] and is available for download from his website at: http://web.mit.edu/dphart/www/Program.pdf. Like all PIV algorithms, this program employs a correlation between the particle locations in two images to deduce the vector field that produced the translocation of these particles. The algorithm also employs

---

[i] In practice, the first and last 32 successive images were used to make two images each of which span approx. 1 second, an order of magnitude shorter than a cycle.

bilinear interpolation to fill in the spaces between tracked particles with appropriate velocity vectors. The primary limitation to using this program to obtain vector images in the present models is that the program's effectiveness is highly dependent on the particle concentration. To achieve a high particle concentration in the present models, particles on the order of tens of microns in diameter need to be used. While these particles can easily be fabricated, capturing a clear image of them with the video camera requires either a very high-resolution camera, or elaborate lighting. To escape these problems, large particles on the order of hundreds of microns to a millimeter were used. This however dictates that the number of particles that can be injected at a time and hence the number of particles per image field is low, producing poor results with the PIV algorithm.

To overcome this problem the following method was employed to raise the apparent particle density in the image field. As in the first method the model was perfused and filmed using the digital video camera at 30 frames per second. Tracer particles were injected into the flow via the proximal injection port. The digital video image was acquired, stored on the computer and synchronized to the waveform analysis. A phase in the flow waveform was chosen to perform the visualization. This typically was the point of maximal velocity, mid-acceleration, mid-deceleration, etc. Two cycles (not necessarily successive) that had a relatively high particle density were selected. For each cycle, six successive still images at the selected phase were produced and enhanced to provide maximal contrast. For the purpose of this procedure we labeled these images 0 thru 5. Using Adobe Photoshop, image 4 was copied and pasted onto image 0. Using the magic wand tool, the background on the image 4 layer was selected and then cleared. The same procedure was followed for images 1 and 5. Thus, we were left with two "successive images" that contained twice the normal particle density each, although the second layer of particles was close to the first layer of particles thus in reality the particles in each image were effectively doubled. This procedure was repeated for the second cycle.

The first and second of the successive images for each cycle were combined using the same technique to ultimately produce two composite images one frame apart which had four times the density of particles as the original images. The entire procedure is illustrated in fig. 3-7.
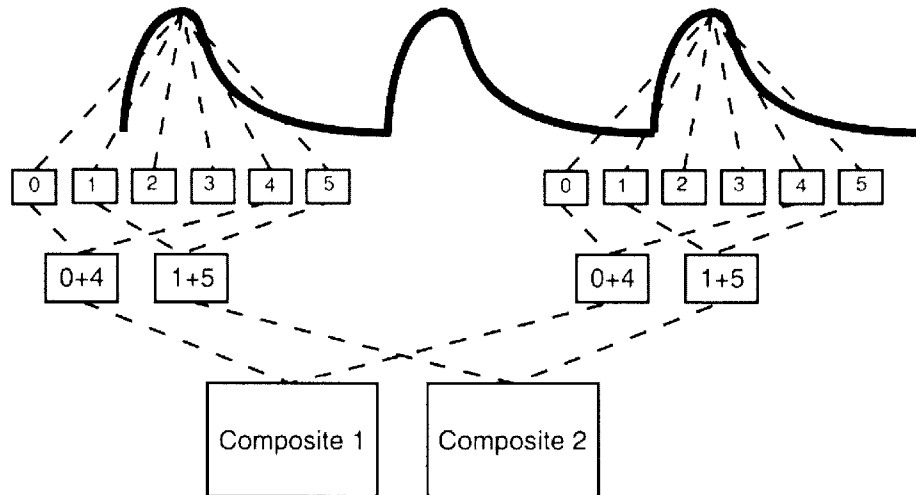

Figure 3-7: Scheme for creating composite images for PIV. Frames 0 thru 5 in each cycle are successive. Composites contain four times the particle density of original frames.

Once the two composite images were obtained, the normal particle image velocimetry program was run using the following parameters:

Primary Correlation Window Size   = 32

Sub-Correlation Window Size   = 32

Compression Pixel Number   = 32

Maximum Search Length   = 8

Max. Dev.   = 8

√ Fill Voids   √ Smooth Data   √ SPCorrection

The output was then displayed at a velocity scale of 8[i]. The output image was copied and pasted into Adobe Photoshop where it was cropped and enlarged to the original 720X480 resolution of the DV camera. An image of the boundaries of the bifurcation, obtained using the original frames, was superimposed onto the image. Vectors occasionally fell

---

[i] For an explanation of the meaning of each one of these parameters, see the help file in the software package.

outside of the boundaries because of the interpolation scheme and were deleted from the final vector field map.

III.2 Experiment:

III.2.a. Part a – Experimental scenario

The experimental scenario was simulated in several cases, distinct from those described previously (table 3.1), where each case represented a change in one geometric parameter of the model. These cases are outlined in the table 3-2 below. Lesions in the daughter vessel were simulated by reduction of flow using the downstream resistance.

Case	Mother vessel geometry	Daughter vessel flow[+]	Collateral flow[+]
10	Constant diameter	93%	None
11	Gradual taper	95%	None
12	Gradual taper	61%	None
13	Slightly tapered	17%	None
14	Slightly tapered	8%	25%
15	Constant diameter	93%	36%
16	Medium Lesion	No lesion	None
17	Large Lesion	No lesion	None

[+] Percent of mother vessel flow.

Table 3-2: Cases for scenario simulation.

Note: Daughter vessel flow in case 14 was affected by both the lesion and the re-distribution of flow from the introduction of collateral and hence does not reflect the extent of the lesion alone. The extent of the lesion on the side branch was similar to that of case 13.

69

The two methods for flow visualization detailed above were performed for each case. PIV was performed at the phase in the cycle that corresponded to immediately before maximal flow velocity was attained. Streamline visualization was performed at approx. 2/3 of the maximal velocity both during the acceleration and the deceleration phases. The results were then compared on a case-by-case basis.

III.2.b. Part b – Temporal development of flow separation

The model was fixed in the geometry described by case 10 in table 3-2 above, i.e. a straight mother vessel, no lesion in the daughter vessel and no collateral flow. PIV was performed at the beginning of the deceleration phase of flow, and one second later during mid-deceleration. The two results were compared to see how the flow field develops over time during the deceleration phase.

III.3 Results and Discussion:

III.3.a. Part a – Experimental scenario

For each one of the cases outlined above (table 3-2) a figure is provided showing the following four results:

1. A sample of the waveform representing one cycle. Circles denote the instants of the flow visualization. A dashed circle denotes the PIV, a single circle denotes streamlines at acceleration and a double circle denotes streamlines at deceleration.
2. PIV result.
3. Streamlines at acceleration.
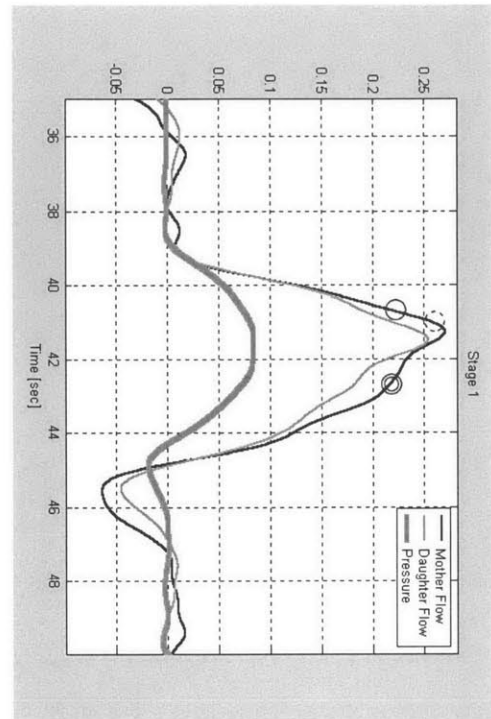4. Streamlines at deceleration.

The caption for each one of these figures identifies the three components that define the specific case of the experiment: mother vessel geometry (straight, tapered or lesion), daughter vessel flow (see table 3-2) and collateral flow (see table 3-2). The parameter that has been altered from the previous case in the figure in question is underlined. Following each one of these data sets is a discussion of the important aspects of flow that can be identified in the figures, and a comparison is made with the previous sets.
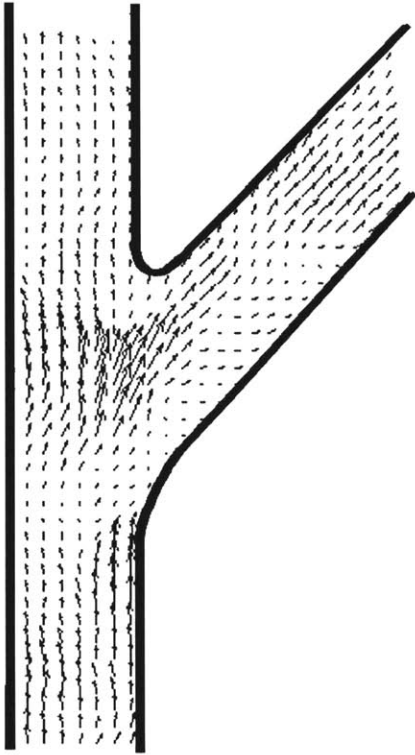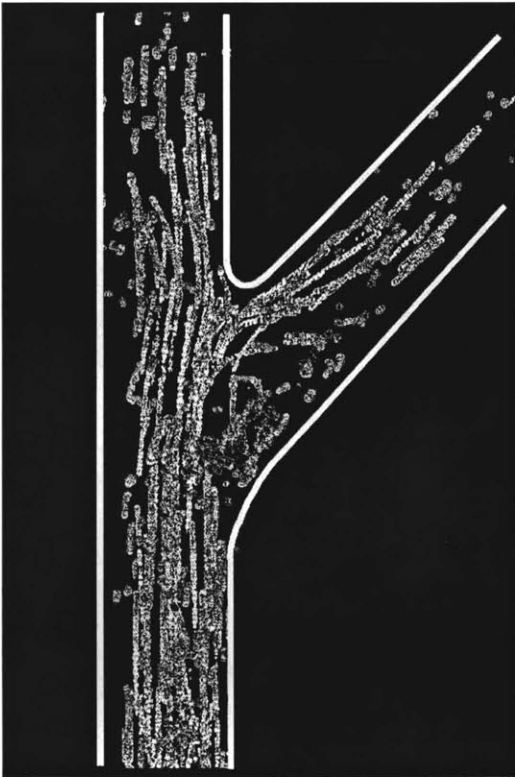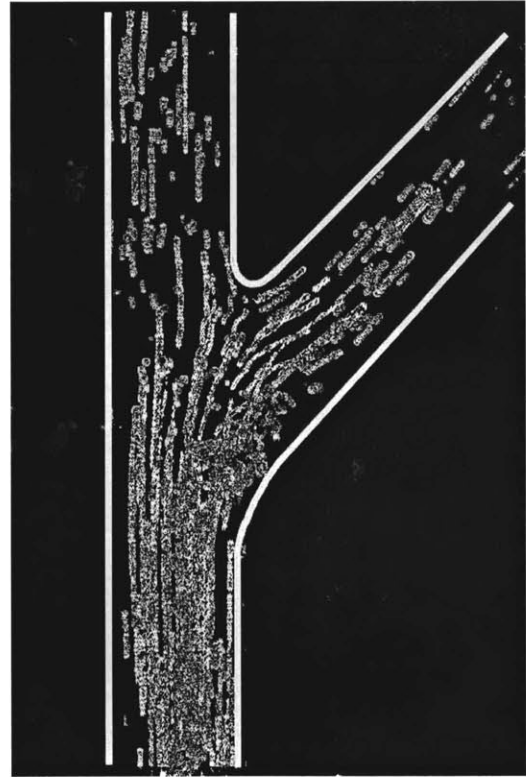
Figure 3-8: Case 10 visualization. Mother vessel: Straight, Daughter flow: 93%, Collateral flow: 0. (A) Waveform: Dashed circle: PIV, Single circle: Streamlines at acceleration, Double circle: Streamlines at deceleration. (B) PIV. (C) Streamlines at acceleration. (D) Streamlines at deceleration.

The waveform plot (fig. 3-8A) shows the general characteristics typical of flow rate through most arteries. There is a sharp period of acceleration, followed by a small decrease in velocity, a plateau phase and a deceleration down to zero velocity, followed by a period of low to zero flow of length approximately equal to that of the flow cycle. Note the appearance of flow reversal as indicated by a negative velocity in both the mother and the daughter branches. This flow reversal correlates with a period of what appears to be negative pressure. This negative pressure is not an actual vacuum, as liquids are incapable of sustaining a true vacuum, but rather a drop in the pressure to below the hydrostatic pressure at the flow sensor location that is used to determine the zero pressure point.

Particle image velocimetry (fig. 3-8B) clearly shows both regions of flow separation. The first prominent region is located in the ostium of the daughter branch on the lateral (proximal) wall. Vectors in this region are very short indicating low flow velocities and low shear stress. The vectors immediately adjacent to the wall are in fact reversed, indicating the re-circulation of fluid that occurs in the region of flow separation. The second region of separation can be seen in the main branch on the lateral wall opposite from the ostium of the side branch. The presence of separated flow is clearly indicated by the curvature of the direction of flow indicated by the vectors – first away and then back towards the artery wall. Flow in the central region of the bifurcation leading towards the flow divider can be seen to accelerate. This will eventually become the region of high shear predicted to occur adjacent to the flow divider walls. In this image, this high shear can be seen next to the daughter vessel angle of the flow divider. The mother vessel angle of the flow divider does not exhibit particularly high shear in this image, most likely from practical limitations of the modeling, namely absence of particles in that specific area in the images used to produce the PIV.

Streamline images (fig. 3-8C, 3-8D) show the same general phenomenon observed in the PIV image. Both regions of flow separation can clearly be made out by the curvature of the streamlines and the presence of very short streamlines inside, which indicate low flow velocities and low shear stress near the wall. The region of separation in the daughter vessel is more rounded and localized whereas the separation in the mother vessel is flatter and more elongated. This might explain why in the PIV image no flow

reversal can be detected adjacent to the wall in the mother vessel. As opposed to the PIV, the high shear region adjacent to both angles of the flow divider can now clearly be seen, especially in the deceleration picture, as indicated by very long streamlines corresponding to high velocities that nearly hug the flow divider walls.

Comparison between the acceleration (fig. 3-8C) and deceleration (fig. 3-8D) images provides further insight into the patterns of flow and separation. First, despite the fact that the mean velocities are the same in both cases, the regions of flow separation are entirely different in shape. In general, both regions of separation are substantially more pronounced in the deceleration phase than in the acceleration phase. Thus during deceleration, there is a shift of flow away from the lateral walls and towards the flow divider. This shift is also evident if one observes the difference in length of streamlines next to the flow divider between these two phases of flow. Secondly, while both regions of separation increase in size from acceleration to deceleration, this is much more pronounced in the daughter vessel than in the mother vessel. Thus, one would expect the relative resistances of these two vessels to change as the flow bypasses the stagnant zone. This can be observed in the flow waveform (fig. 3-8A) as the fact that despite the equivalence of flow rates in the mother vessels (as indicated by the two solid circles), the flow rate in the daughter vessel was lower during deceleration than during acceleration. This reduction can be explained entirely by the shift in relative resistances as growth of the regions of separation diverts flow from the daughter vessel towards the mother vessel during the deceleration phase of flow.

Lastly, combining all three flow images produced another interesting result. As indicated by the circles denoting the timing in fig. 3-8A, the chronological order of these three figures is 3-8C→3-8B→3-8D. Focusing on the location of the region of separation in the main branch, in particular the proximal end (the point of stagnation), one can see that the region grows in the proximal direction during the entire cycle.

The general features described in the discussion of this first case are evident in the results for all other cases defined in table 3-2. In what follows, the results for these other cases are presented in the same format and the discussion will focus on the changes that took place from one case to the other.
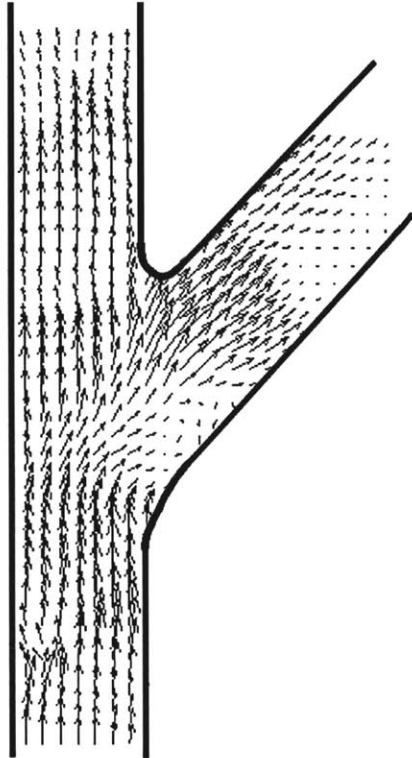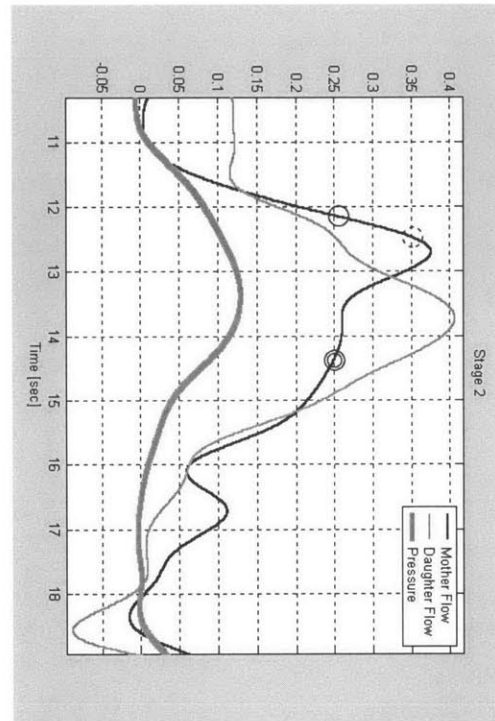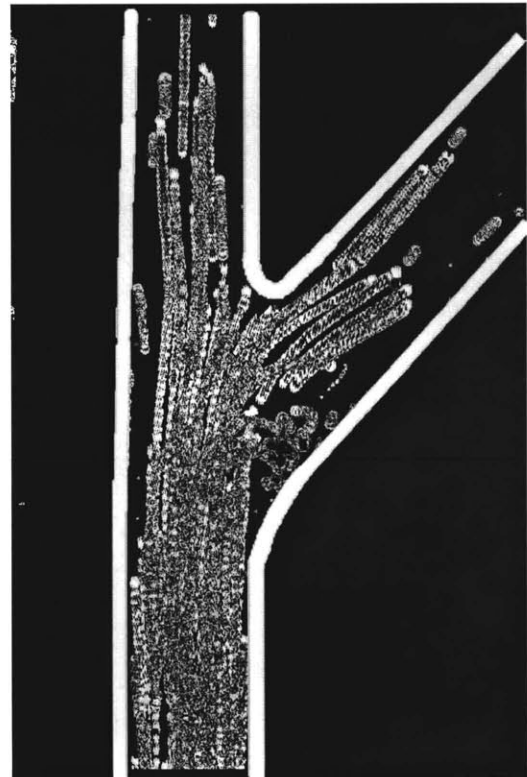
Figure 3-9: Case 11 visualization. <u>Mother vessel: Taper</u>, Daughter flow: 95%, Collateral flow: 0. (A) Waveform: Dashed circle: PIV, Single circle: Streamlines at acceleration, Double circle: Streamlines at deceleration. (B) PIV. (C) Streamlines at acceleration. (D) Streamlines at deceleration.

The gradual taper of the mother vessel produced a waveform plot (fig. 3-9A) of the same general characteristics as for a straight vessel (fig. 3-8A) with two qualitative differences worth consideration. First, the taper produced a phase shift between the flow rates in the mother and daughter vessels, with the daughter lagging the mother vessel waveform by approx. 20% of the cycle length. This phase shift can be considered much like the observed clinical phenomenon of delayed dye clearance in angiographic images of obstructed arteries. Second, taper eliminated the component of flow reversal in the mother vessel seen in the straight vessel waveform (fig. 3-8A) and the corresponding phase of negative pressure. PIV (fig. 3-9B) clearly supports the theoretical prediction for flow in this tapered geometry: While separation in the side branch is clearly evident, including a prominent aspect of reversal, there is no separation in the main branch. Instead, the vectors are parallel to the wall along the entire length of the tapering vessel. As before, very high shear can be seen to exist adjacent to the flow divider, particularly in the daughter branch angle. The streamline images (fig. 3-9C, fig. 3-9D) confirm the same observations seen in the PIV. The separation on the lateral angle of the daughter branch is obvious in the acceleration phase. There appears to be a slight residual separation in the mother branch in fig. 3-9C, however comparison of the length of streamlines adjacent to the walls between this image and fig. 3-8C clearly shows that there is significantly higher shear in the tapered vessel than in the non-tapered one. Finally, the deceleration streamline image (fig. 3-9D) provides further evidence of the phase shift between mother and daughter vessel flows noted above. While flow in the main branch is clearly decelerating at this point, most of the flow now seems to be entering into the side branch. This could be no more than a result of inaccuracies in the imaging, e.g. poor distribution of tracer particles in the image. However, coupled with the result seen in the waveform image (fig. 3-9A), it is likely that this effect is real.

Figure 3-10: Case 12 visualization. Mother vessel: Taper, <u>Daughter flow: 61%</u>, Collateral flow: 0. (A) Waveform: Dashed circle: PIV, Single circle: Streamlines at acceleration, Double circle: Streamlines at deceleration. (B) PIV. (C) Streamlines at acceleration. (D) Streamlines at deceleration.
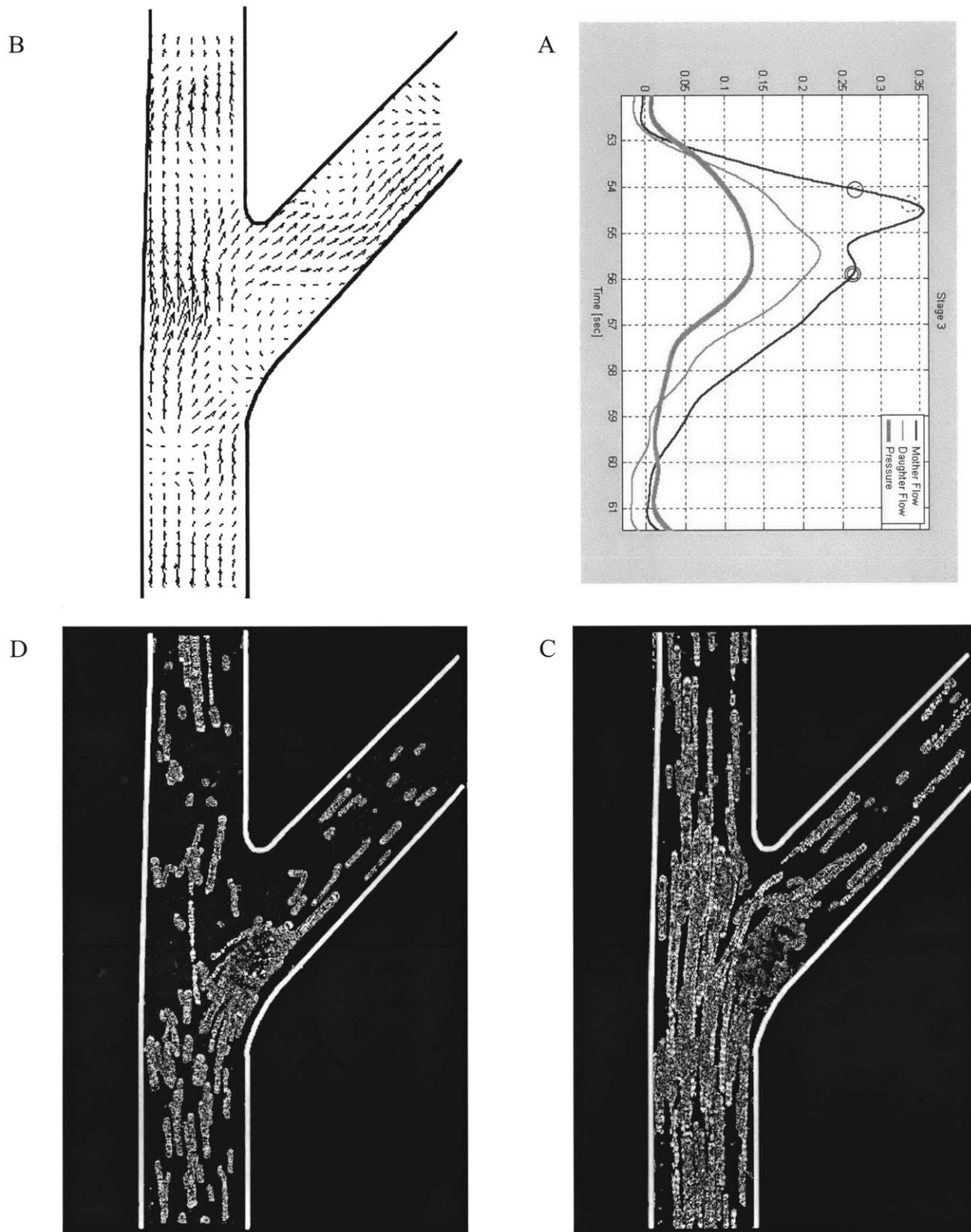
Figure 3-11: Case 13 visualization. Mother vessel: Taper, <u>Daughter flow: 17%</u>, Collateral flow: 0. (A) Waveform: Dashed circle: PIV, Single circle: Streamlines at acceleration, Double circle: Streamlines at deceleration. (B) PIV. (C) Streamlines at acceleration. (D) Streamlines at deceleration.
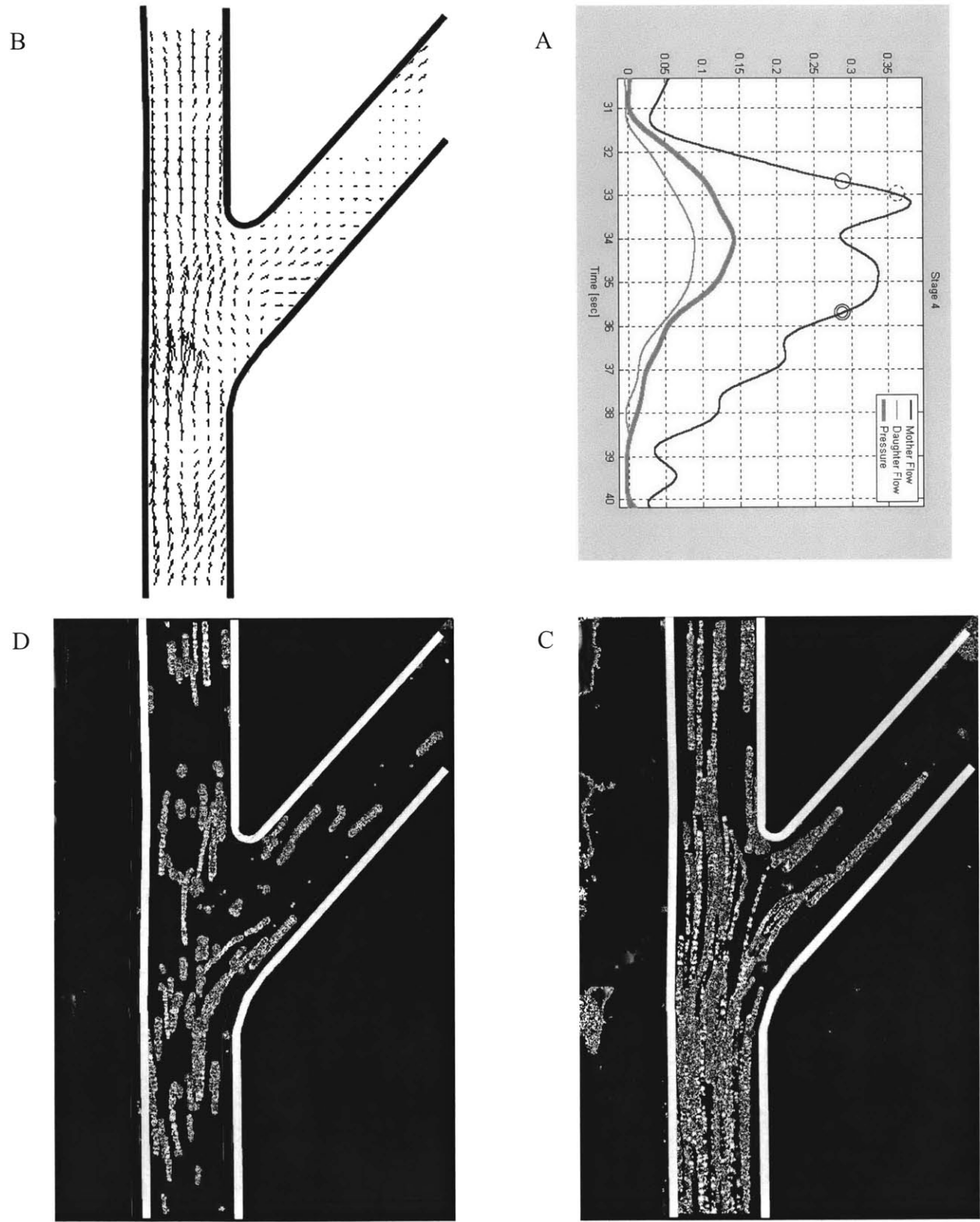
Case 12 represents a modest reduction in total flow into the side branch (61% of main branch flow), and case 13 represents a drastic reduction in total flow into the side branch (17% of main branch flow). Qualitatively, these are two points along a spectrum and thus they will be discussed jointly here. The waveforms (figs. 3-10A, 3-11A) once more show no evidence of flow reversal or negative pressures. Additionally, there is a change in the plateau phase of the mother branch flow rate waveforms. As the flow in the daughter branch was reduced, first modestly in case 12 and then drastically in case 13, the plateau pressure increased until it became a discrete peak (fig. 3-11A). The origin of this new peak can be attributed to the phase lag that was demonstrated between the mother and daughter flow waveforms (see fig. 3-9A and subsequent discussion of case 11). Since the pump output was held constant throughout all cases of this experiment, as the flow rate in the daughter branch was decreased, (figs. 3-10A and 3-11A) the excess flow, in the absence of collaterals, was added to the mother flow waveform. Since this excess is at a phase lag with the original mother vessel flow, the effect of this added flow was to create a second peak that increased in amplitude as more and more flow was diverted from the daughter vessel. Not unexpectedly, PIV (figs. 3-10B, 3-11B) showed progressively decreasing velocities into the daughter vessel as the total flow in the daughter vessel was reduced (compare vector lengths in the ostium from fig 3-9B to 3-10B and then 3-11B). While there is still some deviation of the vector alignments in the main branch (fig. 3-10B) accounted for by the non-zero flow into the side branch, for the most part and especially in fig. 3-11B, flow in the main branch is nearly axial laminar flow as would be expected in a simple straight tube. Streamline images once more show the reduced flow velocities into the daughter branch (compare length of lines in figs. 3-10C and 3-11C to fig. 3-9C). Additionally, the region of flow separation in the daughter branch in these two cases is reduced in size. This is likely from the slower flow rates, and hence, inertia of the fluid coming around the lateral angle and into the daughter branch. Separation in the mother branch was nearly eliminated in the modest flow reduction case (fig. 3-10C) and disappeared entirely in the drastic flow reduction as evidenced by the streamlines in fig. 3-11C that have no curvature towards the lateral wall at all.
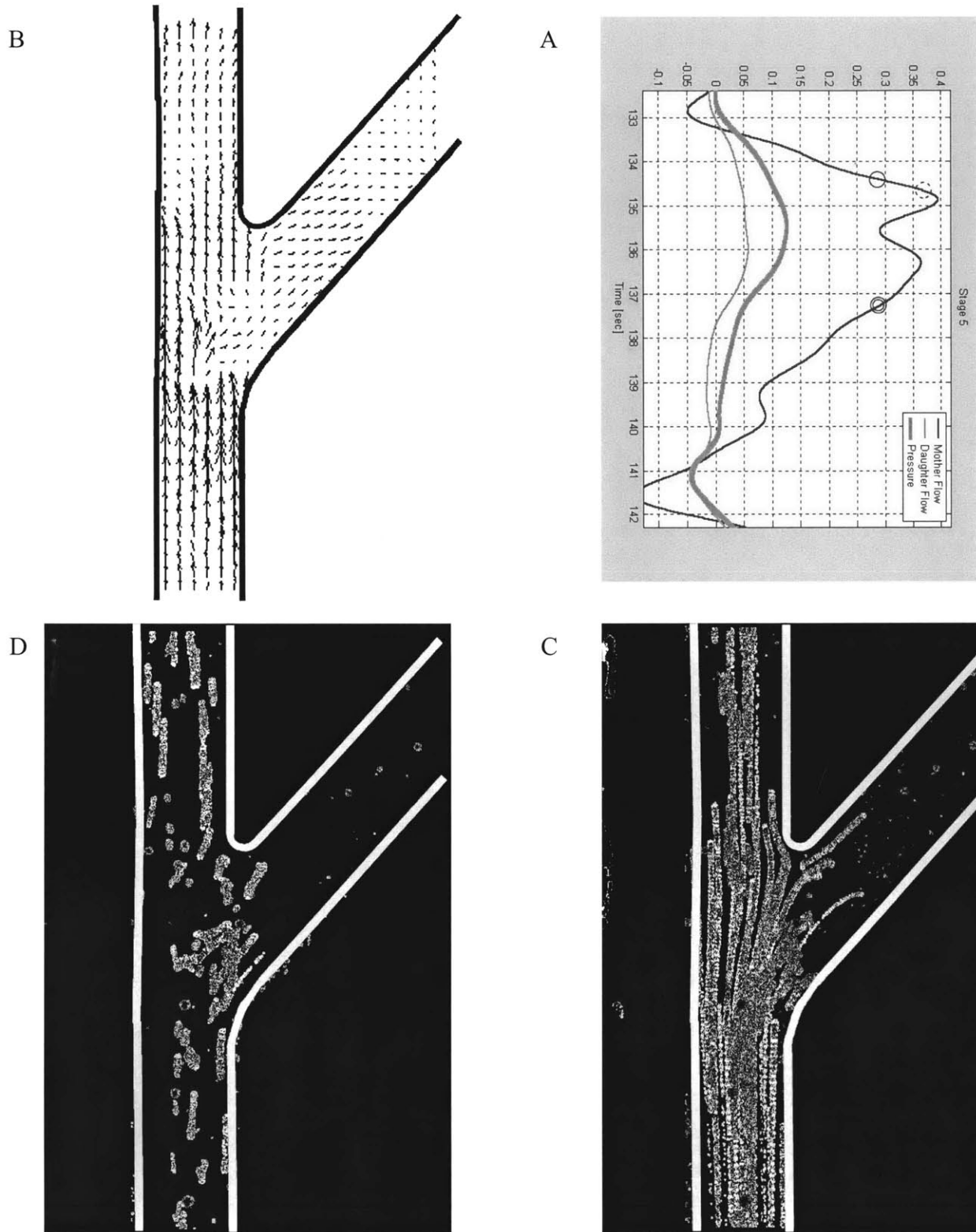
Figure 3-12: Case 14 visualization. Mother vessel: Taper, Daughter flow: 8%, <u>Collateral flow: 25%</u>. (A) Waveform: Dashed circle: PIV, Single circle: Streamlines at acceleration, Double circle: Streamlines at deceleration. (B) PIV. (C) Streamlines at acceleration. (D) Streamlines at deceleration.

The introduction of collateral flow in this geometry had very little effect on the shape of the flow patterns, as can be seen by comparison of the PIV images (figs. 3-11B, 3-12B) and of the streamline images (figs. 3-11C, 3-11D, 3-12C, 3-12D), despite the nearly 25% of the total pump output that was flowing through the collateral vessel. The length of the streamlines in figs. 3-12C, 3-12D is shorter than that of 3-11C, 3-11D in accordance with the reduced total flow entering this segment, yet the qualitative shape of flow remains unchanged. This observation is in fact meaningful, in that it shows that the qualitative shape of the streamlines through the bifurcation segment is relatively invariant with respect to the total flow coming into the proximal end. Hence, as long as one is interested in the qualitative aspects of flow and not precise absolute values, the experiment is not sensitive to a precise determination of the input flow, which is difficult to attain in the prototype because of the practical limitations discussed in chapter 1.

Inspection of the waveform (fig. 3-12A) and comparison with the previous case (fig. 3-11A) shows that a reduction in flow occurs in both the daughter branch and the mother branch. In other words, the collateral vessel "steals" flow from both vessels. The amount of steal can be predicted from the simple electrical analogy presented in fig. 3-13:
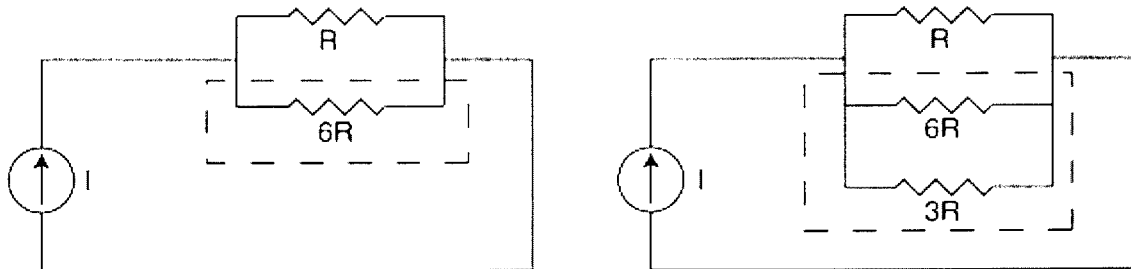
Figure 3-13: Collateral steal. Left panel shows circuit analogy prior to development of collateral. High resistance represents lesion in the daughter branch. Right panel shows analogy for development of collateral vessel. The regions in the organ perfused by the dashed boxes are the same.

The prediction gained from this model was compared to the integrated flow in the two vessels. These two values were consistently within 2% of each other, demonstrating that, for the purposes of this analysis, the simple electrical analogy is highly accurate. The reason this simple analogy works so well in this case is that as mentioned before with respect to the streamline images, the flow patterns themselves do not change with the introduction of collateral flow, hence the channels can be treated as simple invariant resistors.
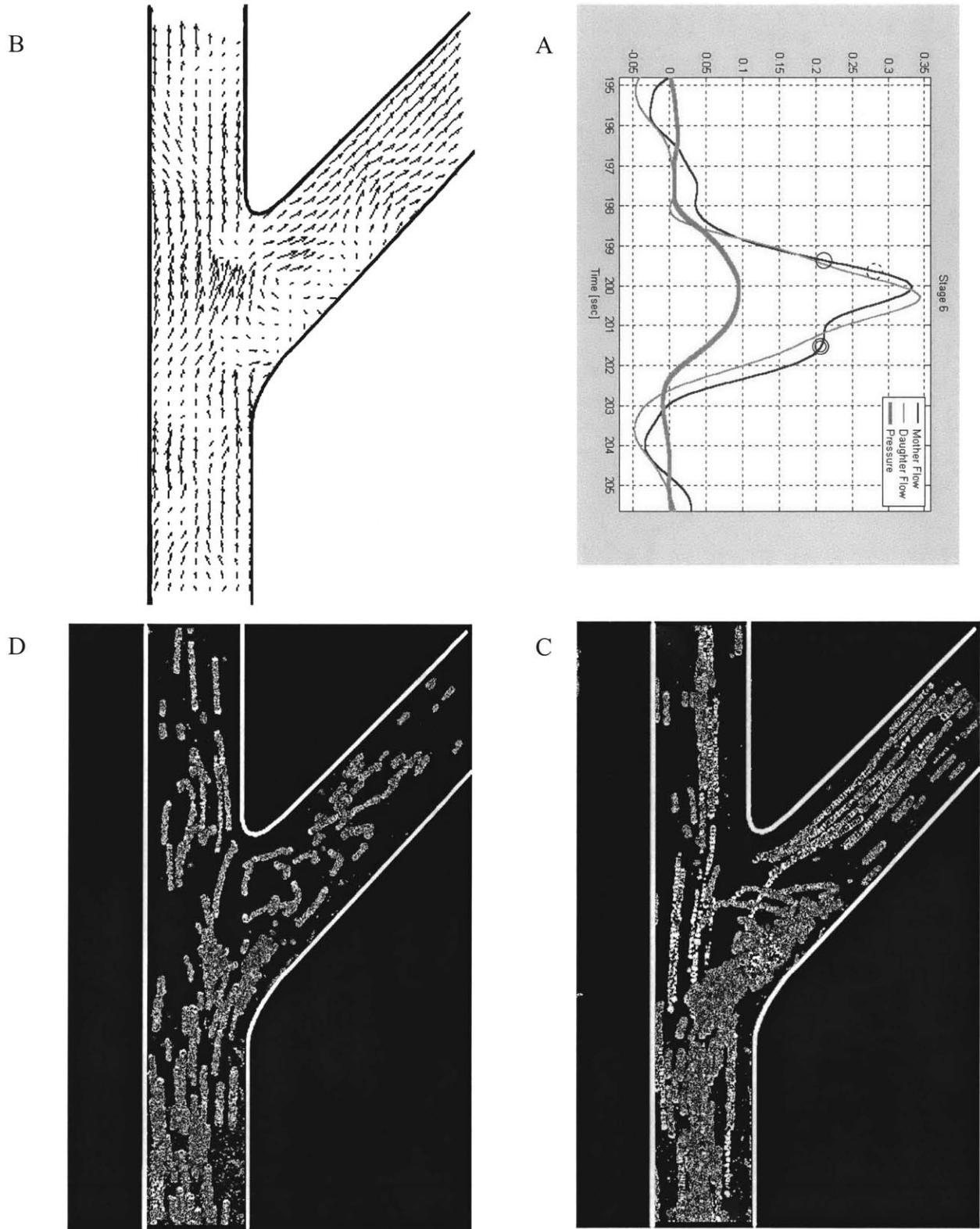
Figure 3-14: Case 15 visualization. Mother vessel: Straight, <u>Daughter flow: 93%</u>, Collateral flow: 36%. (A) Waveform: Dashed circle: PIV, Single circle: Streamlines at acceleration, Double circle: Streamlines at deceleration. (B) PIV. (C) Streamlines at acceleration. (D) Streamlines at deceleration.

Reopening of the daughter vessel in case 15 created a geometry that was similar in many respects to the constant diameter mother vessel with a patent daughter vessel (case 10), except for the existence of a substantial element of collateral flow. Examination of the waveform image (fig. 3-14A) shows the same general properties as those observed originally in fig. 3-8A. These include a plateau in the deceleration phase of the flow wave, as opposed to a discrete second peak, as well as flow reversal at the end of deceleration in both the mother and the daughter branches. Also present is the negative component in the pressure waveform, although it is somewhat smaller in fig. 3-14A than in fig. 3-8A. It is unclear whether this reduction in the negative component is from a real effect caused by the presence of collateral flow, or to intrinsic fluctuations that exist in all of the experimental waveforms. The PIV image (fig. 3-14B) shows the expected flow separation in the daughter branch, and re-establishment of a large region of flow separation in the mother branch. The extent of this latter region of separation is substantially larger both in the axial and in the radial directions than that seen in the straight vessel with intact daughter flow (compare with case 10 fig. 3-8B). The differences can only be attributed to the presence of collateral flow, the single geometric parameter altered between these two cases, and can be understood if one takes into account the reduced inertia of the flow in the main branch, from take-off of flow into the collateral. Such a reduction would allow easier and more extensive diversion of the streamlines from the axial direction. Streamline images provide further evidence of the above-mentioned growth in separation from case 10. The point of stagnation, the proximal end of the region of flow separation, can be seen to be further proximal in fig. 3-14C than in fig. 3-8C, extending now even more proximally than the ostium itself. Comparison between the deceleration phases (figs. 3-14D, 3-8D) shows the growth in the radial direction of the region of separation, which now extends to well beyond the centerline of the mother vessel.
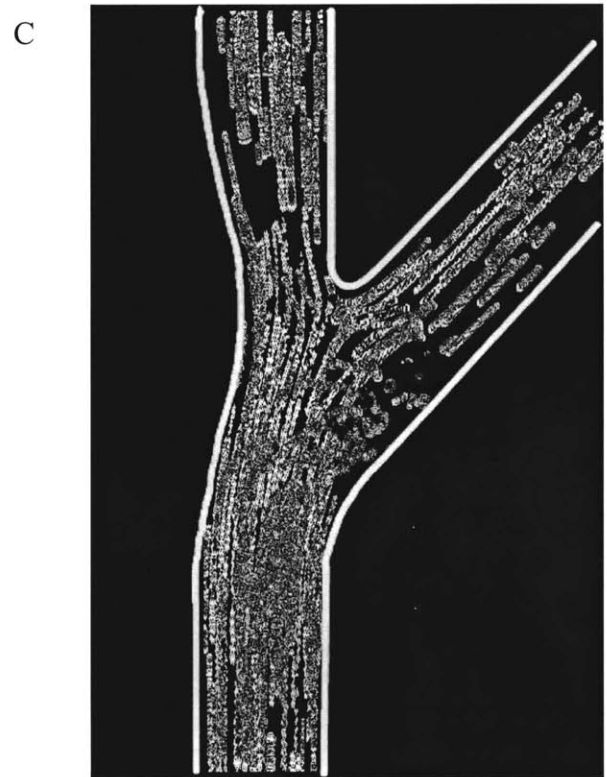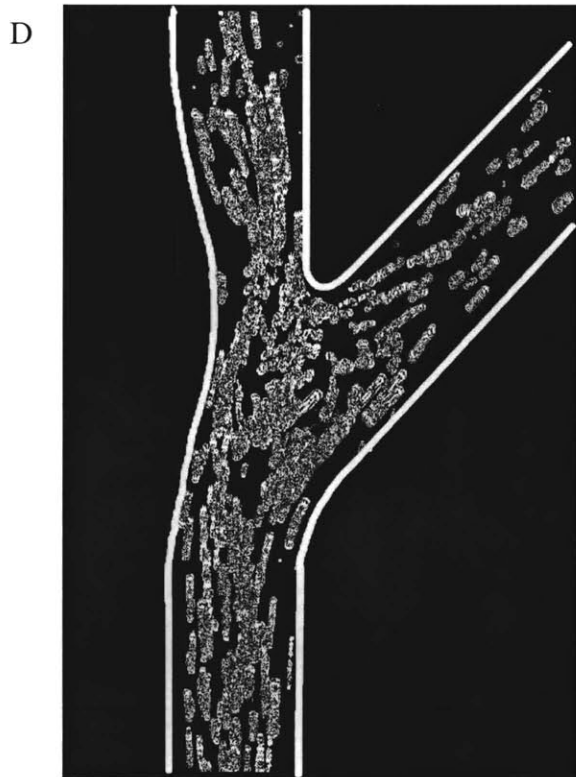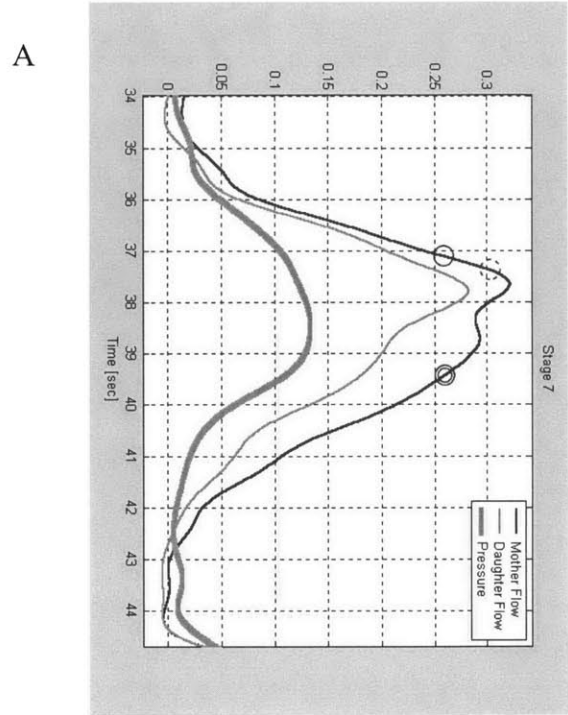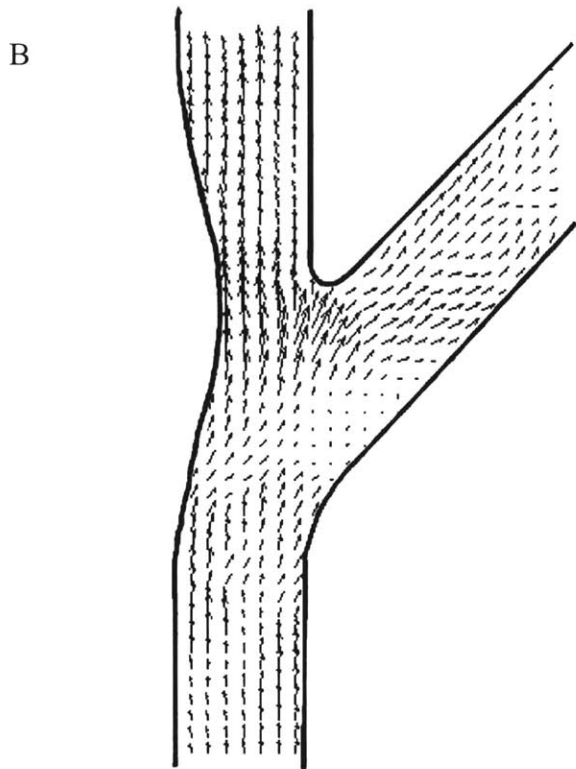
Figure 3-15: Case 16 visualization. <u>Mother vessel: Lesion</u>, Daughter flow: 90%, Collateral flow: 0. (A) Waveform: Dashed circle: PIV, Single circle: Streamlines at acceleration, Double circle: Streamlines at deceleration. (B) PIV. (C) Streamlines at acceleration. (D) Streamlines at deceleration.

Figure 3-16: Case 17 visualization. <u>Mother vessel: long lesion</u>, Daughter flow: 90%, Collateral flow: 0. (A) Waveform: Dashed circle: PIV, Single circle: Streamlines at acceleration, Double circle: Streamlines at deceleration. (B) PIV. (C) Streamlines at acceleration. (D) Streamlines at deceleration.

Cases 16 and 17 are two points along a spectrum that is somewhat different from the preceding cases in that instead of simulation of lesions in the daughter branch, the lesions were now located in 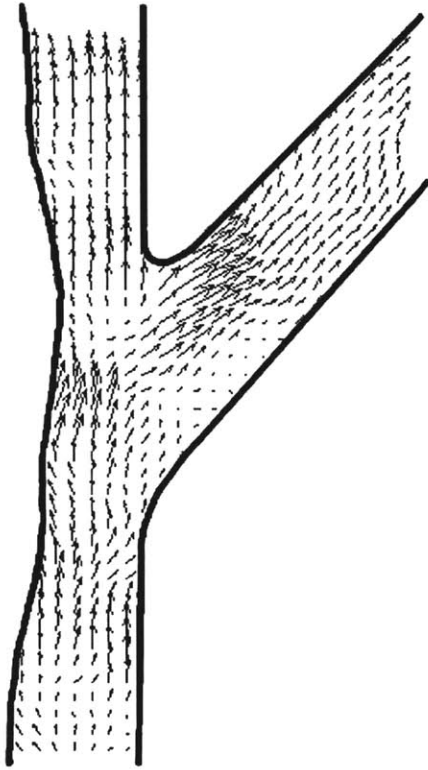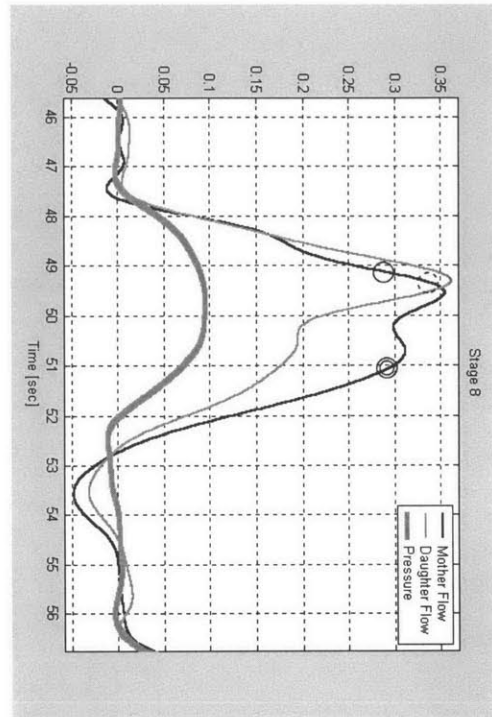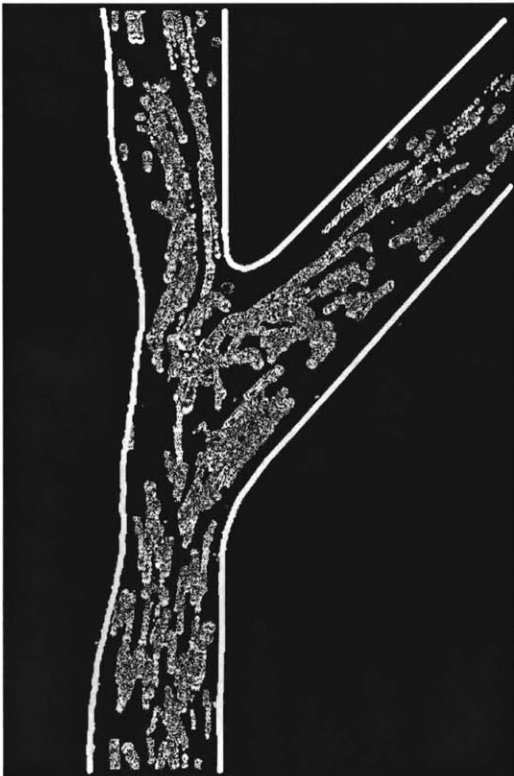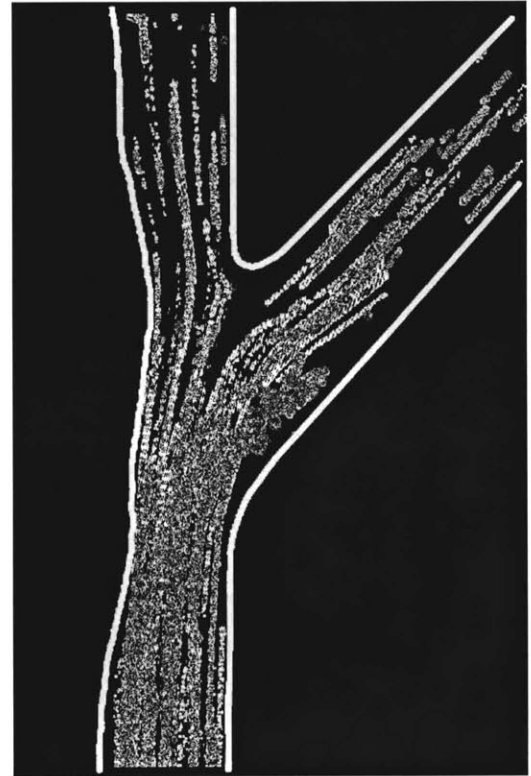the mother branch. The location of these lesions corresponds to the region of flow separation observed in the previous cases, and is thus an expression of the implicit assumption that flow separation is a trigger for atherosclerosis. The minimal luminal diameter was the same in both cases, however the lesion in case 17 was approximately twice as long as that of case 16, and began proximal to the ostium of the side branch (see figs. 3-15, 3-16). Waveform analysis for case 16 (fig. 3-15A) shows the same general properties observed in previous cases. It should be noted that downstream resistance on the daughter vessel was adjusted to produce the observed flow ratio, hence this ratio does not express the re-distribution of flow expected to arise from a lesion in the main branch alone. There is no apparent flow reversal in either the mother or the daughter vessel, nor is there a component of negative pressure at the end of deceleration. PIV (fig. 3-15B) as well as streamline analysis (fig. 3-15C,D) shows that despite the obvious region of flow separation in the side branch, there is no apparent separation in the main branch. Note particularly the long streamlines that pass very close to the lateral wall of the main branch all along the lesion in fig. 3-15C.

In contrast, waveform analysis for case 17 (fig. 3-16A) shows distinctly different features. First, the phase difference between the mother and daughter flow waveforms was reversed from all previous cases of the experiment, with the daughter waveform at a phase lead relative to the mother waveform. Secondly, there is now a clear aspect of flow reversal in both waveforms, as well as a component of negative pressure, suggestive of the existence of separation now in the mother branch. PIV (fig. 3-16B) as well as streamline (fig. 3-16C,D) images confirm this suggestion, with a clear region of flow separation seen in the mother branch distal to the apex of the lesion. Note that the flow accelerates along the lesion and does not separate up to the apex (fig. 3-16B), and then separates in the diverging section of the vessel distal to the apex. Note also that the region of separation in the daughter branch has decreased in size (compare figs. 3-15B,C to figs. 3-16B,C), presumably from the diversion of more flow into the daughter branch as the lesion in the mother branch progresses.

85

III.3.b. Part b – Temporal development of flow separation

Images of PIV performed during case 10 – straight mother vessel, no lesion in the daughter vessel and no collateral – are presented below. These two images show the flow vector field at two instances during deceleration.
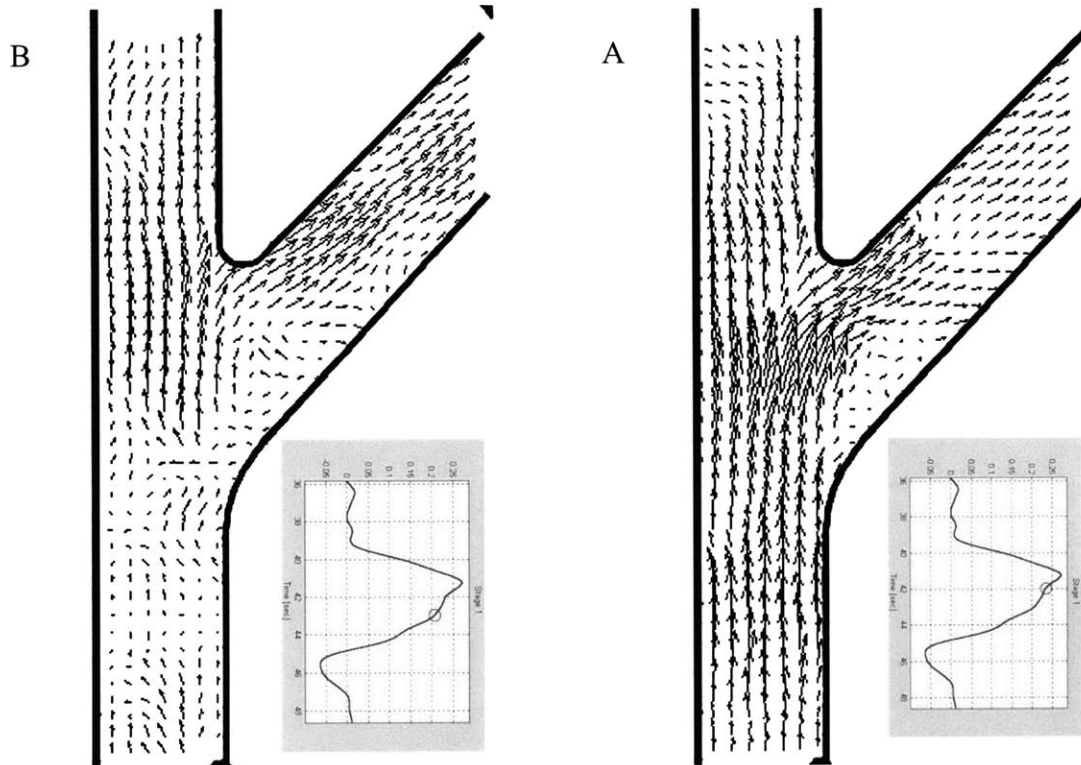
Figure 3-17: PIV at different time points. (A) PIV at beginning of deceleration. (B) PIV at mid deceleration. Circles denote instant of visualization

Both images in fig. 3-17 display the regions of flow separation in both the mother and the daughter branches. Comparison between fig. 3-17A and fig. 3-17B shows how these regions change over the course of a small part of the deceleration phase of flow. The region of separation in the daughter branch remains in the same location, and grows rapidly outwards in the radial direction to fill almost the entire ostium of the side branch. The region of separation in the mother vessel on the other hand, grows in a more axial direction, primarily proximally and the stagnation point rapidly moves upstream to the ostium of the daughter branch itself.

IV. Experiment 4 – Sedimentation analysis

IV.1 <u>Theory:</u>

The method outlined in the experiment 3 investigated the characteristics of the flow field from a perspective of the directions and velocities of flow of the fluid itself. As such it emphasized the mechanical stimulus imposed by the flowing blood on the cells in the vessel walls. However, blood is not simply a fluid, but rather plasma, with a particulate suspension of different cell types. The suspended cells come in contact and interact with the vessel wall, and these cell surface interactions govern many of the processes involved in the vascular response to injury, including thrombosis and inflammation. Thrombotic elements and inflammatory cells have no active method by which to propel themselves within fluid. Hence, the rate of passive deposition of particles onto the vessels walls is a crucial parameter in determining the extent and localization of the inflammatory process. Determining the rate and pattern of deposition of particles on the arterial wall is a formidable challenge, which cannot be solved analytically since it requires solutions to equations that are far too complex. Computational analysis is not well suited for this task either since the process contains an inherent stochastic aspect that is not well modeled numerically. Physical modeling requires a method by which to monitor and describe the deposition – something that is not readily done with most modeling schemes. Nonetheless, this chapter describes a method by which this process can begin to be elucidated.

The tracer particles used in the visualization part of the previous chapter eventually deposit onto the inner surfaces of the model walls as a result of physical aspects of both the vessel wall and flowing particles. The vessel walls of the model are somewhat sticky, and particles that collide with the wall can adhere to the wall and remain in place. The model adhesive process is analogous to the initial deposition of inflammatory cells onto vessel walls where the "stickiness" is provided by receptor-ligand interactions that form between the inflammatory cells and the endothelium or exposed basement membrane. The second factor that causes particles to accumulate on the model walls is that despite all attempts, the particles were never exactly neutrally buoyant. This meant that during the course of flowing through the models, the particles would migrate to either the top or the bottom of the model at different rates. Once

particles reached either the top or the bottom of the channel they began to roll forward along the model wall until they cleared the model, collided with another particle or reached a region of very low shear stress. The last two cases would cause the particles to become trapped in their location and to accumulate and aggregate in these sites, much like leukocyte adhesion and platelet aggregation.

Ultimately, clear patterns emerge in the density of particle deposition after the model has been perfused for several minutes. These patterns, for the reasons specified above, are interpreted to indicate the statistical variation in the probability of deposition of inflammatory cells and factors. The assumption made here is that a region of high particle concentration in the model denotes a region that will ultimately have a high load of inflammatory cells in vivo. It is important to note that once the inflammatory cells have extravasated through the arterial wall, they are subject to different chemotactic influences and their final location is no longer simply a function of passive sedimentation. Additionally, it must be realized that the absolute number of particles that accumulate at the end of the experiment has no significance in and of itself since it reflects not only the flow pattern but also the number of particles injected as well as the mismatch in buoyancy that happens to occur for that specific batch of particles. Only the relative distribution of particles carries any physical significance.

IV.2 Experiment:

IV.2.a. Part a – Experimental scenario

At the end of each flow visualization experiment defined in table 3-2, a still image was taken of the particles trapped inside the model. These images were enhanced, fit with an outline and the sedimentation pattern was analyzed.

IV.2.b. Part b – Effect of taper in mother branch

To analyze the effect of taper in the mother vessel on the sedimentation pattern, the model was perfused with the daughter branch completely open and no collateral flow. The following stages were performed one after the other without stopping the pump or draining the particles:

1. 3 minutes with a tapered mother vessel.
2. 3 minutes with a non-tapered mother vessel.
3. 3 minutes with a tapered mother vessel.

Particles were injected into the model at the beginning of each stage and an image was taken at the end of each stage for sedimentation analysis.

IV.3 Results and Discussion:

IV.3.a. Part a – Experimental scenario

The final image for each one of the cases in table 3-2 is presented below. Regions of higher and lower particle densities can clearly be made out, representing the relative probability of particle deposition. Some trends, such as the high rate of deposition in the ostium of the side branch, or the relative sparing of the region adjacent to the flow divider can be identified in all cases. On the other hand, features such as the deposition in the main branch can be seen to change from case to case.
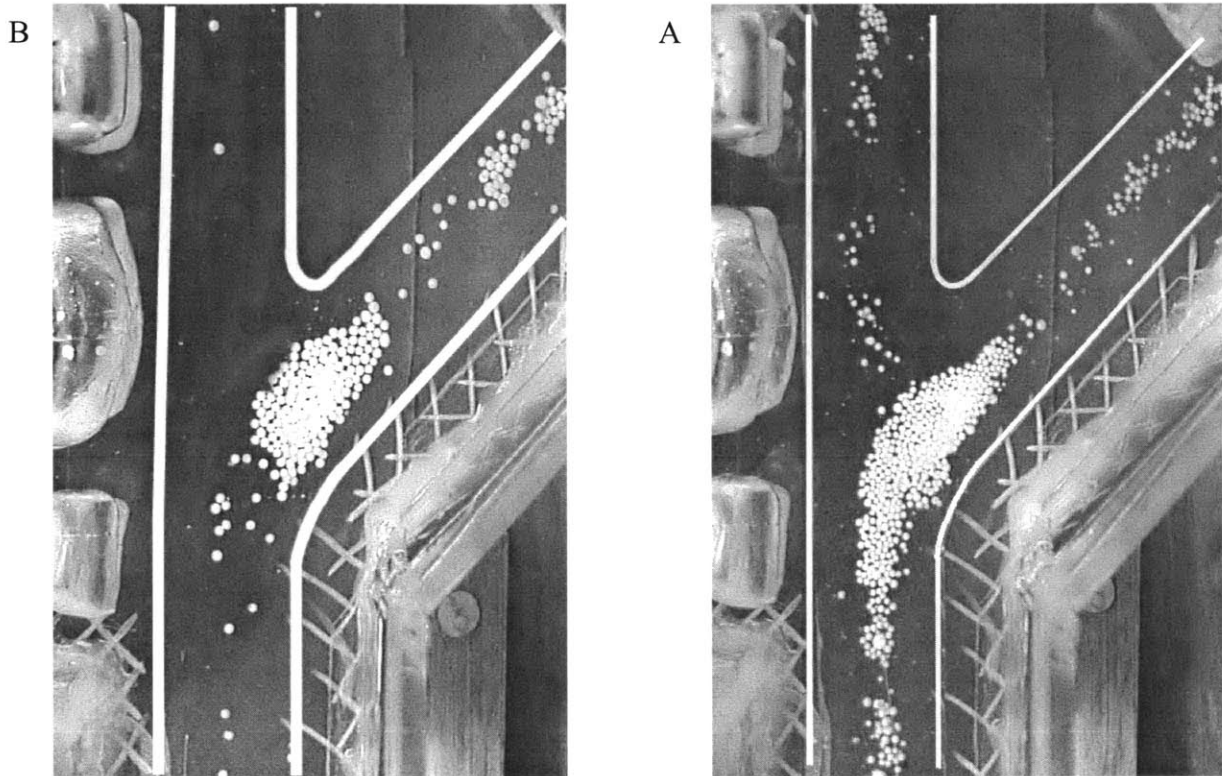
Figure 3-18: Case 10,11 sedimentation patterns. (A) Case 10 – Straight mother vessel, no lesion in side branch, no collateral. (B) Case 11 – <u>Tapering mother vessel</u>, no lesion in side branch, no collateral.

Figure 3-18 shows the sedimentation pattern for a straight and tapered mother vessel, the first two cases defined in table 3-2. Fig. 3-18A clearly shows a high relative rate of deposition associated with both regions of flow separation demonstrated in the previous experiment (see fig. 3-8). The region of separation in the daughter vessel has a particularly high rate of deposition, although the spillover of this region into the main branch is a result of particle collisions with particles that have already been deposited and is not likely to occur in vivo. Note the concentration of particles in the region that corresponds to the distal portion of flow separation in the main branch. Also note the complete sparing of the flow-divider region. In contrast, fig. 3-18B shows an entirely different pattern. Sedimentation in the flow separation region in the daughter branch is similar to before as well as deposition in the distal portion of the daughter branch. Also similar to fig. 3-18A is the sparing of the flow divider region. However, in contrast to fig. 3-18A there is near total sparing of the main branch starting from the point at which tapering of the mother vessel begins and all the way out to the edge of the image.
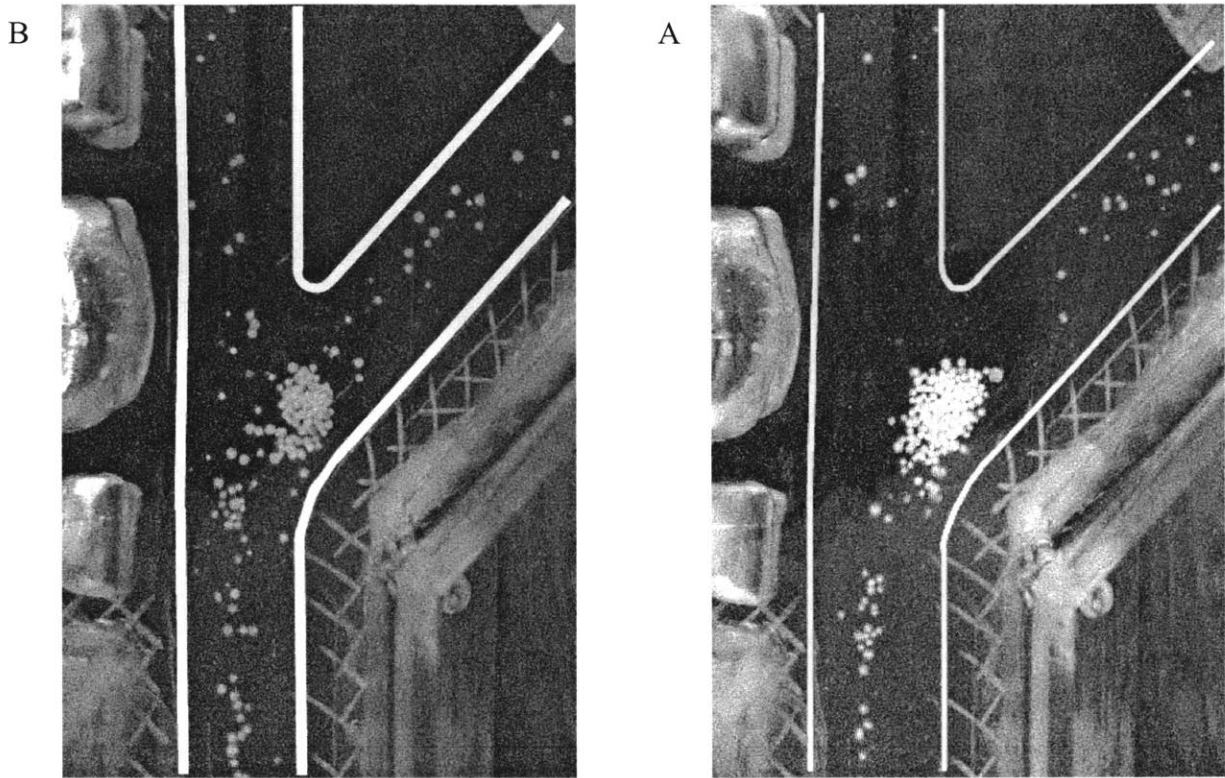
Figure 3-19: Case 12,13 sedimentation patterns. (A) Case 12 – Tapered mother vessel, Daughter flow: 61%, no collateral. (B) Case 13 – Slightly tapered mother vessel, Daughter flow: 17%, no collateral.

The sedimentation pattern for cases 12 and 13 that represent the gradual occlusion of the daughter vessel are presented in fig. 3-19. The particle deposition in the ostium of the daughter branch is still quite similar to the pattern seen in the previous images (see fig. 3-18). This is despite the fact that there is now considerably less flow into this branch of the bifurcation. Note in fig. 3-19A that the distal portion of the mother branch, beginning with the tapering segment is still relatively spared of particle deposition.

Case 13 however has very little flow into the daughter vessel and thus less taper is needed to prevent flow separation in the mother branch (see fig. 3-11). In effect, this case begins to approach a geometry comprised of just one flow channel. Accordingly, the particle deposition pattern in the main branch (fig. 3-19B) can be seen to approach a more homogeneous density along the length of the mother branch.
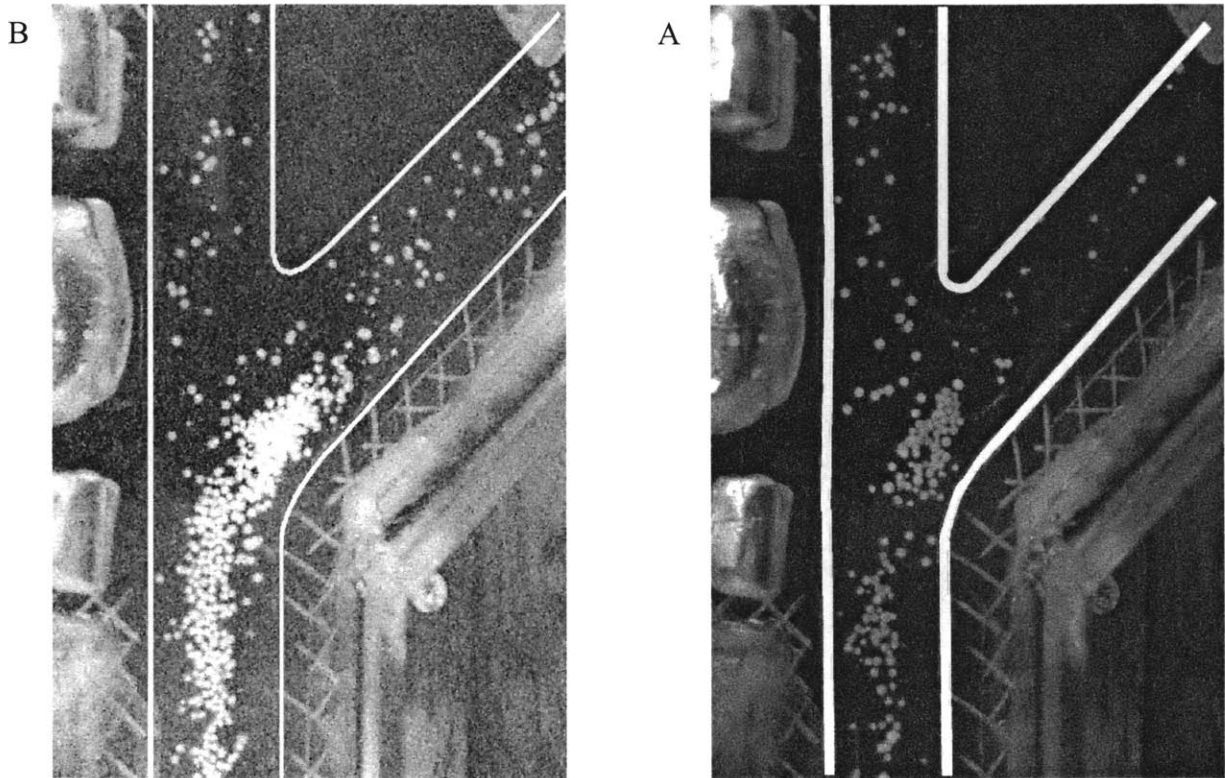
Figure 3-20: Case 14,15 sedimentation patterns. (A) Case 14 – Straight mother vessel, Daughter flow: 8%, Collateral flow: 25%. (B) Case 15 – Straight mother vessel, Daughter flow: 93%, Collateral flow: 36%.

The geometry of case 14 is in essence that of a single straight flow channel – the mother vessel. Flow into the daughter vessel in this case is nearly zero. Accordingly, the sedimentation pattern shows very little particle deposition in the daughter branch. There is still a slightly higher concentration of particles in the ostium of the side branch, most probably from flow disturbances at this point caused by the discontinuity in the wall, as well as the small flow-induced separation that can be identified in fig. 3-12C. Particle deposition in the mother branch is almost entirely uniform, reflecting the fact that flow in this branch is for the most part axial flow through a straight channel (see fig. 3-12B).

Case 15 represents the dilation of the daughter branch. As shown in the previous experiment (fig. 3-14), this re-creates a large region of separation in the mother branch, as well as the obvious region of flow separation in the ostium of the daughter branch. Examination of the sedimentation pattern reveals that both these regions of separation are now associated with high particle deposition rates superimposed on a homogeneous distribution in the entire bifurcation.
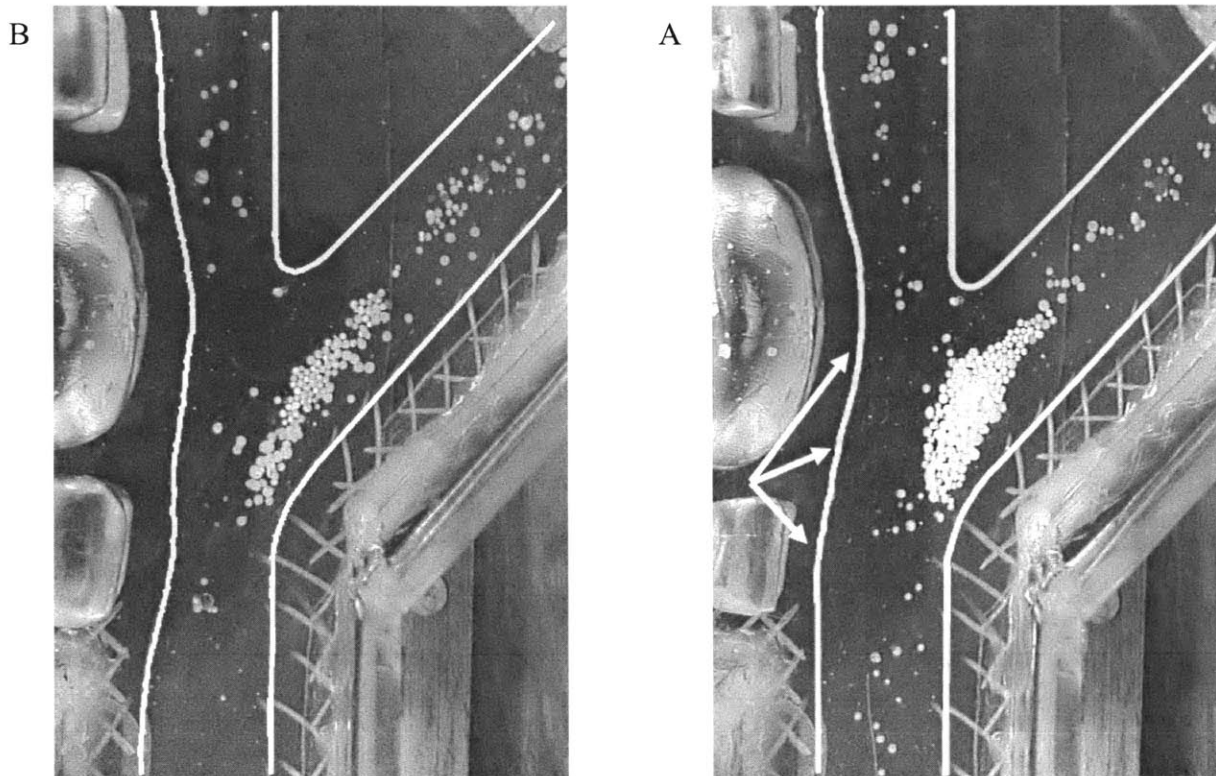
Figure 3-21: Case 16,17 sedimentation patterns. (A) Case 16 – Lesion in mother vessel, no lesion in side branch, no collateral. (B) Case 17 – Long lesion in mother vessel, no lesion in side branch, no collateral.

A distinct high density of deposition can be seen in the ostium of the daughter branch in case 16 (fig. 3-21A). This pattern of deposition correlates in size and shape to the region of separation that was shown to exist in this location in figure 3-15C. The mother vessel in fig. 3-21A exhibits a fairly uniform deposition pattern along its entire length. Note however the region of accelerating flow up to the apex of the lesion denoted by the arrows. This region is almost entirely spared of particle deposition, most likely caused by the accelerating flow causing a region of high shear stress in this part of the bifurcation, which tends to tear the particles away and prevent them from depositing. Figure 3-21B shows the same effects present in case 17. The deposition in the daughter branch has a flatter pattern, corresponding to the flatter shape of the flow separation seen in fig. 3-16C. The rate of deposition in the mother branch is clearly divided into two regions, a low deposition region proximal to the apex of the lesion, and a high deposition region distal to the apex in the same place that flow separation was previously observed (see fig. 3-16D).

IV.3.b. <u>Part b – Effect of taper in mother branch</u>

The sedimentation patterns at the end of each of the three successive stages described in the experiment are given below:
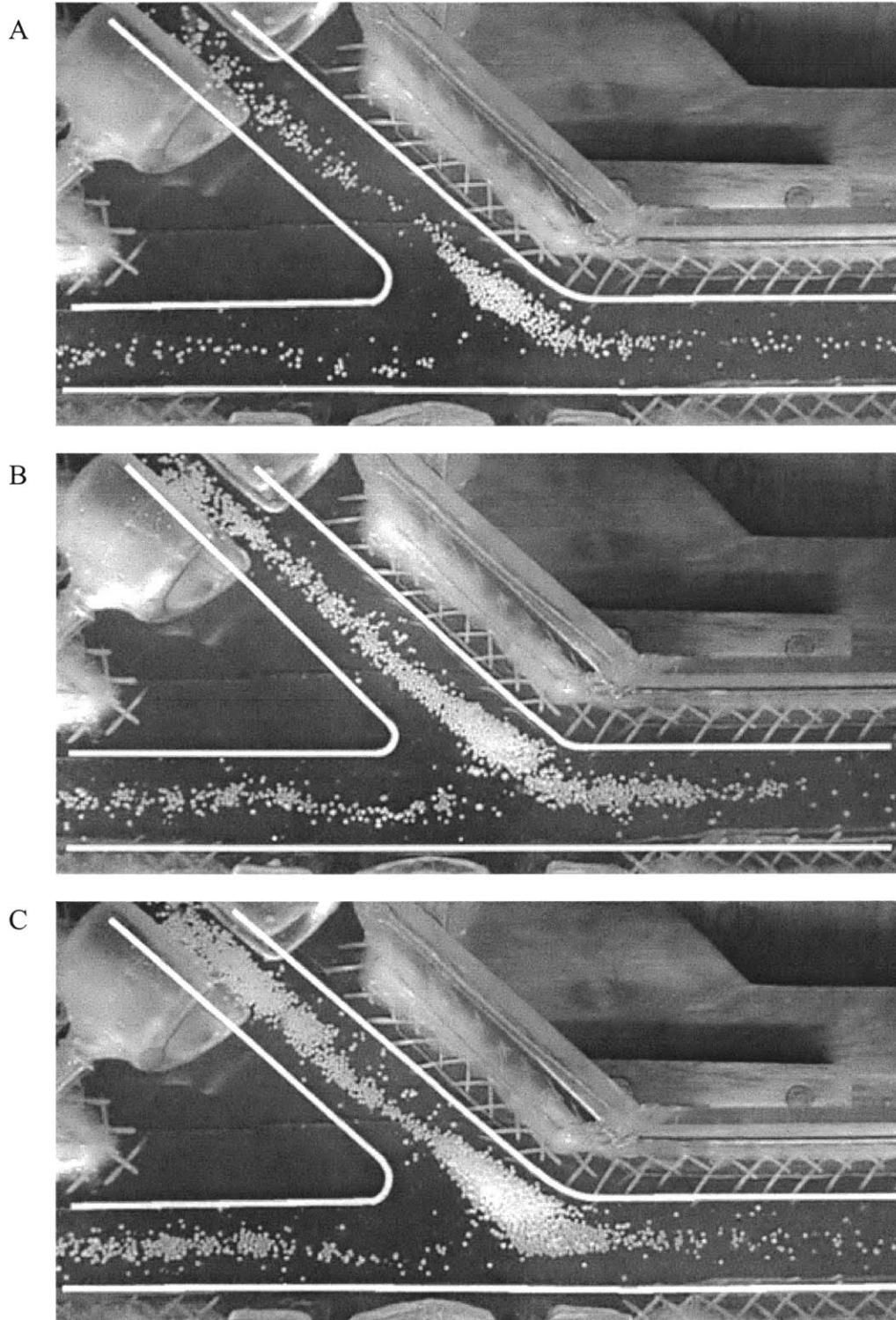

Figure 3-22: Taper effect on sedimentation. Patterns at the end of (A) 3 minutes with taper. (B) 3 additional minutes without taper. (C) 3 additional minutes with taper.

Analysis of fig. 3-22 shows the effect of a slight taper in the mother vessel on the pattern of particle deposition in this vessel from the point opposite the ostium of the daughter branch distally. After the first three minutes with taper (fig. 3-22A) a pattern emerges whereby deposition was heaviest in the region of separation in the daughter branch and in the distal part of the daughter branch itself. The distal portion of the mother branch has a relatively low rate of deposition in comparison to the daughter branch and a comparable rate to that of the proximal portion of the mother branch. The section of mother branch opposite the ostium is at this stage spared of almost any deposition. After an additional 3 minutes, now with no taper in the main branch, an entirely different pattern emerges (fig. 3-22B). The added deposition in the distal portion of the mother branch (particles were not cleared between these 3 stages), is now comparable in rate to the daughter branch. Furthermore, the region in the mother branch opposite the ostium now shows a clear deposition at a rate that is comparable with, if not higher than, the other segments in this vessel. Clearly, removal of the taper and thus creation of a region of flow separation in the mother branch (see figs. 3-8, 3-9) had an accelerating effect on the rate of particle deposition. Three more minutes with the taper re-introduced (fig. 3-22C) re-enforced this phenomenon. As can be seen, the rate of deposition in the distal portion of the mother vessel slowed considerably. Furthermore, the region opposite the ostium did not gain any particles. In fact, the opposite was true – despite the injection of an equal number of particles into the model during these three minutes, the number of particles in this region actually decreased.

V. References

1.   Friedman MH, Bargeron CB, Duncan DD, Hutchins GM, Mark FF. Effects of Arterial
        Compliance and Non-Newtonian Rheology on Correlations Between Intimal Thickness
        and Wall Shear. *Journal of Biomechanical Engineering*. 1992;114:317-320.
2.   Hart DP. Super-Resolution PIV by Recursive Local-Correlation. *Journal of Visualization*.
        1999;10.

Chapter 4: Conclusions

This chapter summarizes the results and discussions presented in chapter 3, as well as integrates the results obtained in the four experiments presented and highlights the way in which they fit together. General trends in the data are derived and the implications for clinical and experimental work are discussed in terms of inertance dominated flow, mathematical modeling, flow visualization and sedimentation analysis.

Many different approaches can be used to model the circulation, indeed most phenomena in the body. One could model the anatomy, physiology and/or pathology of the relevant tissues or organs. The approach taken here is different in that the focus was mechanistic. Only rigorous control of the model configuration with and eye towards specific parametric regulation could enable us to obtain this mechanistic insight. Models that are more faithful to the anatomy, physiology or the pathology cannot provide this perspective and in our view never really approach actual physical modeling. One can understand the systems involved and the mechanisms that affect them by transcending the specific scenarios at hand, and without the limits of attempting to produce an accurate description of a biological system.

I. Inertance dominated flow

That flow in the isolated region of the vascular bed at the level of a bifurcation was shown to be inertance dominated, had profound implications for physical and mathematical modeling of bifurcated vascular beds. Physical models can be constructed with less precise consideration of potentially complex stress-strain relationships, greatly simplifying the task of building a meaningful model. Similarly, if arterial compliance can be disregarded mathematical models can be greatly simplified. The number of free parameters is reduced. This allows for a more meaningful fit for the two free parameters that remain, resistance and inertance, and makes it possible to apply the fit obtained for these parameters to a description of the properties of flow, in particular the changes in resistance from flow separation. It is important to note that this does not mean that the compliance of the arterial wall plays no role in flow within a bifurcation. Indeed, certain phenomenon, such as the temporal distribution of flow between the two branches and the

damping of the waveforms to name just two, would not exist were it not for the existence of compliance. However, to a first order approximation, the mere fact that the model is compliant and that this compliance is within the general range of the prototype system, as observed by the approximate distension of the flow channels with each cycle, is enough to ensure that these important effects will exist in the model in the same qualitative way that they do in-vivo.

II. Mathematical modeling

It is possible to provide a relatively simple lumped parameter mathematical model that describes the flow system very well, as was demonstrated by the excellent fit of the predicted to the measured waveforms in fig. 3-5. This model can then be applied to obtain quantitative information regarding the properties of flow within the model system. Specifically, this can be used as in fig. 3-6 to quantify the resistance of the vessels. The value of the resistance carries physical significance in and of itself as it determines the workload for perfusing a tissue segment through the relevant arteries. Additionally, changes in the resistance can be used to infer changes in the flow patterns within the arteries, specifically the extent of flow separation as was discussed in the theory section (Ch. 3 II-1). Fig. 3-6 demonstrates the ability to quantify changes in the resistance of a vessel due entirely to shifts in the flow patterns (cases 2-4, cases 7-8), without any change in the physical properties or the geometry of the vessel itself. Since these changes are brought about by alterations of a neighboring vessel, this allows one to quantify the interactions that exist between one site in the arterial tree and another. The interactions observed and their effect on the resistance fit with the theoretical predictions made previously regarding the effects of geometric alterations in one vessel on another.

The ability to quantify resistive effects in this way and to accurately deduce the local variations in the patterns of flow is however limited by the manner in which differential pressure measurement is performed. Using an external differential pressure sensor results in an a priori limit on the signal-to-noise ratio and hence the accuracy and reliability with which these measurements and deductions can be made. To produce more accurate results, pressure wires were used instead of the differential pressure sensor, offering the advantage of potential insertion into the silicone segment of interest itself. By

locating one pressure wire immediately proximal to the region of flow separation, and a second pressure wire immediately distal to the region of flow separation, a measurement that does not include the effects of the interface pieces proximal and distal to the bifurcation can be made. However, the sensitivity of the pressure wires is much lower than that which can be achieved by the differential pressure sensor. This is a direct consequence of the fact that the pressure wire is a clinical tool designed to measure pressures in the range of 80-120 mmHg. As discussed previously, the pressure drops that can be expected due to subtle differences in flow separation are on the order of 0.1-0.01mmHg and are thus not picked up by the pressure wires. It should be noted however that if the same calculation is performed for the in-vivo situation, the expected pressure drop from flow separation increases to approximately 1mmHg. It is therefore likely that this same effect could be measured in the clinical setting, or if smaller models were built to investigate this technique specifically.

III. Flow visualization

In general, the methods used here have proven to be useful in describing the expected flow phenomena within the experimental geometries. PIV and streamline analysis, in combination with the waveform analysis were complementary and capable of demonstrating subtle flow effects. In general, all cases of the experimental model demonstrated and localized regions of flow separation, regions of low and high shear, accelerations and decelerations as predicted from basic principles. The location and extent of these flow phenomena had a cyclical temporal course that was dependent upon different parts of the model geometry over the course of an entire cycle. The detailed changes in flow patterns from one case of the experiment to the other, representing either the course of progression of atherosclerotic disease, compensation by the arterial system or the effect of mechanical intervention were dealt with in the previous chapter. We shall review here the general trends of major importance:

Taper in the mother vessel had a significant effect on the flow pattern. In geometries where separation in the mother vessel occurred, namely those with significant daughter branch flow, a very gradual taper in the mother vessel removed the region of flow separation almost entirely. This is not a surprise when one considers the fact that

native arterial geometry almost always tapers at the site of significant bifurcations; the bifurcation of the left main coronary artery into the left anterior and circumflex arteries is an excellent example of this phenomena. Yet the impact of tapering on flow separation carries significant implications when considering the optimal course of intervention in clinical scenarios that include dilation of a lesion at this location.

The pattern of flow in the mother vessel was directly affected by alterations in the daughter vessel alone. Gradual occlusion of the daughter vessel reduced the region of flow separation opposite the ostium of the daughter branch. At high levels of daughter branch occlusion, non-separated flow was achieved in the mother branch even without the introduction of taper. Since the removal of taper, in the absence of flow separation, physically increases the vessel diameter lowering resistance to flow, it seems reasonable that the adaptive arterial bed would develop in this direction, i.e. compensatory dilation of the distal portion of the mother vessel in response to occlusion of the daughter vessel. This potential observation remains to be shown in vivo. Dilation of the daughter branch on the other hand, re-established a significant region of separation in the mother branch. In some instances, for example where significant collateral flow was present, this new region of separation can be substantially more prominent than the one that existed in the same location before occlusion of the side branch. Further analysis is required to identify other adaptive changes, e.g. alterations in downstream resistance to flow, which could affect the extent of the new region of separation in the mother vessel. This sort of analysis could have important clinical implications when considering the optimal approach to dilation of lesions in a side branch.

The flow in a geometry that includes a lesion in the main branch had important characteristics that were related to the geometry of the lesion present. The length of the lesion in the mother branch affected the flow separation in the daughter branch. A long lesion reduced the area of flow separation in the ostium of the daughter branch and in this sense was "protective" of side branch. Since occlusion of flow in the side branch reduced the extent of separation in the main branch, as was discussed previously, this protective aspect of a bifurcation can be seen to work bilaterally, at least in the case examined of a branch cross-sectional ratio of 1:1. Short lesions in the mother branch which had the same geometry of the space taken up previously by the side branch induced flow

100

separation, induced little-to-no further flow disturbances. On the other hand, a long lesion was associated with a region of flow separation that begins at the apex of the lesion and extends distally. This is consistent with the clinical observation that these lesions grow in the distal direction.

IV. Sedimentation analysis

A gap exists between the well-documented pattern of flow within the bifurcated geometry, namely that of regions of flow separation and high and low shear stress, on the one hand and the biological mechanism of vascular disease on the other. Sedimentation analysis of the sort performed here goes a long way towards bridging this gap by providing empirical evidence for the pattern of deposition of blood-borne particles and inflammatory cells as a result of the observed flow patterns. Several documented patterns in particular were easily observed including:

- Sparing of deposition of the angles of the flow divider, correlating with the high shear stress evidenced by flow visualization.

- Highest rate of deposition in the ostium of the daughter vessel, correlating with the resident region of flow separation and consistent with the most common localization of atherosclerotic lesions.

- Elevated rate of deposition in the main branch opposite the ostium of the side branch in those cases where flow separation in the main branch was shown to occur.

Lesions in the mother vessel affected deposition of particles in their vicinity, i.e. a relative sparing of deposition in the proximal portion leading up to the apex of the lesion and an increase in deposition from the apex distally. The length of a lesion in the mother branch was also shown to have an effect on the pattern and extent of deposition of particles in the side branch facing this lesion.

Of particular interest is the effect that taper in the main branch has on the rate of particle deposition in the distal portion of this vessel, downstream from the bifurcation. Very gradual tapers were protective of the distal portion of the vessel, in some cases (see fig. 3-18B) almost to the point of preventing deposition altogether. Conversely, non-tapering vessels, despite having a larger physical cross section showed a clear pattern of

sedimentation in the regions where previous visualization showed separation to exist, as well as an elevated overall sedimentation rate in the distal portion. In the region of the lateral wall opposite the ostium of the side branch, a tapering mother vessel not only effectively eliminated sedimentation of additional particles, but also removed particles that had previously accumulated there. These observations carry potentially important clinical applications relating to the way that lesions in the mother vessel are dilated and the geometrical end result one attempts to achieve.

V. Future work

The methods described in this thesis, when taken collectively, make up a useful set of tools for the analysis of the interactions between different sites in the arterial tree. For this analysis to have a significant impact on clinical practice, a general set of guidelines needs to be produced for the most common problems encountered in the clinical setting. One way of creating such guidelines would be to simulate possible clinical interventions in the scenarios discussed herein, such as the dilation of a side branch or the creation of a main branch with or without taper, using models constructed to test specific parameters in geometry. These parameters might include, the ratio of diameters of the two branches, the angle of bifurcation, the total flow into the segment, etc.

There are ongoing debates within the clinical community as to the optimal course of treatment given a specific patient presentation, for example, the choice of bypass surgery, angioplasty or stenting of one branch of a bifurcation lesion, the other or both. Often times, the only indications available with which to judge the efficacy of one course of treatment or the other are probabilistic predictions from large clinical trials and the acute and long-term angiographic images of the vessels. Clinical trial data are however non-mechanistic and offer little insight into the individual patient. Angiography is severely limited in its ability to describe the one physical parameter of physiologic relevance to the patient – flow. The techniques described here are highly versatile and allow for the creation of widely varying geometries, as well as the simulation and comparison of a whole host of clinical interventions. We believe that by analyzing the flow patterns created by these different interventions, one could provide the mechanistic

evidence needed to better tailor a clinical approach to the specific patient presentation, as well as evolve the existing approaches to produce higher efficacy of the result.

The analysis presented here of particle deposition is a novel approach in the description of flow patterns within arteries. By bridging the gap between streamlines and adhesion, this technique provides direct evidence of a crucial step in the process of atherosclerotic lesion formation. This analysis should be taken further to include different properties of walls as well as particles and different scenarios of flow. One case was demonstrated in this thesis in which alteration of the geometry (introduction of taper after a period of non-taper) seemed to actually reverse pre-existing adverse effects. This is an important concept for the practice of clinical treatment of atherosclerosis as it hints at the possibility of allowing for regression of pre-existing lesions. It is understood that additional study beyond particle deposition rates will be required. In particular examination of the interaction of mechanical stimuli with cells present within the arterial wall is critical to determining if arrest of re-stenosis or even actual plaque reduction can be achieved.

Finally, the models built here allow for complete dynamic control of the model geometries and the conditions of flow. Models are however ultimately only capable of simulating the flow field and not the biological ramifications of flow. It may be possible to begin to understand how the latter affects the former by creating hybrid model systems with living elements. Models can be seeded with vascular cells and cell-replete plasma perfused through the system. The impact of flow alterations on endothelial cell ultrastructure, myofilament alignment, smooth muscle cell proliferation and inflammatory cell infiltration might then be examined.

# Appendix A: Design and operation of sensors

Differential pressure sensor:

1. Parts:
   1.1. Motorola MPX10DP – Differential pressure sensor.
   1.2. 324 Quad Op-Amp chip.
   1.3. Analog devices AD624BD – Instrumentation amplifier.
2. See circuit diagram on next page.
3. Gain settings:

| Gain	100						200						500						1000					
Dipswitch	1	2	3	4	5	6	1	2	3	4	5	6	1	2	3	4	5	6	1	2	3	4	5	6
On		x				x			x			x				x		x		x		x	x	x
Off	x		x	x	x		x	x		x	x		x	x	x		x		x		x			

4. Zero adjustment:
   4.1. Coarse: using 1K potentiometer on –15V source.
   4.2. Fine: using 10K potentiometer on 624.
5. External terminals:
   5.1. Blue: Ground
   5.2. Green: +15
   5.3. Yellow: -15
   5.4. Red: +5
   5.5. Orange: V_{out}
   5.6. Brown: Output common (can be grounded).

Amplification circuit for differential pressure sensor:
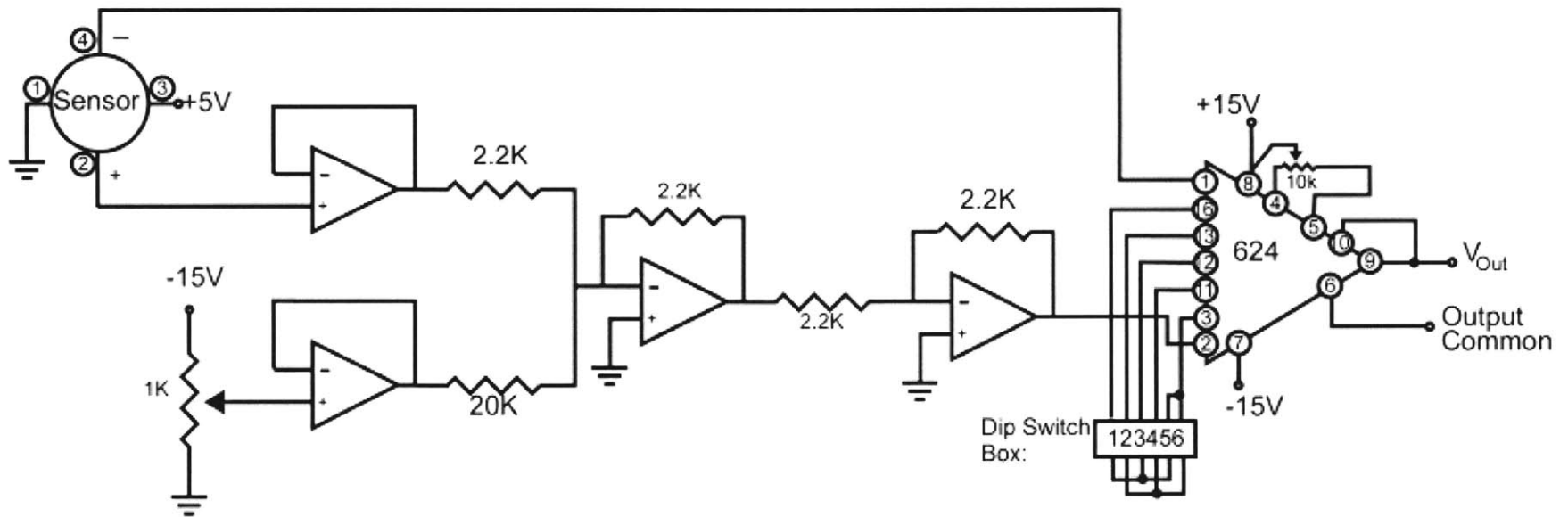
Amplification circuit for pressure wire:
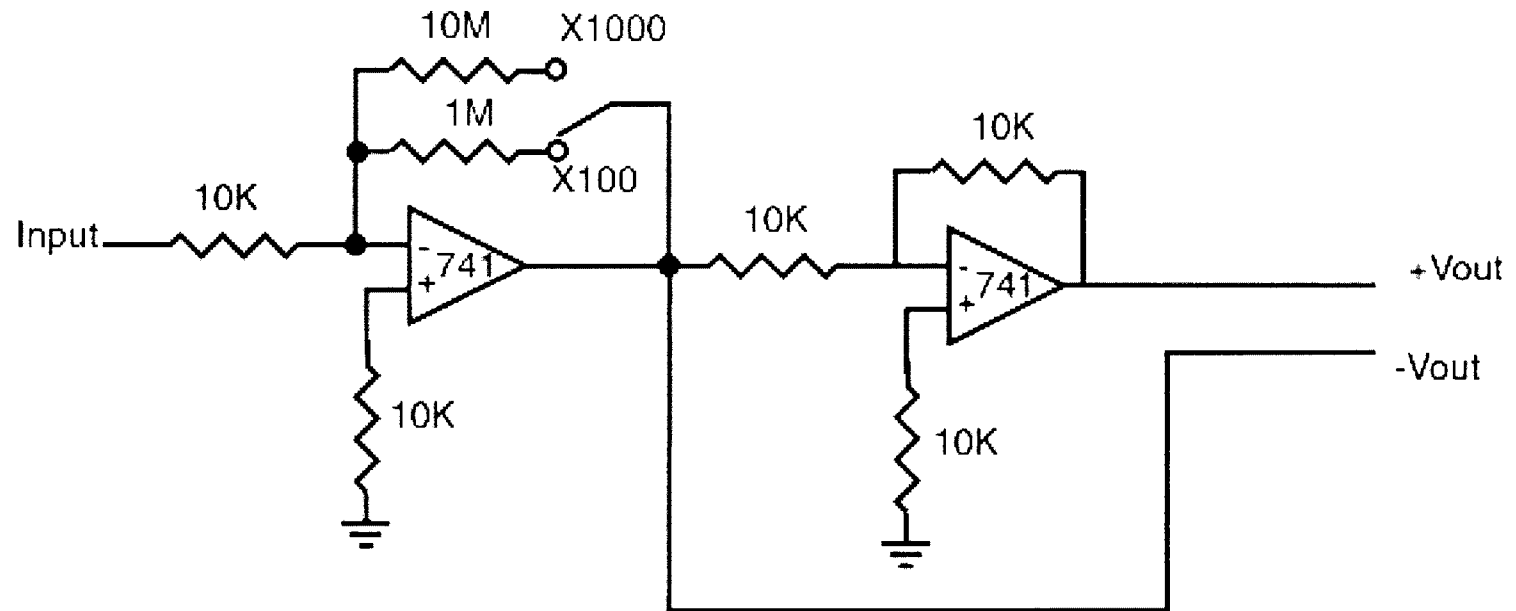
Appendix B: Code

All data analysis was performed using MATLAB V.5.3 by Math Works. The code for the few non-trivial operations is given below:

Filtering of waveforms

Use:

This was performed for low-pass filtering of pressure or flow waveforms. The filter order used throughout this thesis was 512, the cutoff frequency was for the most part 1Hz or 2Hz. which allows at least the first 10 or 20 harmonics of the fundamental frequency of the pump to pass unfiltered.

Code:

```
myfilter = fir1(filter_order,cutoff_frequency*2/sampling_frequency);
filtered_signal = filtfilt(myfilter,1,unfiltered_signal);
```

Difference function for inertance and resistance

Use:

This function takes as inputs a value for the inertance and resistance as well as the flow and differential pressure waveforms. The function calculates the predicted differential pressure waveform based on the theoretical model and the measured flow waveform. The output is the integral of the absolute value of the difference between the predicted and measured differential pressure waveforms.

Code:

```
function z=difference(LR,dpressure,flow)
L=LR(1);
R=LR(2);
Factor=1;
derived_wave=filter([R+L -L],(1/Factor),flow);
temp=derived_wave(80:length(derived_wave));
temp(length(temp)+1:length(derived_wave))=derived_wave(length(temp)+1:l
ength(derived_wave));
derived_wave=temp;
difference_wave=abs(derived_wave-dpressure);
```

```
z=sum(difference_wave);
```

Difference function for resistance

Use:

This function is similar to the one above. It differs only in that it assumes a known value for the inertance.

Code:

```
function z=difference_R(R,L,dpressure,flow)
Factor=1;
derived_wave=filter([R+L -L],(1/Factor),flow);
temp=derived_wave(80:length(derived_wave));
temp(length(temp)+1:length(derived_wave))=derived_wave(length(temp)+1:l
ength(derived_wave));
derived_wave=temp;
difference_wave=abs(derived_wave-dpressure);
z=sum(difference_wave);
```

Optimization function for resistance

Use:

The function uses the Nelder-Mead simplex algorithm to find the optimal value of the resistance. Optimum is determined as that which minimizes the above given difference function for resistance based on an arbitrary inertance value.

Code:

```
R=fmins('difference_R',R0,foptions,[],L0,pressure_wave,flow wave)
```

Prediction function

Use:

This function uses the resistance generated by the optimization function, the inertance value and the measured flow waveform to generate a predicted pressure waveform according to the theoretical model.

Code:

```
predicted_dP=filter([R+L0 -L0],1,flow_waveform);
```